



รายงานวิจัยฉบับสมบูรณ์

# โครงการ การศึกษาสมบัติแบบแข็งเนื่องจากการเจือแบบตัวรับบนตำแหน่ง A ใน $0.93Bi_{0.5}Na_{0.5}TiO_3$-$0.07BaTiO_3$ เพียโซอิเล็กทริกเซรามิกไร้ตะกั่ว

โดย ผู้ช่วยศาสตราจารย์ ดร.ศศิพร ประเสริฐปาลิฉัตร
ภาควิชาฟิสิกส์ คณะวิทยาศาสตร์
มหาวิทยาลัยนเรศวร

พฤษภาคม 2563

สัญญาเลขที่ TRG6080018

รายงานวิจัยฉบับสมบูรณ์

# โครงการ การศึกษาสมบัติแบบแข็งเนื่องจากการเจือแบบตัวรับบนตำแหน่ง A ใน $0.93Bi_{0.5}Na_{0.5}TiO_3$-$0.07BaTiO_3$ เพียโซอิเล็กทริกเซรามิกไร้ตะกั่ว

ผู้ช่วยศาสตราจารย์ ดร.ศศิพร ประเสริฐปาลิฉัตร
ภาควิชาฟิสิกส์ คณะวิทยาศาสตร์
มหาวิทยาลัยนเรศวร

สนับสนุนโดยสำนักงานกองทุนสนับสนุนการวิจัยและ
สถาบันวิจัยแสงซินโครตรอน (องค์การมหาชน)

# กิตติกรรมประกาศ

This work is financially supported by the Thailand Research Fund and Synchrotron Light Research Institute. Besides, I'm utterly grateful for contributions from several people and organizations which allowed this work to be completed. Their supports are greatly appreciated.

I would like to thank Dr. Jaru Jutimoosik and Dr. Pinit Kidkhunthod for their assistant and useful discussions on the synchrotron-based techniques. Asst. Prof. Dr. Theeranun Siritanon for the help on the Rietveld refinement technique. Assoc. Prof. Dr. Theerachai Bongkarn for the value discussions and for the dielectric measurement setup provided. Assoc. Prof. Dr. Tawat Suriwong for the advice on the Rietveld refinement. The synchrotron light research institute (public organization), Thailand, is also acknowledged for the synchrotron facilities and I would also like to thank Naresuan university for lab space and facilities.

**Abstract**

---

**Project Code :** TRG6080018

**Project Title :** Study of hardening characteristics by A-site acceptor doping in $0.93Bi_{0.5}Na_{0.5}TiO_3$-$0.07BaTiO_3$ lead free piezoelectric ceramics

**Investigator :** Assist. Prof. Dr. Sasiporn Prasertpalichat
Department of Physics, Faculty of Science, Naresuan University

**E-mail Address :** sasipornp@nu.ac.th

**Project Period :** 2 years

The inconsistent and unclear effects of doping in $Bi_{0.5}Na_{0.5}TiO_3$ (BNT-BT) lead-free ceramics as compared to that of PZT is one of the reasons that have limited their usage in practical applications. In this study, the effects of A-site Li and B-site Fe acceptor doping [$(Bi_{0.465}Na_{0.465}Ba_{0.07})_{1-x}Li_xTiO_3$ and $(Bi_{0.465}Na_{0.465}Ba_{0.07})Fe_xTi_{1-x}O_3$ , $x$ = 0.01–0.03] on the structural, microstructure, dielectric, electrical conductivity, ferroelectric and piezoelectric properties of lead-free 0.93BNT-0.07BT ceramics were systematically investigated. The phase ratio (*R3c*/*P4bm* ~ 80/20) was found to remain almost unchanged across the entire Li and Fe doping level studied. Moreover, both Li- and Fe-doped samples also exhibited similar trend of changes upon increasing doping level: an increase in average grain size, along with a decrease in resistivity ($\rho$) and activation energy ($E_a$), which are typical characteristics observed for acceptor doping. However, while a clear transition from slim to square-like *P-E* hysteresis loops ($E_c$ = 30.7 kV/cm, $P_r$ = 33.9 $\mu C/cm^2$) was observed in A-site Li doping from $x$ = 0.02 on, such changes were moderate in all B-site doped samples (i.e. a slight constricted *P-E* loops with $E_c$ ~ 13.5-15.1 kV/cm and $P_r$ ~ 28.6–31.7 $\mu C/cm^2$). The discrepancies could be linked to the differences in degree of stabilized ferroelectric order. This study suggests A-site doping as a more effective way for high power applications where high $E_c$ and temperature stability is required.

**Keywords :** Lead-free BNT-BT, hardening characteristics, A- and B-site acceptor doping, piezoelectric

# บทคัดย่อ

**รหัสโครงการ :** TRG6080018

**ชื่อโครงการ :** การศึกษาสมบัติแบบแข็งเนื่องจากการเจือแบบตัวรับบนตำแหน่ง A ใน $0.93Bi_{0.5}Na_{0.5}TiO_3$-$0.07BaTiO_3$ เพียโซอิเล็กทริกเซรามิกไร้ตะกั่ว

**ชื่อนักวิจัย :** Assist. Prof. Dr. Sasiporn Prasertpalichat
Department of Physics, Faculty of Science, Naresuan University

**E-mail Address :** sasipornp@nu.ac.th

**ระยะเวลาโครงการ :** 2 years

งานวิจัยนี้ศึกษาอิทธิพลการเจือแบบตัวรับบนตำแหน่ง A ด้วยลิเทียม (Li) และตำแหน่ง B ด้วยเหล็ก (Fe) ตามสูตรเคมี $(Bi_{0.465}Na_{0.465}Ba_{0.07})_{1-x}Li_xTiO_3$ และ $(Bi_{0.465}Na_{0.465}Ba_{0.07})Fe_xTi_{1-x}O_3$ (ที่ปริมาณ $x$ = 0.01–0.03)ตามลำดับ ที่มีต่อโครงสร้างเฟส โครงสร้างจุลภาค สมบัติการนำไฟฟ้า สมบัติไดอิเล็กทริก สมบัติเฟร์โรอิเล็กทริก และสมบัติเพียโซอิเล็กทริกในเซรามิก ผลการศึกษาพบว่าเซรามิกแสดงโครงสร้างผสมระหว่างเฟสรอมโบฮีดรัล (*R3c*) และเททระโกนัล (*P4bm*) โดยมีสัดส่วนเฟส *R3c/P4bm* ~ 80/20 ซึ่งไม่เปลี่ยนแปลงมากนักเมื่อปริมาณการเจือ ($x$) Li และ Fe เพิ่มขึ้น ในทำนองเดียวกันพบว่าเซรามิกที่เจือด้วย Li และ Fe มีการเปลี่ยนแปลงโครงสร้างจุลภาคและสมบัติการนำไฟฟ้าไปในทิศทางเดียวกันและด้วยปริมาณที่ใกล้เคียงกัน กล่าวคือ มีขนาดเกรนเฉลี่ยเพิ่มขึ้น ค่าสภาพต้านทานไฟฟ้า ($\rho$) และพลังงานก่อเกิดการนำไฟฟ้า ($E_a$) ลดลง ซึ่งล้วนเป็นลักษณะเฉพาะที่พบได้ทั่วไปจากการเจือแบบตัวรับ แต่อย่างไรก็ตาม พบว่าการเจือที่ตำแหน่ง A ด้วย Li ส่งผลให้วงวนฮิสเทอรีซิส (*P-E*) เปลี่ยนจากแบบบางเป็นแบบสี่เหลี่ยมอย่างชัดเจนที่ปริมาณ $x$ = 0.02 โดยมีค่า $E_c$ และค่า $P_r$ ค่อนข้างสูง ($E_c$ = 30.7 kV/cm, $P_r$ = 33.9 $\mu C/cm^2$) ในขณะที่การเจือที่ตำแหน่ง B ด้วย Fe ให้ผลเพียงปานกลางในทุกปริมาณการเจือ $x$ (วงวนฮิสเทอรีซิสแบบมีรอยหยัก, $E_c$ ~ 13.5-15.1 kV/cm และ $P_r$ ~ 28.6–31.7 $\mu C/cm^2$) งานวิจัยนี้แสดงให้เห็นว่าการเจือที่ตำแหน่ง A มีประสิทธิภาพที่ดีกว่าสำหรับการนำไปประยุกต์ใช้ในอุปกรณ์อิเล็กทรอนิกส์กำลังสูงซึ่งต้องการค่า $E_c$ และความเสถียรต่ออุณหภูมิค่อนข้างมาก

**คำสำคัญ :** เซรามิกไร้ตะกั่ว BNT-BT; สมบัติแบบแข็ง; การเจือแบบตัวรับที่ตำแหน่ง A และตำแหน่ง B; เพียโซอิเล็กทริก

## 1. Introduction

Lead zirconate titanate, $Pb(Zr_xTi_{1-x})O_3$ (PZT), and its derivatives have dominated the piezoelectric market for more than half a century due to their excellent electromechanical properties at the "morphotropic phase boundary" (MPB) [1] [2] and high curie temperature ($T_c$ > 300$^{\circ}$C), which enables a broader operating temperature [3]. Moreover, tailoring PZT's properties for specific applications are well established and can be directly done by chemical modification through dopant. For examples, 'hardening' characteristics, which is required for high-power applications such as transformer and ultrasonic motor, can be achieved in PZT simply by acceptor doping on either A- or B-sublattice site of the perovskite structure (e.g. $Fe^{3+}$/$Mn^{3+}$replacing $Ti^{4+}$/$Zr^{4+}$ or $K^+$ replacing $Pb^{2+}$). This causes a formation of negatively-charged defects (e.g. $Fe'_{Ti}$) along with compensating oxygen vacancies ($V_O^{\cdot\cdot}$). And it is widely accepted that these mobile charged defects either in the form of single ion (e.g. $V_O^{\cdot\cdot}$) or defect dipoles (e.g. $Fe'_{Ti}-V_O^{\cdot\cdot}$) could stabilize domain configurations and lead to a reduction of polarization contributions to the electrical response. Accordingly, the materials exhibit 'hard-type' characteristics which include a lowered electrical resistivity (i.e. higher conductivity), a decrease in the piezoelectric coefficient, dielectric permittivity ($\varepsilon_r$) and dielectric loss (tan $\delta$), along with an increase in $Q_m$ and coercive field ($E_c$) as well as more pronounced aging effects [4] [5] [6]. However, lead oxide (PbO), which is the main component in PZT ($\sim$ 60-70 wt%), is highly toxic to both environment and human health, resulting in a restriction of its use in many countries around the globe[7]. Therefore, a search for lead-free piezoelectric ceramics with comparable properties to that of PZT is crucial.

Among the available lead-free materials, the solid solution between rhombohedral $Bi_{0.5}Na_{0.5}TiO_3$ (BNT) and tetragonal $BaTiO_3$ (BT), (1–*x*)BNT–*x*BT, has received much attention due to its superior ferroelectric and piezoelectric properties at the MPB around $x$ = 0.055-0.07, similar to what observed in PZT [8] [9]. Acceptor doping have also been investigated extensively in BNT-based systems by adopting typical A- and B-site acceptor dopants used in PZT. However, B-site acceptor doped BNT-based ceramics only displayed a slight or moderate

hardening characteristics. For examples, independent studies of $Fe_2O_3$-doped BNT [10] and BNKT exhibited only a small increase in coercive field ($E_c$) [11] even though the defect dipoles responsible for hardening characteristics were clearly detected,. Likewise, Sapper *et al.* [12] reported a small or absence of aging effects in 1 at% Fe doped (1-*x*)BNT-*x*BT (*x* = 0.01). The less pronounced hardening and aging effects were attributed to the relaxor nature of BNT-based materials, which makes stabilized domain volume smaller than that of the ferroelectric PZT. Similarly, hard-type characteristics like an increase in $E_c$ or internal bias field were very difficult to discern in Fe-doped 92BNT-6BT-2KNN [13] due to the constricted *P-E* hysteresis loop arising from the ergodic relaxor nature of the base composition. Meanwhile, though an increase in $Q_m$ was observed in a study of Mn-doped 92BNT-BT [14], a conclusion that it was a hardening characteristic from microscopic origin cannot be made as the microstructure and density also changed.

Compared to their B-site counterpart, the amount of reports on hardening characteristics due to A-site modifications are relatively small. Most of previous works mainly focused on the effects of A-site nonstoichiometry on the electrical conductivities and leakage currents since both Bi and Na are volatile elements and tend to escape during high temperature sintering [15] [16] [17] [18]. Lately, after oxygen vacancies have been revealed to be the dominant conduction species in Bi-deficient BNT [16], attention has also been paid toward the development of BNT as oxide ion conductor through A-site acceptor doping [19]. Though the number of studies based on A-site acceptor-doped BNT-based systems are very limited, satisfactory hardening characteristics due to A-site modifications (through adjusting Bi/Na ratio) were recently shown in a comprehensive study of (1-*x*)BNT–*x*BT at the compositions near the MPB (*x* = 5.5, 6 and 7 mol%) [20]. All “hardening” characteristics including an increase in $E_c$, $Q_m$, as well as a decrease in $P_r$, $d_{33}$, $\varepsilon_r$, and tan $\delta$ were obtained in all Na-excess samples. Moreover, an increase in $E_c$ and a decrease in $P_r$ were further confirmed by remanent hysteresis measurements. Also, Yesner *et al.* [21] observed a drastic increase in $Q_m$ in Bi-deficient BNT-BKT-BT ceramics.

Given that hardening characteristics due to A-site stoichiometry modification exhibited promising results as compared to its B-site counterpart, it is very interesting to investigate whether the same or more pronounced hard-type characteristics could be obtained by other A-site acceptor dopants. To the best of our knowledge, there has been no report that systematically compare the effect of A-site and B-site acceptor dopants in (1–*x*)BNT–*x*BT at the MPB compositions. Therefore, in this study, the 0.93BNT-0.07BT, which was the MPB composition exhibiting the highest degree of hardening in previous study [20], will be chosen as a starting composition. The role of A-site Li and B-site Fe acceptor-doped 0.93BNT-0.07BT will be compared and investigated through systematic studies of crystal structure, dielectric, electrical conductivity, piezoelectric and ferroelectric properties. Due to the reported inconsistencies of doping effects between lead-free and PZT materials as well as the fact that comprehension of doping outcome is one of the key requirements for employing material in practical use, this study is expected to provide more understanding on the doping effect, particularly acceptor doping, at the MPB composition of BNT-BT, which is widely used as base composition in various studies.

## 2. Literature review

### 2.1 Hardening mechanism and associated defect chemistry

In perovskite oxide compounds e.g. $Pb(Zr_{0.5}Ti_{0.5})O_3$ and $BaTiO_3$, adjusting electrical properties for different applications is normally done via doping either by isovalent or aliovalent dopants on the A- and B- site. Typically, a small amount of dopants on the order of 1-2 at% can induce the materials properties to possess “softening” or “hardening” characteristics. Examples of typical donor and acceptor dopants used are shown in Table 2.1.

**Table 2.1** Common aliovalent dopants in $Pb(Zr_{0.5}Ti_{0.5})O_3$ and $BaTiO_3$ [2]

| | |
|---|---|
| A-site donors | $La^{3+}$, $Bi^{3+}$, $Nd^{3+}$ |
| B-site donors | $Nb^{5+}$, $Ta^{5+}$, $Sb^{5+}$ |
| A-site acceptors | $K^{+}$, $Rb^{+}$ |
| B-site acceptors | $Co^{3+}$, $Fe^{3+}$, $Sc^{3+}$, $Ga^{3+}$, $Cr^{3+}$, $Mn^{3+}$, $Mn^{2+}$, $Mg^{2+}$, $Cu^{2+}$ |

While softening characteristics are induced via doping with higher valence cations, hardening characteristics, on the other hand, can be achieved by doping with acceptor dopants or lower valence cations (e.g. $Fe^{3+}$ replacing $Ti^{4+}/Zr^{4+}$ or $K^{+}$ replacing $Pb^{2+}$). Acceptor doping results in a formation of negatively charged defects in the material. And in order to maintain charge neutrality, one of these three positively charged defects will be generated: 1) cation interstitials, 2) anion vacancies or 3) holes. The preferable type is determined thermodynamically. For example, an incorporation of acceptor $Fe_2O_3$ or CuO dopants into $PbTiO_3$ causes the formation of negatively charged defects (e.g. $Fe'_{Ti}$ $Cu''_{Ti}$) together with the compensating oxygen vacancies ($V_O^{\cdot\cdot}$) (i.e. anion vacancies) as following:

$$Fe_2O_3 \xrightarrow{2PbTiO_3} 2Fe'_{Ti} + 3O_O^X + V_O^{\cdot\cdot} \quad (1)$$

$$CuO \xrightarrow{PbTiO_3} Cu''_{Ti} + O_O^X + V_O^{\cdot\cdot} \quad (2)$$

These mobile charged defects alone (e.g. $Fe'_{Ti}$, $Cu''_{Ti}$ and $V_O^{\cdot\cdot}$) or in the form of defect dipoles (i.e. a couble between negatively charged defects and positively charge defects, e.g. $Fe'_{Ti} - V_O^{\cdot\cdot}$) can stabilize domain configurations, and subsequently lead to a decrease of domain wall contributions to the polarization response. Consequently, the materials show hardening characteristics, which include a moderately lowered electrical resistivity (i.e. high conductivity), a decrease in the piezoelectric coefficient, $\varepsilon_r$ and tan $\delta$, as well as an increase in $Q_m$ and $E_c$ and aging effects.

So far, three mechanisms have been proposed to explain the origin of the stabilized domain configurations (see Fig. 2.1) : (1) *grain boundary effects* [22] [23], which is a diffusion of charged defects to grain boundaries, resulting in internal bias fields that pin polarization orientation; (2) *domain wall effects* [24] [25], which is the diffusion of charged defects to the domain wall area, thus impeding domain wall movement and (3) *volume or bulk effects* [5], which is an alignment of defect dipoles along the spontaneous polarization ($P_s$) within domains.

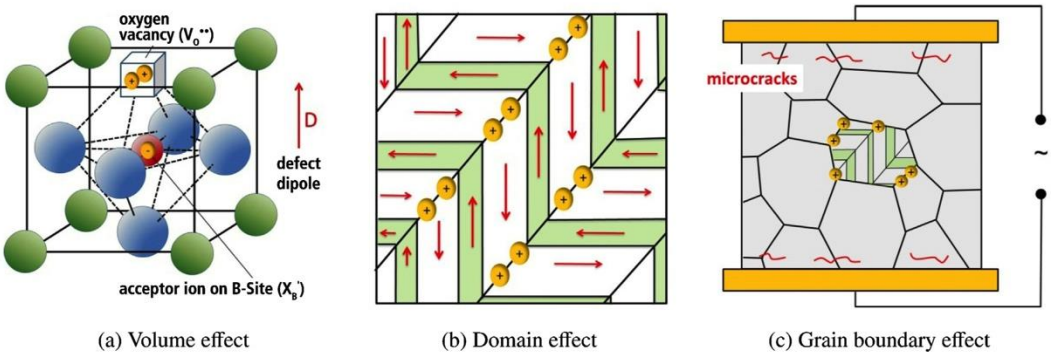


**Fig. 2.1.** Schematic illustration showing the proposed domain stabilization mechanisms, (a) volume effect, (b) domain effect and (c) grain boundary effect (figure taken from [26])

Among the proposed mechanisms, *volume effect* model is the most widely accepted one. In this model, defect dipoles (e.g $Fe'_{Ti} - V_O^{\cdot\cdot}$) may randomly align along one of the possible directions when the sample is in its high temperature paraelectric cubic phase (see Fig. 2.2(a)). As the sample cools down to the paraelectric-ferroelectric phase transition, the defect dipoles will tend to align along the spontaneous polarization directions allowed by the symmetry of the phase in order to minimize their potential energy e.g <001> directions for the tetragonal phase (see Fig. 2.2 (b)) or <111> directions for the rhombohedral phase (see Fig. 2.2(c)). This spontaneous realignment of the defect dipoles is known as the aging process. The aging time is, therefore, the time that the defect dipoles need for aligning themselves along the $P_s$. Aging time is material and temperature dependent. Normally, the higher the temperature is, the

shorter the aging time will be. For example, the aging time of $BaTiO_3$ is 5 days at 80°C and 28 days at room temperature [27].

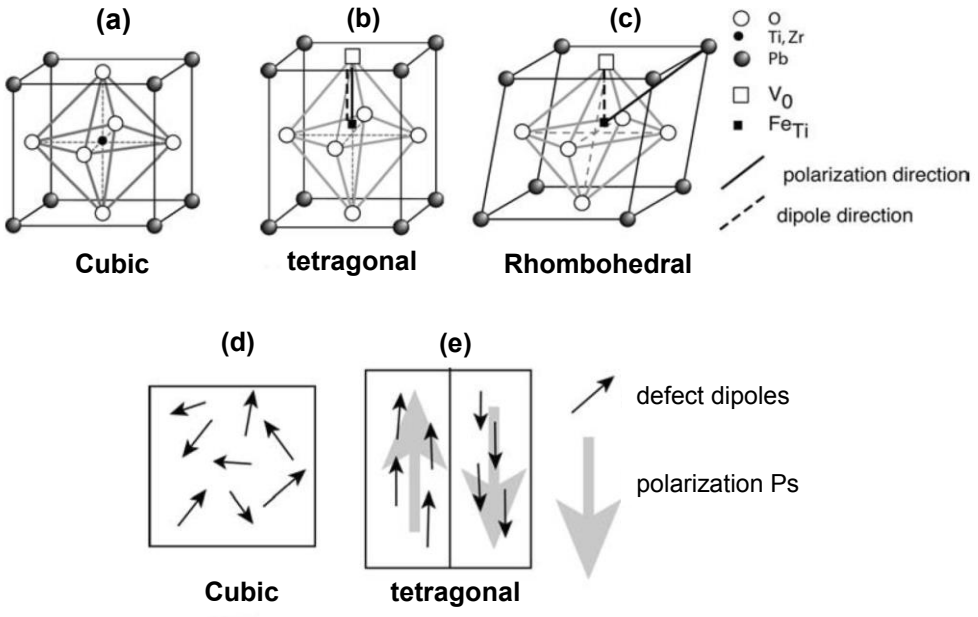


**Fig. 2.2.** Defect dipoles and spontaneous polarization ($P_s$) direction in (a) cubic, (b) tetragonal and (c) rhombohedral unit cell of a perovskite crystal. In (b) and (c), the *dotted* and *solid* line represent a defect dipole and a spontaneous polarization direction, respectively. Schematic representations exhibit corresponding defect dipoles and Ps in (d) cubic (randomly aligned) and (e) tetragonal (preferentially aligned along $P_s$) (figure adapted from [28])

In unpoled ceramics, aging will result in a pinched or constricted *P-E* hysteresis loop, as shown in Fig. 2.3 (a). In contrast, if the ceramic is poled at high enough temperature (but below $T_c$) and at electric field levels that are sufficient to reorient the defect dipoles and $P_s$, the shifting of whole *P-E* hysteresis under an alternating field will be observed, as shown in Fig. 2.3 (b).

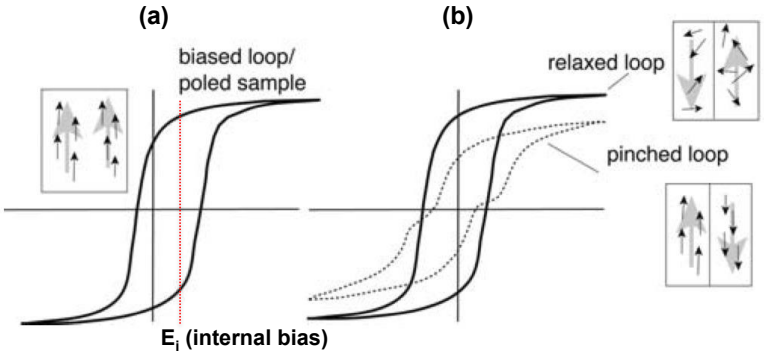


**Fig. 2.3.** *P-E* hysteresis loop in hard rhombohedral PZT ceramics (a) *P-E* loop of poled sample showing internal bias field ($E_i$) (b) a pinched loop in aged sample and a symmetric or relaxed loop after deaging (figure adapted from [28])

## 2.2 A-site modification studies in BNT-based systems

Since Bi and Na on the A-site are volatile elements, the A-site vacancies in BNT and BNT-BT are likely to be formed during sintering. This essentially makes the stoichiometry of the sintered compositions different from the expected stoichiometry. The effects of A-site non-stoichiometry on the physical, dielectric and piezoelectric properties as well as the crystal structure reported in the literatures are summarized below.

Hiruma *et al*. [15] studied the effect of Bi and Na non-stoichiometry according to the chemical formula $Bi_{0.5(1+x)}Na_{0.5}TiO_{3-0.75x}$ and $Bi_{0.5}Na_{0.5(1+y)}TiO_{3-0.75x}$, which is denoted as BNT-Bi(*x*), BNT-Na(*y*) and *x, y* = -0.01, -0.02 and 0.01. The results showed a decrease in dielectric loss (decreased conductivity) in samples that possessed either excess in Bi (e.g. BNT-Bi(0.01) or deficient in Na (e.g. BNT-Na(-0.01) BNT-Na(-0.02)). In contrast, an increase in dielectric loss (increased conductivity) was observed in samples with either deficient in Bi (e.g. BNT-Bi(-0.01)) or excess in Na (e.g. BNT-Na(0.01)). Due to an improvement of dielectric properties in samples with Bi/Na > 1.0 and a general degradation of that in samples with Bi/Na < 1.0, it was proposed that Bi vaporization during the high sintering temperatures was the primary reason for the deteriorations in properties. However, the effects on ferroelectric properties especially hardening and softening characteristics haven't been mentioned.

Similarly, Zuo *et al*. [29] also reported the effects of A-site nonstoichiometry in BNT but in this study both Bi and Na were changed by the same amount (i.e. $(Bi_{0.5}Na_{0.5})_{1+x}TiO_3$ $x$ = -0.02, -0.01, -0.005, 0, 0.005, 0.01). Samples with A-site deficiency resulted in relatively high dielectric loss (i.e. high conductivity) compared to that of A-site cation excess samples. This confirmed that the A-site vacancies formed during sintering are responsible for the high conductivity of BNT ceramics. However, the ferroelectric properties were largely unaffected by the A-site nonstoichiometry since *P-E* hysteresis loops for both A-site deficient and A-site excess samples remained the same as seen in Fig. 2.4 below.

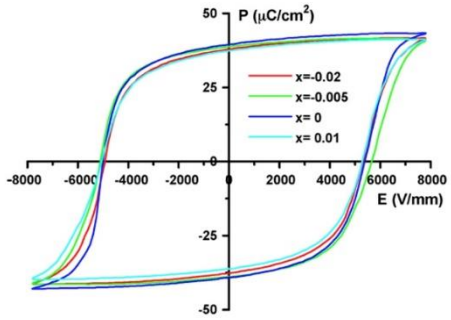


**Fig. 2.4.** Polarization versus electric field hysteresis loops of $(Bi_{0.5}Na_{0.5})_{1+x}TiO_3$, $x$ = -0.02, -0.01, - 0.005, 0, 0.005, 0.01

Sung *et al*. [30] [18] studied the effects of Na and Bi nonstoichiometry in $(Bi_{0.5}Na_{0.5})TiO_3$. When the degree of Na deficiency increased, a decrease in $T_d$ but an increase in $d_{33}$ was observed. In contrast, as the degree of Bi deficiency increased, an increase in $T_d$ but a decrease in $d_{33}$ was observed.

Li *et al.* [16] reported a thorough study on the effect of Bi and Na non-stoichiometry in BNT by using impedance spectroscopy and other techniques. Compared to stoichiometric composition, the impedance data revealed that BNT with excess Bi (i.e. $NBi_{0.51}T$) or deficient Na ($Na_{0.49}BT$) exhibited an increase in resistivity by 3-4 orders of magnitude. Moreover, the dependence of the bulk resistivity on the oxygen partial pressure ($pO_2$) and the value of activation energy of 1.66 eV (~ ½ $E_g$) suggested n-type electronic conduction as the primary conduction mechanism for these highly insulating samples. In contrast, for samples with a deficiency in Bi ($NBi_{0.49}T$) or excess in Na ($N_{0.51}BT$), a decrease in total resistivity and a grain

boundary resistivity, which was a strong function of $pO_2$, together with the results from electromotive force measurements revealed that the conduction mechanism was dominated by $V_O^{\cdot\cdot}$. Figure 2.5 shows Arrhenius type plots of the bulk conductivity for resistive samples (i.e. samples with excess Bi or deficient Na, Bi/Na > 1.0) and conductive samples (i.e. samples with deficient Bi or excess Na, Bi/Na < 1.0).

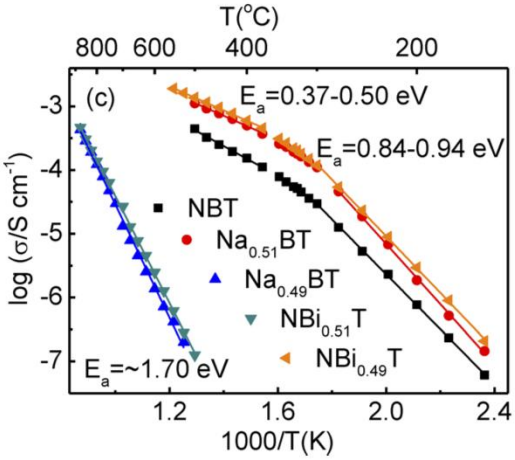


**Fig. 2.5.** Arrhenius type plots of bulk resistivity showing a similar behaviour between excess Bi and deficient Na sample (blue and green line, $E_a$ ~ 1.70 eV). Similar conducting behaviour between deficient Bi and excess Na is also observed (orange and red line). (figure taken from [16])

Another study from Li *et al*. [31] also highlighted the importance of the pre-drying step of the hygroscopic $Na_2CO_3$ starting reagent prior to processing. The adsorbed water in undried $Na_2CO_3$ powder has shown to result in a significant change in the stoichiometry of Na, and thus giving similar electrical properties to that of Na-deficient sample.

Recently, Prasertpalichat *et al.* [20] studied the effects of A-site acceptor (through excess Na) and donor (through excess Bi) doping in (1-*x*)BNT-*x*BT at the compositions near the MPB (*x* = 5.5, 6 and 7 mol%). Compared to the stoichiometric compositions, A-site acceptor-doped compositions displayed a significant increase in coercive field ($E_c$), which is an indication of domain wall pinning in typical hard PZT as shown in Fig 2.6. Moreover, the results were further confirmed via remanent polarization hysteresis analyses and the same trend still persisted as seen in Fig 2.7, thus confirming that the observed increase in $E_c$ is true phenomena not a misleading result from conduction or leakage currents

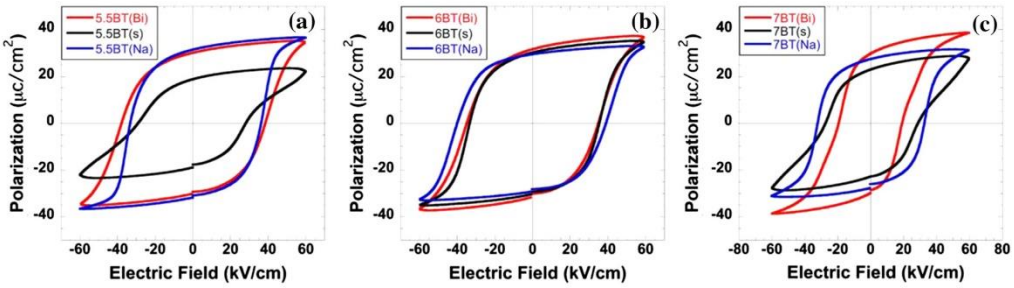


**Fig. 2.6.** Standard *P-E* hysteresis loops of donor (Bi) stoichiometric (s) and acceptor (Na) doped (1-*x*)BNT-*x*BT where *x* = 0.055, 0.06 and 0.07 measured at room temperature with a frequency of 1 Hz (figure taken from [20])

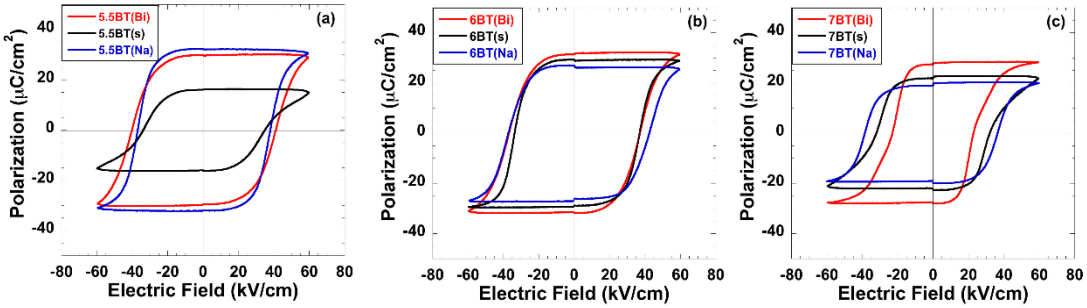


**Fig. 2.7.** Remanent *P-E* hysteresis of donor (Bi), stoichiometric and acceptor (Na) doped (1-*x*)BNT-*x*BT (*x* = 0.055, 0.06 and 0.07) (figure taken from [20])

## 3. Objectives

3.1 To compare the effects of A-site ($Li^+$) and B-site ($Fe^{3+}$) acceptor dopants on hardening characteristics of $0.93Bi_{0.5}Na_{0.5}TiO_3$-$0.07BaTiO_3$ lead free piezoelectric ceramics.

3.2 To study the conduction mechanism of A-site ($Li^+$) and B-site ($Fe^{3+}$) acceptor dopants by using impedance spectroscopy technique.

## 4. Experimental and calculational details

### 4.1 Sample preparations.

Ceramic samples based on the compositions $(Bi_{0.465}Na_{0.465}Ba_{0.07})_{1-x}Li_xTiO_3$ (abbreviated as Li100*x*), for A-site Li doping, and $(Bi_{0.465}Na_{0.465}Ba_{0.07})Fe_xTi_{1-x}O_3$ (abbreviated as Fe100*x*), for B-site Fe doping, where $x = 0\text{-}0.03$, were prepared via conventional solid state mixed oxide route. Reagent-grade powders of $Bi_2O_3$ (99.9%, Sigma Aldrich), $Na_2CO_3$ (99.95%, Alfa Aesar), $TiO_2$ (99%, Sigma Aldrich), $BaCO_3$ (99.9%, Alfa Aesar), $Li_2CO_3$ (99%, Merck) and $Fe_2O_3$ (99%, Sigma Aldrich), were used as starting chemicals. The starting materials were weighted according to the required chemical formula and then ball-milled in ethanol with yttrium-stabilized zirconia as a media for 24 h before subsequently dried in the oven for 24 h. After that, the milled powders were calcined at 800°C and followed by re-milling and drying step to ensure that the achieved powders were in sub-micron sized range. The obtained powders were then mixed with 3 wt% polyvinyl butyral (PVB) and pressed into disc pellets with 15 mm in diameter. The pellets were sintered at temperature between 1150 to 1175°C in a covered crucible for 2 h with a polymer burned out step at 400°C for 3 h. It should be noted that all green pellets were embedded in sacrificial powders of the same composition in order to minimize the loss of the volatile Bi and Na components during sintering.

### 4.2 Sample Characterizations.

Phase purity and crystal structure were identified by X-ray diffraction (XRD, Bruker D8 Advance) on crushed sintered ceramics using Cu $K\alpha$ radiation. Two sets of scans were performed, one with an addition of NaCl as internal standard in the $2\theta$ range of 10º-80º with a

0.02º step-size and 1 s/step scan speed. The other scan was without standard in the range 10º-120º with a 0.02º step-size and 2 s/step scan speed. The obtained XRD data were further analyzed by using the Le Bail and Rietveld refinement technique via the TOPAS software. Then the synchrotron x-ray absorption near edge structure (XANES) spectroscopy were conducted on BNBT-*x*Fe samples at ambient temperature at XAS beam line (BL5.2 SUT-NANOTECT-SLRI) of Synchrotron Light Research Institute (SLRI), Thailand, with provided electron energy of 1.2 GeV and beam current of 140-80 mA. The Ti and Fe *K*-edge XANES spectra were measured in the fluorescent mode and the signals were collected by using a four-element Si drift detector. A double crystal monochromator Ge(220) was used to scan the photon energy. For Ti and Fe K-edge XANES measurements, the scanning step was set at 0.2 eV in the photon energy range of 4500-5400 eV and 7100-7200 eV, respectively. The normalized XANES data were processed and analyzed after background subtraction in the pre-edge and post-edge region using the ATHENA software. The linear combination analysis (LCA) method in the ATHENA program as implement in IFEFFIT package was used for the data fitting [32].

Prior to electrical measurements, samples were ground and polished to ~0.7-0.8 mm thick and then silver paste (Heraeus C1000) was applied on both sides and fired at 700°C for 0.5 h. The temperature and frequency dependence of dielectric properties were measured by Agilent 4263B LCR Meter on poled samples. It's worth noting that all samples were poled by applying a dc electric field at 50 kV/cm for 0.5 h at room temperature. The impedance spectroscopy was conducted over a wide temperature (~460-540°C) and frequency range (20 Hz-10MHz) using Keysight impedance gain/phase analyzer (model 4194A). The electric field induced polarization (*P*-*E*) and strain (*S*-*E*) measurements were measured by using a Precision Premier II, Radiant technology. The low field piezoelectric coefficient ($d_{33}$) was measured using a YE2730A d33 meter.

## 5. Results and discussion

### 5.1 Crystal structure and phase fraction determination by XRD and Rietveld refinement

Figure 5.1(a) displays room temperature X-ray diffraction (XRD) patterns of BNBT–*x*Li and BNBT–*x*Fe (*x* = 0, 0.01, 0.02 and 0.03) crushed sintered pellets. It is noteworthy that NaCl was used as an internal standard to obtain a better determination of lattice parameter changes due to Li and Fe doping. Thus, apart from the peaks corresponding to NaCl (marked with asterisk (*) in Fig. 5.1(a)), it can be seen that all samples exhibited a single-phase perovskite structure with no trace of any secondary phases, suggesting that $Li^{+}$ and $Fe^{3+}$ ions diffused into lattice site and form a complete solid solution with BNBT. For pure BNBT (i.e. 0.93BNT-0.07BT), the rhombohedral characteristic (111) peak at $2\theta \sim 40^{\circ}$ (Fig. 5.1(b)) and tetragonal characteristic (200) reflection at $2\theta \sim 46^{\circ}$ (Fig 5.1(c)) displayed a single broad peak with no visible shoulder or peak splitting, indicating that the prepared BNBT possessed pseudocubic structure. The result is consistent with previous studies in which the average structure of (1-*x*)BNT-*x*BT at the MPB compositions (*x*=0.055-0.07) were reported to be near cubic [33] or pseudocubic with a minor tetragonal and rhombohedral distortion [34] [35]. In case of Li-doped BNBT ceramics, a single broad (111) and (200) peaks persisted up to *x*=0.02 (Li2). However, when *x* reached 0.03 (Li3), the (111) peak became broader and a small but noticeable bump on the higher angle was started to be observed; meanwhile, the (200) peak also broadened, implying that the degree of tetragonal and rhombohedral distortion increased. In addition, it was found that the peaks shifted toward higher $2\theta$ with increasing Li doping. This indicates that the lattice site is reduced, which can be attributed to a smaller ionic radii of $Li^{+}$ ion ($\sim$ 1.20 Å) [19] [36] as compared to that of $Bi^{3+}$ (1.38 Å), $Na^{+}$ (1.39 Å) and $Ba^{2+}$ (1.61 Å) [37] on the A-site. On the other hand, for BNBT-*x*Fe ceramics (*x*=0.01-0.03), neither shoulder nor peak splitting of (111) and (200) peaks were observed across the entire range of Fe doping level studied, suggesting that pseudocubic structure persisted in all Fe-doped BNBT ceramics and that Fe doping had little to no effect on the structural changes. Besides, a relatively small

downward peak shift, which indicates an expansion of unit cell volume, was detected upon increasing Fe doping level and it can be ascribed to a larger ionic radius of $Fe^{3+}$ (0.645 Å) that substitutes for $Ti^{4+}$ (0.605 Å) [37]. The results are well consistent with previous reports on Fe-doped BNKT [11] and 0.94BNT-0.06BT ceramics [38] in which a slight peak shift were also reported. A less pronounced peak shift in Fe-doped BNBT ceramics may arise from a smaller difference between ionic radii of $Fe^{3+}$dopant and $Ti^{4+}$host ion on B-site in comparison to those on the A-site ($Li^{+}$ Vs $Bi^{3+}$, $Na^{+}$ and $Ba^{2+}$).

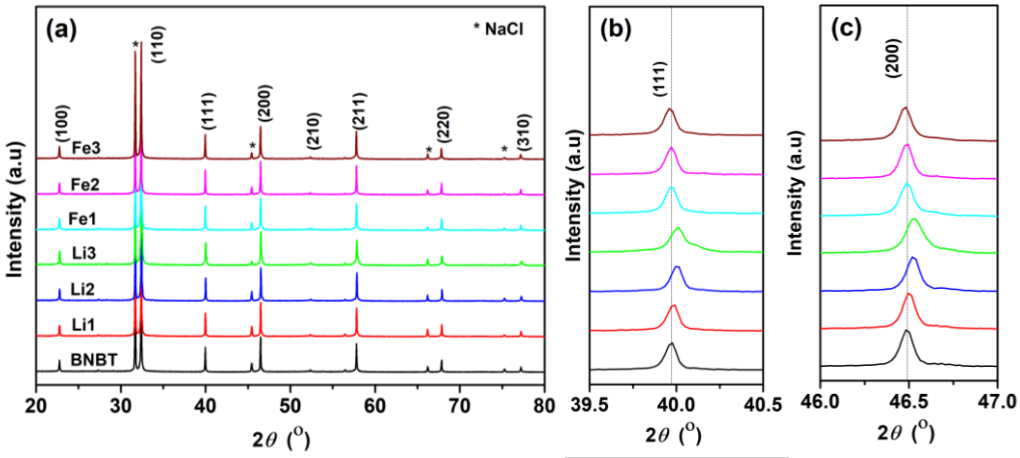


**Fig. 5.1.** Room temperature XRD patterns of BNBT-*x*Li and BNBT-*x*Fe ceramics (*x* = 0, 0.01, 0.02 and 0.03) in the $2\theta$ range of (a) 20-80° (b) 39.5-40.6° and (c) 46.0-47.0°

Since the base composition (0.93BNT-0.07BT) in this study is at the MPB where two phases coexist, Rietveld refinement technique was performed on all samples' XRD data to provide more insight on the effect of Li and Fe doping on structural change especially the phase fraction, which have been shown to have a significant effect on the electrical properties. For the present study, the use of two-phase model consisting of rhombohedral (space group *R3c*) and tetragonal (space group *P4bm*) phases provided the optimum fit, consistent well with previous reports of similar compositions [39] [40]. In addition, it's worth noting that two sets of refinement were performed in this study. First, the accurate cell parameters of both phases were obtained from a Le Bail refinement using XRD patterns collected with internal standard addition (i.e. NaCl). Then, the obtained values were fixed in Rietveld refinement so that the

number of correlated parameters was minimized. The structural information obtained from [41] was used as a starting model. Background data was refined by using Chebyshev function with six polynomial coefficients whereas the atomic occupancies were assumed to be equal to the chemical formula of each composition and were not refined. The calculated profile from Rietveld refinement along with corresponding experimental XRD data of BNBT-*x*Li and BNBT-*x*Fe ceramics are demonstrated in Fig. 5.2. Related refinement data including phase fraction, lattice parameters and fitting quality values are listed in Table 5.1. The reliability factors (see Table 5.1) and the good fit between calculated and observed data (see Fig. 5.2.) indicate that the samples are well described by the refined models. For BNBT (i.e. undoped 0.93BNT-0.7BT) the refined phase fraction of *R3c* and *P4bm* were 84.11% and 15.89%, respectively, which correspond well with previous results obtained from the refinement of both laboratory (93% *R3c*+7% *P4bm*) [39] and high-resolution XRD data (77.7% *R3c*+22.3% *P4bm*) [41]. With increasing either Li or Fe doping level (*x*) from 0.01 to 0.03, it was found that the *R3c* phase fraction changed in the range of ∼79%–85% and that of *P4bm* varied between ∼15 to ∼21%, respectively. This relatively small change of both *R3c* and *P4bm* phase fraction (i.e. less than ±5% variation) as compared with the base composition BNBT suggests that both A-site (Li) and B-site (Fe) acceptor doping had little or no influences on the constituent phases. Previous studies from Xu *et al*. [40] observed a substantial change of phase fraction from 49.5% *R3c*+50.5% *P4bm*, for $x = 0$, to 24.8% *R3c*+75.1% *P4bm*, for $x = 0.10$, in (1-*x*)(BNT-BT)-*x*$NaTiO_3$ ceramics. Similar phenomenon was also observed in Li-doped BNT-BT-*x*$CaTiO_3$ [39], in which a variation from 93% *R3c*+7% *P4bm* ($x = 0$) to 43% *R3c*+57% *P4bm* ($x = 0.15$) was reported. Thus, a fairly small change in phase fraction in this study may be ascribed partly to a lesser amount of doping ($x \leq 0.03$) compared to that of previous reports ($x \sim 0.10$ or 0.15). Nevertheless, it was observed that the changes in unit cell volume, obtained from the refinement, agreed well with the observed XRD peak shift in Fig. 5.1 where both *R3c* and *P4bm* unit cell volume gradually decreased with increasing Li content while they continuously increased upon increasing Fe dopant.

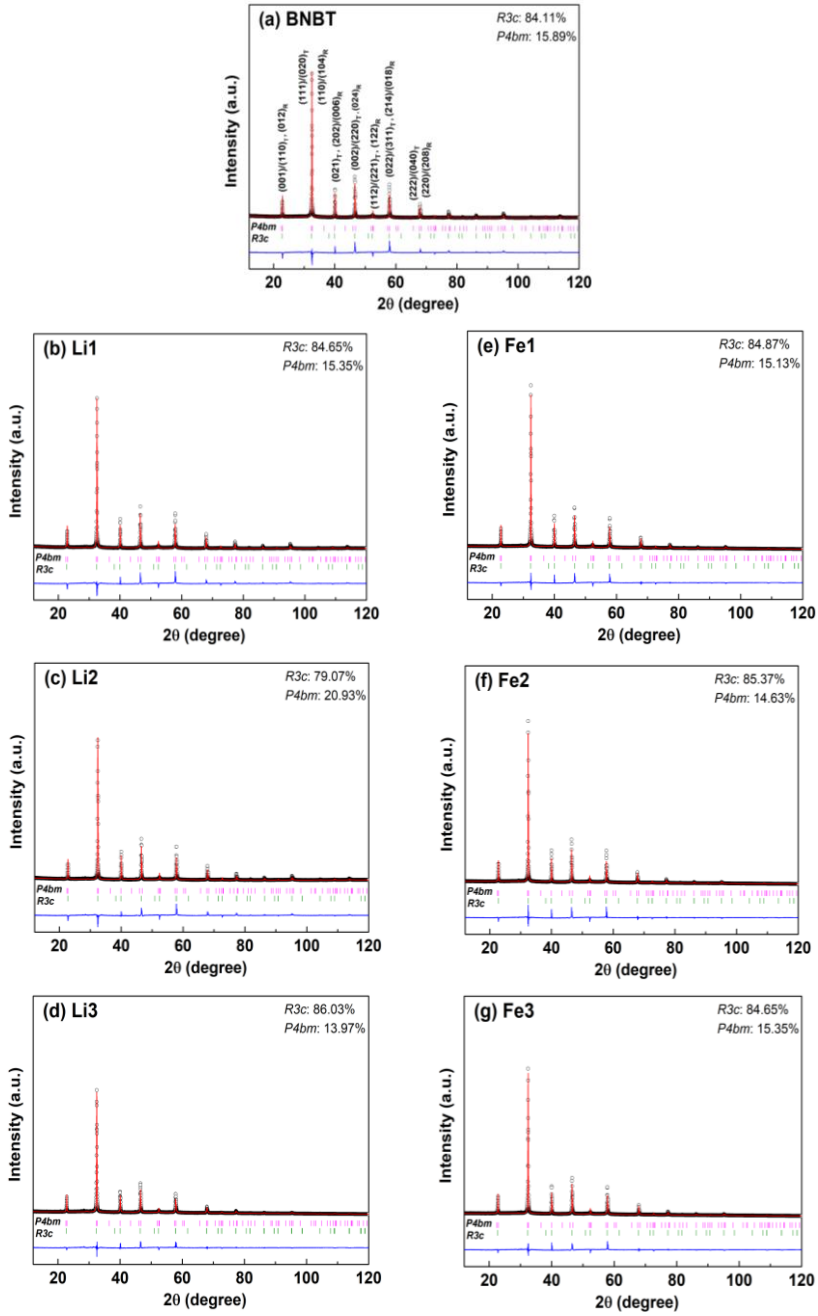


**Fig. 5.2.** Room temperature XRD patterns of BNBT-*x*Li and BNBT-*x*Fe ceramics, $x$ = 0.01-0.03. The black circles represent experimental data and the red lines correspond to the calculated profile from Rietveld refinement. The blue lines are differences between the experimental and the refined diffraction patterns. The allowed Bragg reflections for *P4bm* and *R3c* space groups are indicated by pink and green ticks, respectively.

**Table 5.1** Phase fraction, calculated lattice parameters and fitting quality values of BNBT-*x*Li and BNBT-*x*Fe samples obtained from the Rietveld refinement of room-temperature XRD data.

| | Phase fraction (%) | | *R3c* | | | *P4bm* | | | $\%R_{wp}$ | $\%R_p$ |
|---|---|---|---|---|---|---|---|---|---|---|
| | *R3c* | *P4bm* | a (Å) | c (Å) | vol ($Å^3$) | a (Å) | c (Å) | vol ($Å^3$) | | |
| BNBT | 84.1 | 15.9 | 5.5219(2) | 13.526(1) | 357.2 | 5.4904(4) | 3.9498(4) | 119.1 | 11.27 | 8.24 |
| Li1 | 84.7 | 15.3 | 5.5206(2) | 13.523(1) | 356.9 | 5.4877(4) | 3.9511(4) | 119.0 | 11.47 | 8.37 |
| Li2 | 79.1 | 20.9 | 5.5187(2) | 13.517(1) | 356.5 | 5.4929(4) | 3.9430(4) | 119.0 | 10.89 | 8.02 |
| Li3 | 86.0 | 14.0 | 5.5196(2) | 13.510(1) | 356.4 | 5.4953(3) | 3.9376(3) | 118.9 | 11.88 | 8.39 |
| Fe1 | 84.9 | 15.1 | 5.5225(2) | 13.526(1) | 357.3 | 5.4918(3) | 3.9523(4) | 119.2 | 12.06 | 8.31 |
| Fe2 | 85.4 | 14.6 | 5.5226(2) | 13.527(1) | 357.3 | 5.4907(4) | 3.9541(4) | 119.2 | 12.59 | 8.78 |
| Fe3 | 81.0 | 19.0 | 5.5241(2) | 13.530(1) | 357.6 | 5.4950(4) | 3.9494(4) | 119.3 | 11.94 | 8.26 |

### 5.2 Structural information, Valence state and local environment of BNBT-*x*Fe

The synchrotron x-ray absorption near edge structure (XANES) spectroscopy is an element specific technique that can probes the absorption edge of the desired element to gain structural information about its valence state and local environment. This technique can thus be used to identify the lattice site of an atomic species, e. G. A dopant, in a known matrix [42] [43]. The measured Ti and Fe *K*-edge XANES spectra measured for BNBT and BNBT-xFe ceramics are compared with standard $TiO_2$ ($Ti^{4+}$) and $Fe_2O_3$ ($Fe^{3+}$) powders, as shown in Fig. 5.3(a) and 3(b), respectively. Under most circumstances, XANES also allows for the determination of cation valences. The higher the oxidation number, the further the position of absorption edge is shifted toward higher energies as compared to the neutral metallic state. As indicated by XANES spectra in Fig. 5.3, the position of absorption edge at Ti *K*-edge of all samples resembles that of the $TiO_2$ standard, showing that Ti species in all samples is $Ti^{4+}$, as expected. For Fe K-edge, one can easily see that the edge position of all BNBT-*x*Fe ceramics is higher than that of the $Fe^{3+}$ at approximately 7126 eV. Thus, this result indicates that the majority Fe ions in our samples possessed the mixed valence state of $Fe^{3+}$ and $Fe^{4+}$. Moreover, all the spectral feature of Fe K-edge also look similar to those of Ti K-edge of BNBT-*x*Fe ceramics, suggesting that the local structure surrounding Fe atoms in BNBT-*x*Fe ceramics is

similar to that of Ti atoms, which means Fe substituting for Ti in BNBT-*x*Fe ceramics. This result introduced oxygen vacancies leading to a distortion of the local symmetry.

To gain information about the local atomic structure and the size occupancy of Fe dopant in BNBT structure, calculation of XANES spectra was performed using the ab initio FEFF8.2 code with the self-consistent and full multiple-scattering options [44]. The spherical cluster size of electron wave function was increased until the spectra converged. The theoretical Ti and Fe K-edge XANES spectra, which correspond to BNBT-*x*Fe ceramics, were calculated in terms of a cluster derived from the average structure determined from our XRD result. Clusters with a size up to eight shells, containing at least 110 atoms, around the absorber (Ti and Fe atoms) were used to calculatethe XANES spectra based on BNBT *P4bm* and *R3c* crystallographic phases. The calculated XANES spectra of Ti and Fe substituting on the Ti site in BNBT *P4bm* and *R3c* structures are shown in Fig. 5.3(c) and (d), respectively. It is clear that the calculated XANES spectra are in very good agreement with the measured spectra of BNBT-*x*Fe ceramics, this implies that the local structure around Ti atom in BNBT-*x*Fe ceramics have a mixed phase between *P4bm* and *R3c* in a ratio of 20:80. This result is consistent with the phase fraction from our XRD analysis. Furthermore, calculation of Fe K-edge XANES spectra reveals that Fe dopant prefer to substitute on the Ti site of BNBT *R3c* structure, suggesting that the occupancy behavior of Fe dopant depend on doping level and preparation methods.

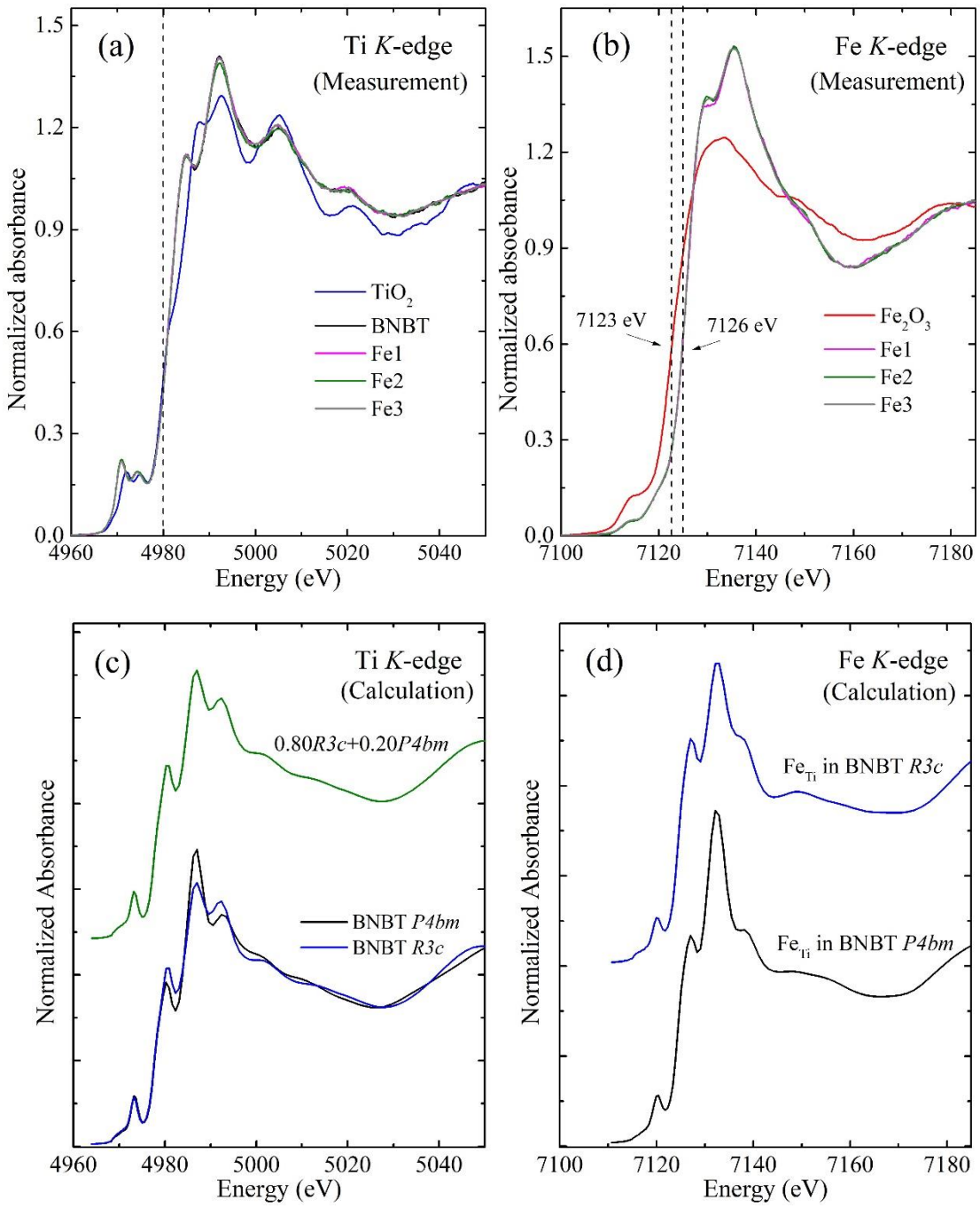


**Fig. 5.3**. Measured (a) Ti *K*-edge, (b) Fe *K*-edge XANES spectra of BNBT-*x*Fe ceramics with comparison to $TiO_2$ and $Fe_2O_3$ standards and calculated (c) Ti *K*-edge, (d) Fe *K*-edge XANES spectra of BNBT *P4bm* and *R3c* structures.

### 5.3 Microstructures

Fig. 5.4(a)–(g) illustrates SEM micrographs of BNBT-*x*Li and BNBT-*x*Fe (*x*=0-0.03) ceramics thermal etched at 1000$^{O}$C for 20 mins. All samples exhibited dense microstructure with a mixture of small and large irregular-sized grains. With increasing doping level (*x*), the average grain size calculated by using linear intercept method gradually increased from 0.68±0.11 μm (*x* = 0) to 0.99±0.13 μm (Li1), 1.23 ± 0.19 μm (Li2), and 1.25 ± 0.13 μm (Li3), for Li doping, and to 0.99 ± 0.16 μm (Fe1), 1.16 ± 0.15 μm (Fe2) and 2.10±0.29 μm (Fe3), for Fe doping. In this study, acceptor doping on A-site with Li or on B-site with Fe can cause negatively charged defects along with the compensating oxygen vacancies according to the following defect reactions:

$$Li_2O \xrightarrow{2(Bi_{0.465}Na_{0.465}Ba_{0.07})TiO_3} 2Li'_{(Bi_{0.465}Na_{0.465}Ba_{0.07})} + V_O^{\cdot\cdot} + O_O^X \quad (1)$$

$$Fe_2O_3 \xrightarrow{2(Bi_{0.465}Na_{0.465}Ba_{0.07})TiO_3} 2Fe'_{Ti} + V_O^{\cdot\cdot} + 3O_O^X \quad (2)$$

It's generally known that oxygen vacancy can help facilitate the mass transportation during sintering process and result in a promotion of grain growth [45]. Thus, a continuous increase in grain size with increasing Li and Fe doping level could be attributed to an increase in oxygen vacancy concentrations generated upon increasing doping content. Similar results were also observed in Li-doped BNKT [46] and BNT-KNN [47] as well as Mn-doped 0.94BNT-0.06$BiAlO_3$ [48].

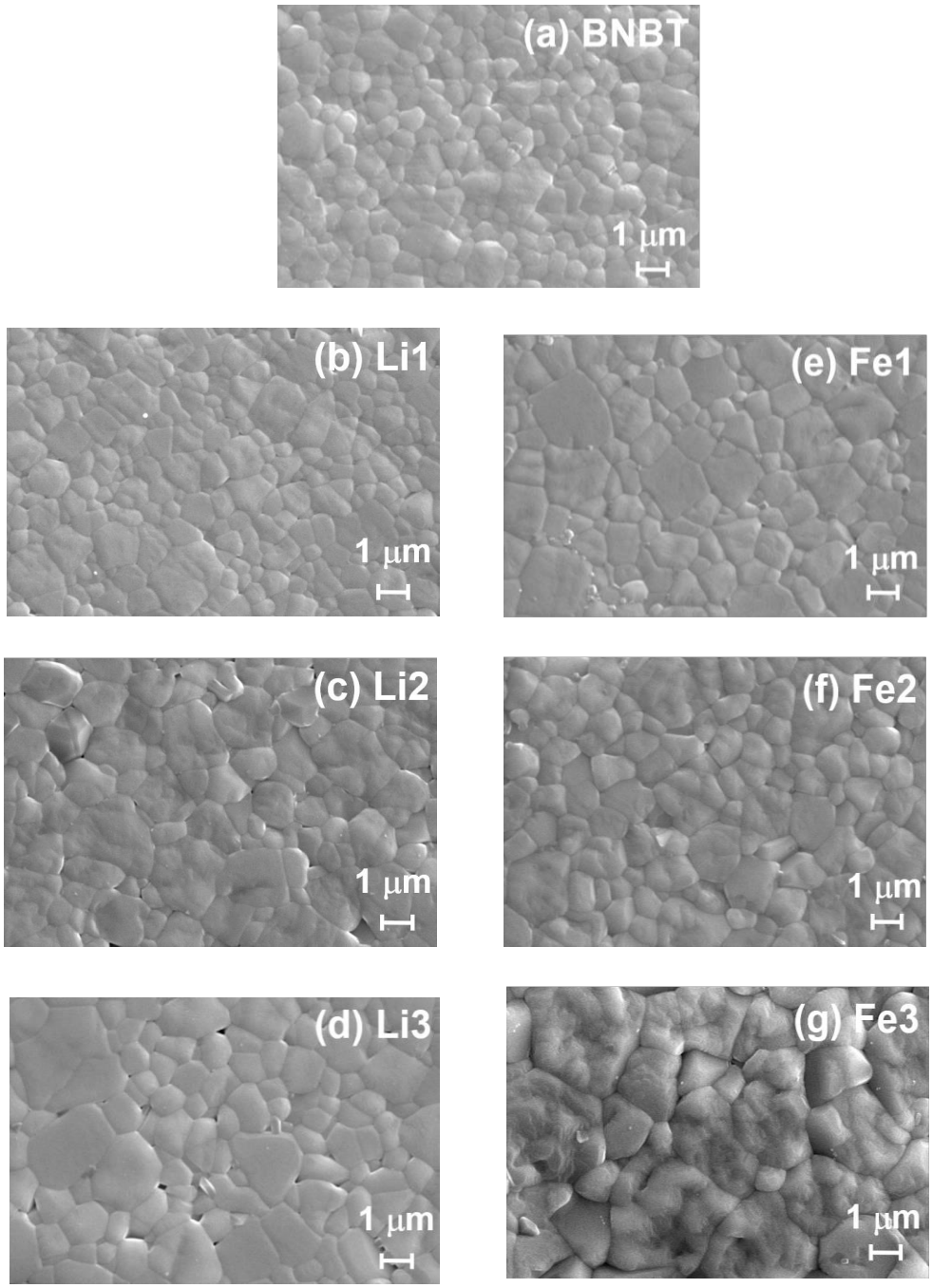


**Fig. 5.4.** SEM micrographs of BNBT-*x*Li and BNBT-*x*Fe ceramics (*x* = 0, 0.01, 0.02 and 0.03)

### 5.4 Dielectric properties

Temperature dependence of relative permittivity ($\varepsilon_r$) and loss tangent ($\tan\delta$) of poled BNBT-*x*Li and BNBT-*x*Fe ceramics measured from room temperature (RT) up to 450$^{\circ}$C at frequency of 1 Hz–100 kHz were illustrated in Fig. 5.5(a)–(g). For both BNBT-*x*Li and BNBT-*x*Fe ceramics, two dielectric anomalies were observed throughout the entire temperature and frequency range studied. The first one at the temperature of $T_m$ ~300$^{\circ}$C is characterized by maximum dielectric permittivity ($\varepsilon_{r,m}$) with frequency independent while another one at a lower temperature of $T_{F\text{-}R}$ (i.e. ferroelectric-to-relaxor transition temperature) is categorized by frequency-independent discontinuity peak in both $\varepsilon_r$–T and $\tan\delta$–T curves (indicated by arrow in Fig. 5.5(a)–g)). The origin of $T_m$ has been recently accepted to arise from two successive processes that occur upon increasing measuring temperature: (1) a transition from rhombohedral (*R3c*) to tetragonal (*P4bm*) polar nanoregions (PNRs) and (2) a relaxation of *P4bm* PNRs emerged from *R3c* [49] [50]. Meanwhile, the origin of $T_{F\text{-}R}$ is ascribed to a breakdown of electric-field-induced ferroelectric order from the non-ergodic relaxor (NER) state (i.e. a state where materials irreversibly transform into ordered FE domain under applied electric field and sustain even E-field is removed) into ergodic relaxor (ER) upon heating the materials [49] [51]. The temperature and frequency dependence of dielectric properties in this study corresponded well to the proposed framework.

To better compare the effects of A-site (Li) and B-site (Fe) acceptor doping on dielectric properties, extracted parameters from $\varepsilon_r$–T curves (at 1 kHz) including $T_{F\text{-}R}$, $T_m$, $\varepsilon_{r,m}$, room temperature $\varepsilon_r$ ($\varepsilon_{r,RT}$) along with their corresponding $\tan\delta$ are listed in Table 5.2. From Table 5.2, it can be seen that $T_{F\text{-}R}$ significantly increased from 26$^{\circ}$C (BNBT) to 37$^{\circ}$C, 67$^{\circ}$C and 97$^{\circ}$C for Li1, Li2 and Li3, respectively, while it moderately increased to 36$^{\circ}$C (Fe1) and 45$^{\circ}$C (Fe2) before slightly dropped to 41$^{\circ}$C (Fe3). The $T_{F\text{–}R}$ is known to be correlated with the stability of ferroelectric order (i.e. the higher the $T_{F\text{-}R}$ is, the stronger domain configuration the material possesses) [52]. And it is widely accepted that the oxygen vacancies can stabilize the ferroelectric domain in perovskite oxide materials [53]. Thus, an upward shift of $T_{F\text{–}R}$ with

increasing either Li or Fe acceptor doping level in this study is most likely be a result of an increase in oxygen vacancy concentration which is generated according to the abovementioned defect reactions (equation (1) and (2)). Similar results have also been reported in other acceptor-doped BNT-based ceramics including $(Bi_{0.47}Na_{0.47}Ba_{0.06})Ti_{1-x}Fe_xO_{3-\delta}$ ($x$ = 0–0.03) [38] and $Bi_{1/2}(Na_{0.8}K_{0.2})_{1/2}(Ti_{1-x}Fe_x)O_{3-x/2}$ ($x$ = 0–0.03) [11], $0.96(Bi_{0.5}Na_{0.5})(Ti_{1-x}Mn_x)O_3$–$0.04BiAlO_3$ ($x$ = 0–0.01 mol%) [48] and $(1-x)(Bi_{1/2}Na_{1/2})TiO_3$-$x(Bi_{1/2}Li_{1/2})TiO_3$ ($x$ = 0–0.24) [54]. In contrast to the change in $T_{F-R}$, it was found that $T_m$ increased from 306°C (BNBT) to 326°C (Li3) for Li doping but decreased to 288°C (Fe3) for Fe doping. Due to the complication behind the origin of $T_m$, the reason for its shifting is still inconclusive. Both upward [48] [55] [56] and downward [57] shift of $T_m$ have been reported in previous studies of acceptor doped BNT-based ceramics. However, regardless of the type of acceptor dopant used, a sharp rise in $\tan\delta$ at fairly high temperature (>400°C) was noticed in both Li- and Fe-doped BNBT ceramics with high doping content (e.g. Li2, Fe2, Li3, Fe3). This could be attributed to oxygen vacancies that can be thermally activated at high temperature [38], thus leading to an increase in $\tan\delta$ at elevated temperature, as was also shown previously in other acceptor-doped BNT–based ceramics e.g. Mn-doped 0.94BNT–0.04BA [48], Mn-doped BNBK [56] and Fe-doped BNBT [38].

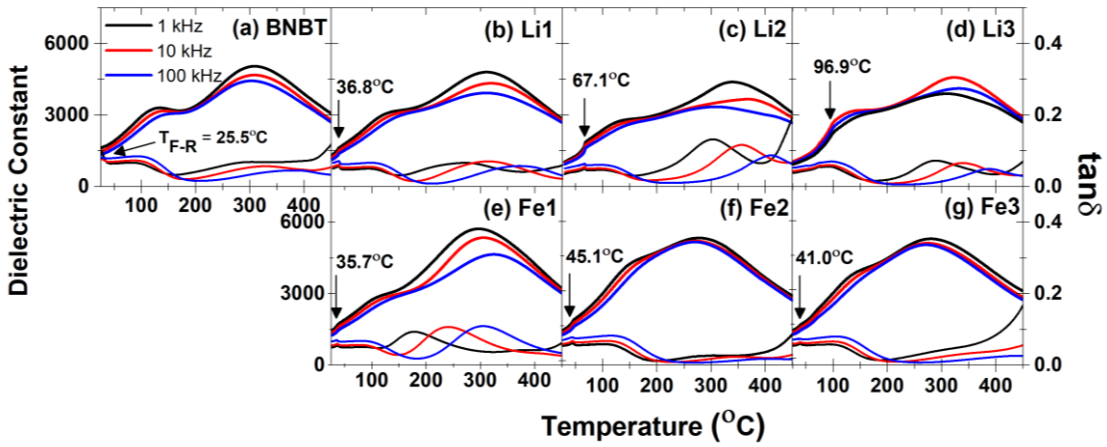


**Fig. 5.5.** Temperature dependence of relative permittivity ($\varepsilon_r$) and dielectric loss (tan $\delta$) for poled BNBT-*x*Li and BNBT-*x*Fe ceramics, *x* = 0.01, 0.02 and 0.03 measured at 1, 10 and 100 kHz.

**Table 5.2** Related dielectric properties parameters of unpoled and poled BNBT–*x*Li and BNBT–BNBT– *x*Fe ceramics

| Compositions | $T_{F-R}$ (°C) | $T_m$ (°C) | $\varepsilon_{r, RT}$ | $\tan\delta_{RT}$ | $\varepsilon_{r, m}$ | $\tan\delta_m$ |
|---|---|---|---|---|---|---|
| BNBT | 26 | 306 | 1666 | 0.09 | 5045 | 0.06 |
| Li1 | 37 | 311 | 1391 | 0.05 | 4780 | 0.06 |
| Li2 | 67 | 337 | 1032 | 0.03 | 4380 | 0.09 |
| Li3 | 97 | 326 | 1087 | 0.04 | 4574 | 0.06 |
| Fe1 | 36 | 291 | 1529 | 0.05 | 5714 | 0.04 |
| Fe2 | 45 | 287 | 1364 | 0.05 | 5265 | 0.02 |
| Fe3 | 41 | 288 | 1282 | 0.05 | 5204 | 0.04 |

### 5.5 Electrical conductivity and conduction mechanism

To investigate the conduction mechanism and further explain the observed sharp rise in tan$\delta$ at high temperature observed in previous section, impedance spectroscopy technique was conducted on all samples. Figure 5.6(a)–(g) shows the complex plane ($Z^*$) plots of BNBT-*x*Li and BNBT-*x*Fe ceramics measured in the temperature range of 460–540$^{\circ}$C at 20 Hz–10 MHz. For BNBT, the $Z^*$ plot showed a single semicircle corresponding to the bulk response. With increasing either Li or Fe doping content, a depressed single semicircle with an asymmetric arc at low frequency was clearly observed, indicating an increase in contribution from grain boundary. More details on the effects of Li and Fe will be discussed in the following paragraph. Nonetheless, in all samples, it can be seen clearly that the resistance values progressively decreased with the rise in temperature, conforming to the negative temperature coefficient of resistance (NTCR) effect commonly observed in various semiconductors [58] e.g. BNT-BT-*x*NN [59] and BNT-BT-*x*Cz [60]. This behavior can be attributed to the thermal activation of weakly trapped charge carriers [61]. The impedance data were also replotted in the form of $Z''(f)$ spectroscopic plots as demonstrated in Fig. 5.7(a)–(g). All samples exhibited a shift of $Z''$ peak toward higher frequencies along with a reduction of $Z''$ values with increasing temperature. This indicates a reduction of samples' resistance with an increase in temperature, consistent well with the behavior observed in $Z^*$ plots.

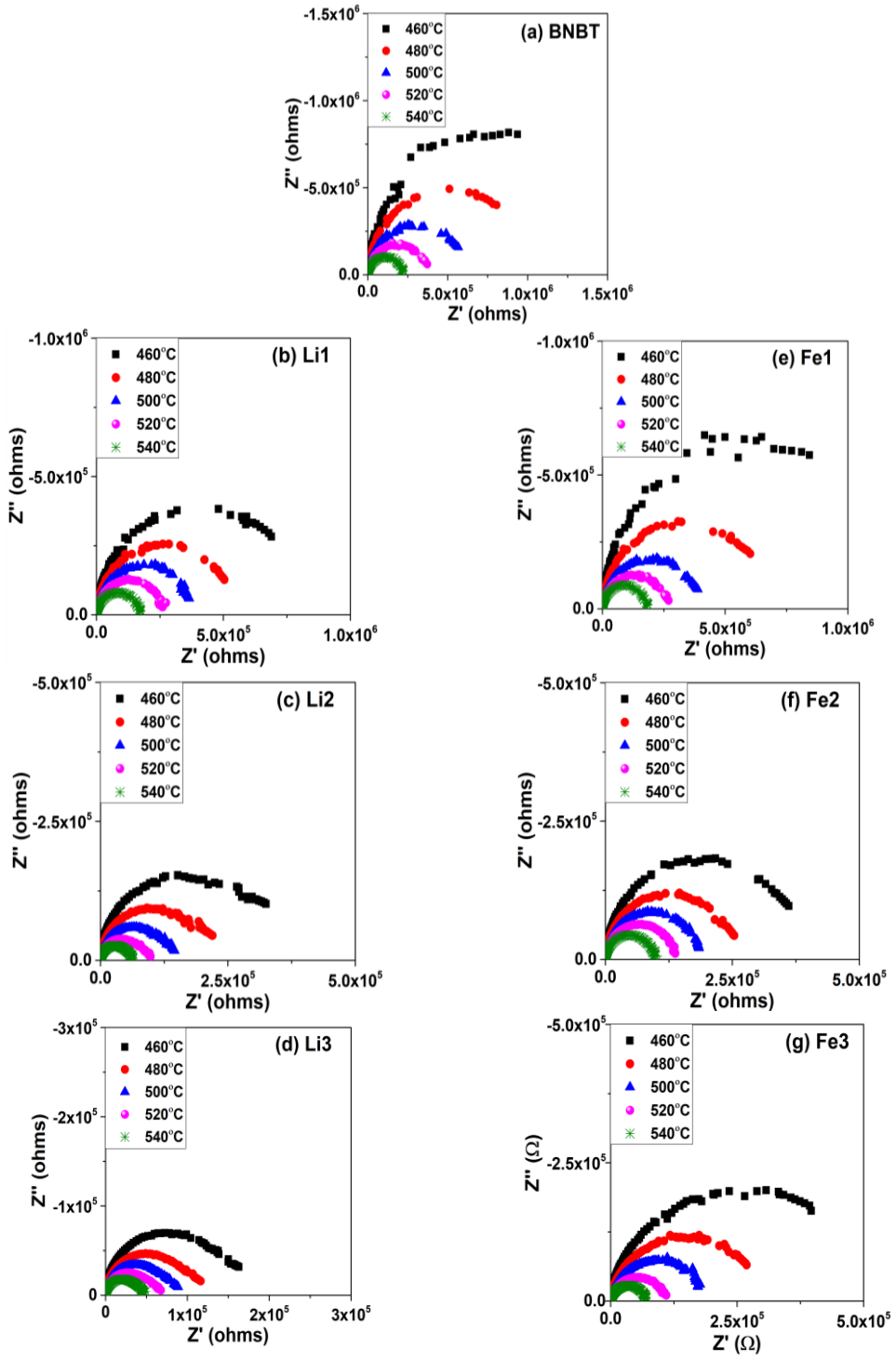


**Fig. 5.6.** Impedance complex plane plots (Z*) of BNBT–*x*Li and BNBT–*x*Fe ceramics, *x* = 0.01, 0.02 and 0.03, ceramics measured in the temperature range of 460°C-540°C.

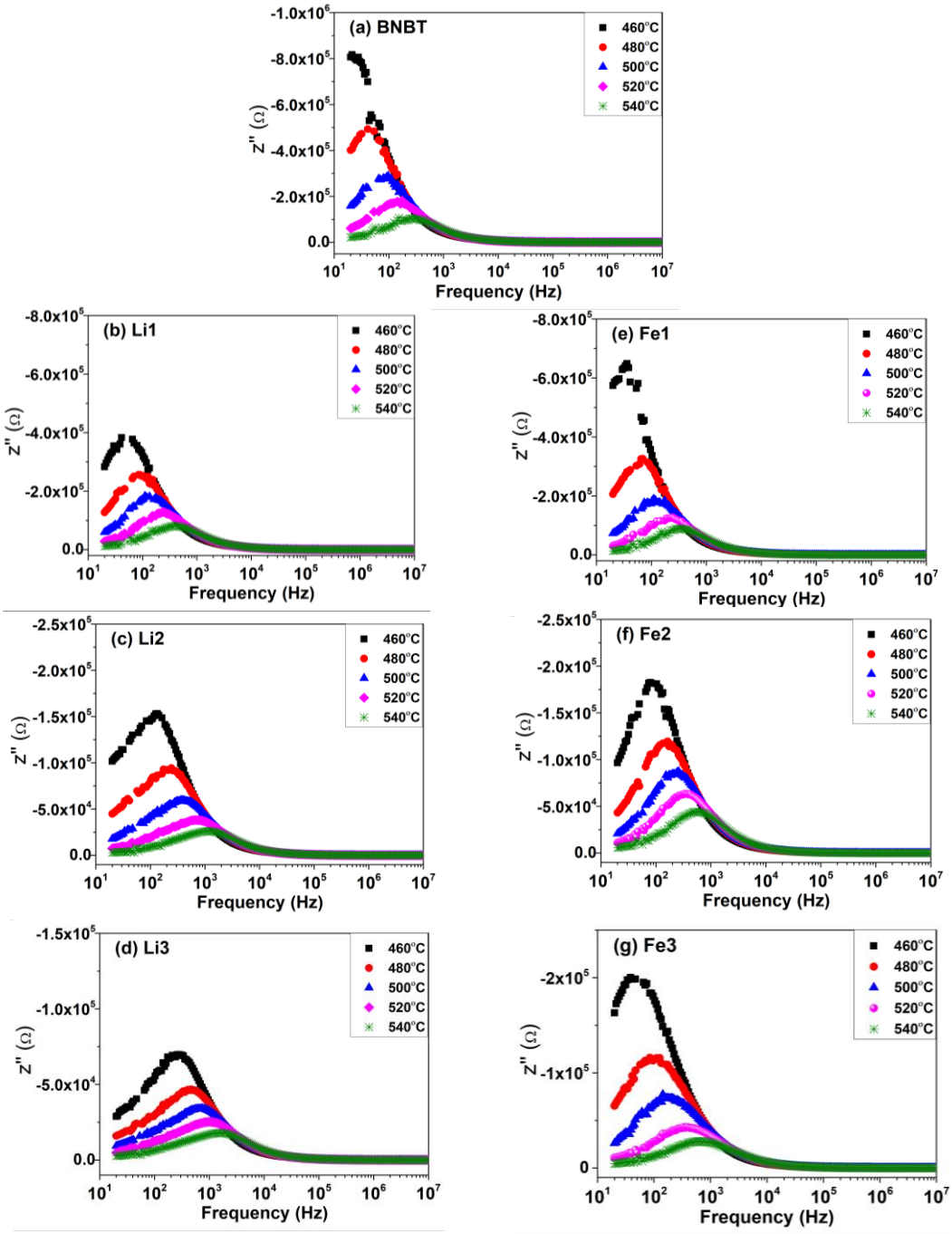


**Fig. 5.7.** The $Z''$(f) spectroscopic plots of BNBT–*x*Li and BNBT–*x*Fe ceramics, *x* = 0.01, 0.02 and 0.03, ceramics measured at different temperatures and frequencies (*T*=460°C–540°C, *f* = 20 Hz–10 MHz).

For a better comparison on the effect of Li and Fe doping, the complex plane (Z*) and corresponding normalized $Z''$(f) spectroscopic plots ($Z''/Z''_{max}$) at 540$^{\circ}$C of BNBT–*x*Li and BNBT–*x*Fe ceramics were compared as shown in Fig. 5.8(a)–(d). In addition, the resistivities ($\rho$), calculated from low frequency arc intersection on *x*-axis ($Z'$) and sample's dimension, are also listed in Table III. From Fig. 5.8 (a), (b) and Table III, it is clearly observed that increasing either Li or Fe doping content resulted in a continuous decrease of resistivity from 3.21 (BNBT) to 2.18, 0.98 and 0.72 MΩ.cm (for Li1, Li2 and Li3) and to 2.56, 1.56 and 1.02 MΩ.cm (for Fe1, Fe2 and Fe3), respectively. Moreover, it was found that the semicircular arc at low frequency became more apparent at high doping level for both Li- and Fe-doped BNBT compositions e.g. Li3, Fe3. This observation was evidently supported by the normalized $Z''$(f) plots (Fig. 5.8(c)–(d)) where a single Debye peak for BNBT clearly evolved into a broad peak with noticeable asymmetry at low frequency region with increasing Li or Fe doping content. The broadness of Debye peak was further confirmed by extracting the full width at half maximum (FWHM) (marked by arrow in Fig 8(c) and (d)). For BNBT, the FWHM of 1.20 decades was obtained, which is close to the ideal theoretical values of 1.14 decades [62]. With increasing doping level (*x*), the FWHM increased to 1.22, 1.41 and 1.58 decades for Li1 Li2 and Li3, respectively; meanwhile, it also increased to 1.16, 1.27 and 1.48 for Fe1, Fe2 and Fe3. The observed behaviors in both Z* and normalized $Z''(f)$ plots evidently suggest that the grain boundary contribution became more prominent upon increasing either Li or Fe doping content. Similar result was also reported in KNN modified 0.94BNT-0.06BT ceramics [60].

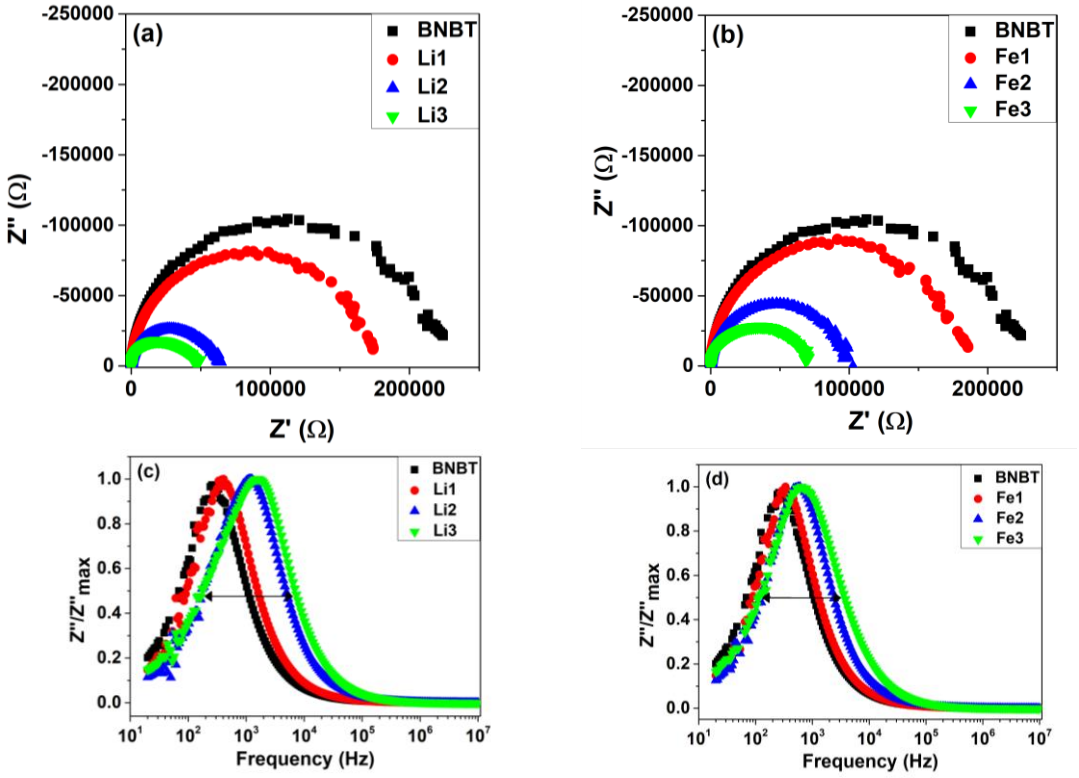


**Fig. 5.8.** The complex plane (Z*) plots at 540°C of (a) BNBT–*x*Li and (b) BNBT–*x*Fe ceramics along with the corresponding normalized $Z''$(f) spectroscopic plots at 540°C of (c) BNBT–*x*Li and (d) BNBT–*x*Fe ceramics.

To analyze the activation energy of conduction ($E_a$), the plots of 1000/T versus ln$\sigma$ for BNBT-*x*Li and BNBT–*x*Fe ceramics are demonstrated in Fig. 5.9(a) and (b), respectively. All plots obeyed the Arrhenius law, which is expressed as:

$$\sigma = \sigma_0 . exp\left[-\frac{E_a}{k_B T}\right] \quad (3)$$

where $\sigma_0$ is constant, $E_a$ is the activation energy of conduction, $k_B$ is Boltzmann constant and $T$ is temperature in Kelvin. By calculating the slope of the fitted graphs, the $E_a$ magnitudes for each composition were obtained as listed in Table 5.3. For $ABO_3$ perovskite materials, $E_a$ magnitudes varies depending on the type of conducting species. For example, doubly ionized oxygen vacancies ($V_O^{\cdot\cdot}$) can be thermally activated at high temperature with associated $E_a$ of

1.005–1.093 eV [63] [64] [65] while $E_a$ for intrinsic band-type electronic conduction for BNT-BT based materials were reported to be approximately half of the band gap ($E_g/2$ ~1.6–1.7 eV) [66] [67]. In the present study, the pure BNBT ceramic possessed $E_a$ of 1.33 eV, agreeing well with that of previous studies on BNT-based systems which reported $E_a$ in the range of 1.3–1.7 eV [68] [69]. With increasing doping level, despite some fluctuation, $E_a$ exhibited a decreasing trend to 0.86 eV (Li3) and 1.29 eV (Fe3). Though $E_a$ in the samples with high level of *x* content (e.g. Li2, Fe3) fell in the range of oxygen ionic conduction, the electrode response at low frequency was not observed. Therefore, the oxygen ionic conduction is not likely the case and we instead propose the electronic conduction to be the dominating mechanism for both undoped (i.e. BNBT) and doped (i.e. Li and Fe) BNBT samples, which is consistent with the studies of BNT-BT-CZ [70] and BNT-BT-KNN [60] and BNT-BT-NN [71]. In this study, the addition of Li or Fe most likely causes a reduction of energy barrier required for electronic conduction [60]. Consequently, the resistivity decreased with increasing doping level.

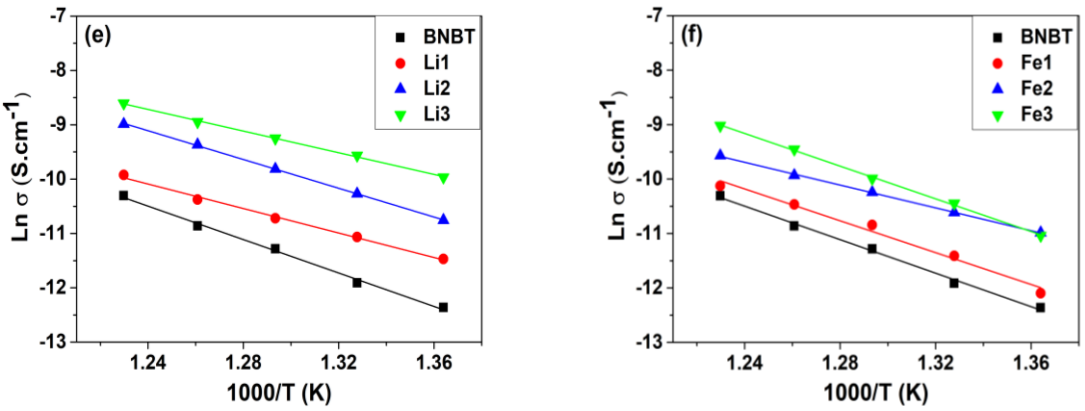


**Fig. 5.9.** The Arrhenius plots of (a) BNBT–*x*Li and (b) BNBT–*x*Fe ceramics. The symbols represent the experimental data and the straight line is the least-square fit.

**Table 5.3** The resistivity at 540°C and activation energy of conduction of BNBT–*x*Li and BNBT–*x*Fe ceramics

| Compositions | $\rho_{540°C}$ (Ω.cm) | $E_a$ (eV) |
|---|---|---|
| BNBT | $3.21 \times 10^6$ | 1.33 |
| Li1 | $2.18 \times 10^6$ | 0.97 |
| Li2 | $0.98 \times 10^6$ | 1.14 |
| Li3 | $0.72 \times 10^6$ | 0.86 |
| Fe1 | $2.56 \times 10^6$ | 1.26 |
| Fe2 | $1.56 \times 10^6$ | 0.90 |
| Fe3 | $1.02 \times 10^6$ | 1.29 |

### 5.6 Ferroelectric and piezoelectric properties

Figure 5.10(a)–(g) and Fig. 5.11(a)–(g) exhibits room temperature polarization hysteresis (*P*-*E*) loops and bipolar strain curves (*S*-*E*) of BNBT-*x*Li and BNBT-*x*Fe ceramics (*x*=0, 0.01, 0.02 and 0.03) under an applied electric field of 50 kV/cm at 1 Hz. Related ferroelectric and piezoelectric parameters including $E_c$, $P_r$, $P_s$, $P_r/P_s$ ratio, negative strain ($S_{neg}$) and positive strain ($S_{pos}$) are listed in Table IV. For pure BNBT, a relaxor-like slim *P*-*E* loop with relatively small $P_r$ (11.5 μC/cm$^2$) and $E_c$ (11.3 kV/cm) together with a sprout shaped *S*-*E* curve with no noticeable $S_{neg}$ (Fig. 5.11(a)) were observed, indicating that the obtained BNBT is in ergodic relaxor state having a “weak” polar phase at zero electric field which can reversibly transform into ferroelectric state under an applied field [72] [73] [74]. However, it’s observed that the $P_r$ and $E_c$ of BNBT in this study were lower than the reported values in previous studies of the same composition [75] [20], which may be attributed to the differences in the purity of the starting materials and/or the preparing conditions especially those that affect Bi and Na volatility [17] [20]. Interestingly, it was found that A-site (Li) and B-site (Fe) doped BNBT ceramics clearly exhibited different ferroelectric and piezoelectric properties upon increasing doping level (*x*).

For Li doping, at $x$ = 0.01 (Li1), both slim *P-E* loop and sprout-shaped *S-E* curve with similar $E_c$, $P_r$, $P_s$ and $S_{neg}$ values to that of BNBT were observed, suggesting that Li1 is still an ER. With increasing $x$ to 0.02 (Li2), an abrupt change to a square-like *P-E* loop with a substantial increase in $E_c$ (from 10.4 to 30.7 kV/cm) and $P_r$ (from 11.8 to 33.9 $\mu C/cm^2$), which is a common characteristic for ferroelectric, was observed and sustained up to $x$ = 0.03 (Li3). Corresponding well to the *P-E* loops, the *S-E* curves exhibited a sudden change from a sprout to a butterfly shape with obvious $S_{neg}$ at $x$ = 0.02 (Li2), which persisted up to $x$ = 0.03 (Li3). These drastic changes from a slim- to a rectangular-shaped *P-E* loop along with a transition from a sprout- to a butterfly-shaped *S-E* curves indicate that 2 mol% Li doping can induced the BNBT from ergodic relaxor (ER) to ferroelectric (or more precisely a nonergodic relaxor (NER) state). The results agreed well with the $T_{F-R}$ values, which were around RT for BNBT (26$^{O}$C) and Li1 (37$^{O}$C) but were significantly higher than RT for Li2 (67$^{O}$C) and Li3 (97$^{O}$C).

On the contrary, a slight constricted *P-E* loops with the $E_c$ that slightly varied in the range of 13.5–15.1 kV/cm was observed in all Fe-doped BNBT samples as seen from Fig. 5.10(e)-(g). Furthermore, both *P-E* and *S-E* data demonstrated that 1 mol% Fe (Fe1) can induce the ferroelectric order as evidently seen from a substantial increase in $P_r$ (from 11.5 to 28.6 $\mu C/cm^2$), a moderate increase in $P_s$ (from 34.5 to 38.5 $\mu C/cm^2$) and the emergence of butterfly-shaped bipolar strain with obvious $S_{neg}$ (0.16%). With increasing of $x$ to 0.02 (Fe2) and 0.03 (Fe3), a gradual increase in $P_r$ (to 29.4 and 31.7 $\mu C/cm^2$), $P_s$ (to 39 and 39.7 $\mu C/cm^2$) and $S_{neg}$ (to 0.17% and 0.19%) were clearly detected, thus suggesting a continuous increase in ferroelectricity upon increasing Fe doping content. These observations were further supported by the $P_r/P_s$ ratio which showed a large jump from 33.3% (BNBT) to 74.3 (Fe1) and then kept increasing to 75.4% (Fe2) and 79.8% (Fe3), indicating that a fraction of electric field-induced polarization, which remains after removing electric field, is larger in the sample with higher Fe content. In addition, alongside with the slight constricted P-E loop, it's worth noting that all Fe1, Fe2 and Fe3 samples possessed the deformed butterfly-shaped *S-E* curves, which can be observed as a broad feature around the negative strain minimum. Similar phenomena

(i.e. slight constricted *P-E* loops and deformed butterfly-shape *S-E* curves) have also been encountered in other modified BNT-based materials when the measuring temperatures is close to the ferroelectric-to-relaxor transition temperature ($T_{F-R}$). In other words, it is often observed at the temperature slightly below $T_{F-R}$ or when the disrupted ferroelectric order is almost completely changed to the ergodic relaxor state (ER). Examples of those systems include $85BN_{0.5(1-x)}Li_{0.5x}$T-11BKT-4BT ($x$ = 0–0.15) [76] in which a gradual disruption of ferroelectric order was observed with increasing $x$. In their study, a slim *P-E* loop together with sprout-shaped *S-E* curve were observed in the sample ($x$ = 0.15), which had $T_{F-R}$ lower than RT, while the exact same *P-E*/*S-E* behaviors to this study were detected at the measuring temperature of $40^{O}$ in $x$ = 0.10 composition, which possessed the $T_{F-R}$ of $70^{O}$C. Similarly, for (1-$x$)BNKT-$x$$SrTi_{0.8}Zr_{0.2}O_3$ ($x$ = 0–1.0%) ceramics [77], the same phenomena as this study (i.e. a concurrent constricted *P-E* loop with high $P_r$ and the deformed butterfly *S-E* curve) were also observed at 10-$20^{O}$C lower than the $T_{F-R}$ e.g. at $60^{O}$C ($T_{F-R}$ = $71^{O}$C), for $x$ = 0 and at $90^{O}$C ($T_{F-R}$ = $109^{O}$C), for $x$ = 0.2%. Thus, based on these studies, we proposed the $T_{F-R}$, which located slightly above the RT in all Fe1 ($36^{O}$C) Fe2 ($45^{O}$C) and Fe3 ($41^{O}$C) samples, to be responsible for the observed constricted *P-E* loops in Fe-doped BNBT ceramics.

For the compositions around the MPB where two phases coexist, the *P-E* loop characteristics (e.g. $E_c$, $P_r$) are also greatly influenced by the phase fraction or the dominating phase [78] [79] [40]. For example, the higher the *P4bm* phase is, the smaller the $E_c$ and $P_r$ is observed for BNBT-based ceramics having *R3c* and *P4bm* coexistent phases [40] [78] while the opposite trend (i.e. a higher $E_c$ and $P_r$) was detected for PZT-based systems [80]. In this study, the data from XRD and Rietveld refinement clearly showed that both BNBT-$x$Li and BNBT-$x$Fe ceramics possessed similar amount of *R3c* ($\sim 79\% - 85\%$) and *P4bm* ($\sim 15 - 21\%$) phase upon increasing doping content, which was even further confirmed by XANEs analysis for the case of BNBT-$x$Fe ceramics to be consistent (80% *R3c* 20% *P4bm*). Besides, the microstructure (i.e. grain size), which can also affect the *P-E* loop features [78], was also revealed by the SEM to display the same trend upon increasing either Li or Fe doping level.

Accordingly, the attributing of inconsistencies of high-field ferroelectric and piezoelectric properties between BNBT-*x*Li and BNBT-*x*Fe ceramics to the $T_{F-R}$ seems to be reasonable as other influencing factors (e.g. crystal structure and microstructure) were verified to be mostly the same change upon increasing either Li or Fe doping content.

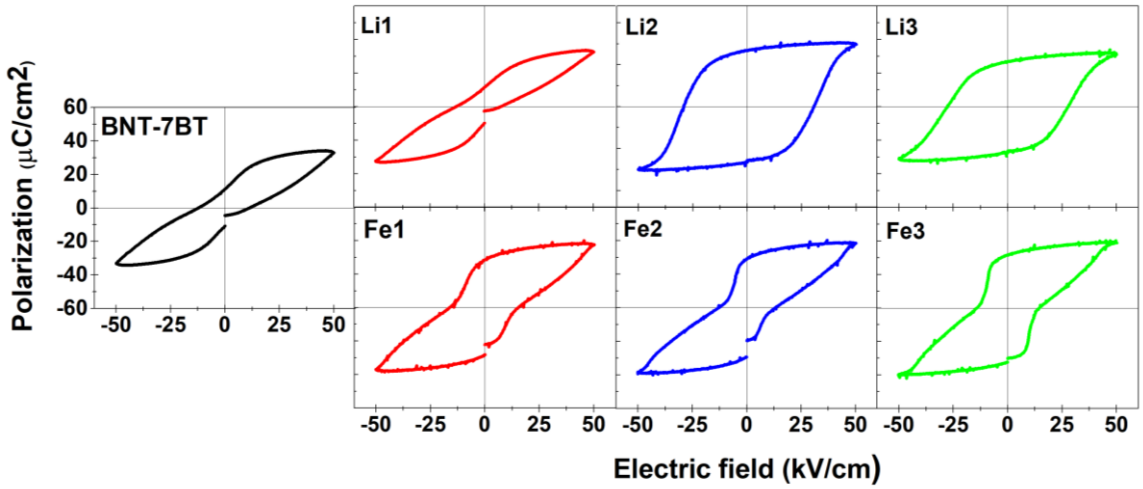


**Fig. 5.10.** Room temperature polarization hysteresis (*P*-*E*) loops of BNBT-*x*Li and BNBT-*x*Fe ceramics (x = 0, 0.01, 0.02 and 0.03) measured at 1 Hz.

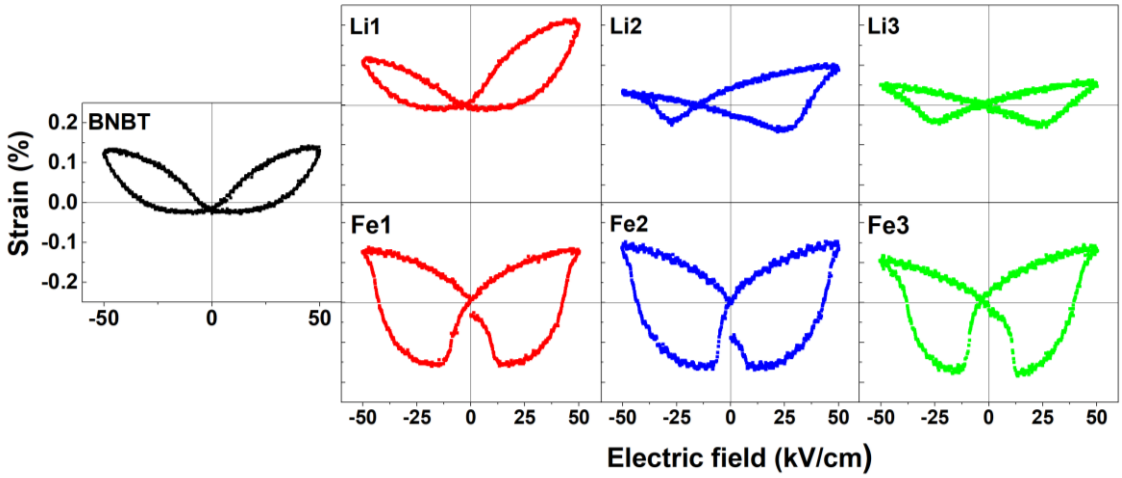


**Fig. 5.11.** Room temperature bipolar strain curves of BNBT-*x*Li and BNBT-*x*Fe ceramics (*x* = 0, 0.01, 0.02 and 0.03) measured at 1 Hz.

**Table 5.4** Room temperature ferroelectric and strain properties of BNBT-*x*Li and BNBT-*x*Fe ceramics ($x$ = 0, 0.01, 0.02 and 0.03)

| Compositions | $E_c$ (kV/cm) | $P_r$ ($\mu C/cm^2$) | $P_s$ ($\mu C/cm^2$) | $P_r/P_s$ (%) | $S_{neg}$ (%) (+$E$ direction) | $S_{pos}$ (%) (+$E$ direction) |
|---|---|---|---|---|---|---|
| BNBT | 11.3 | 11.5 | 34.5 | 33.3 | - | 0.16 |
| Li1 | 10.4 | 11.8 | 33.4 | 35.3 | - | 0.22 |
| Li2 | 30.7 | 33.9 | 38.3 | 88.5 | 0.073 | 0.11 |
| Li3 | 27.7 | 26.7 | 32.2 | 82.9 | 0.065 | 0.066 |
| Fe1 | 15.1 | 28.6 | 38.5 | 74.3 | 0.16 | 0.14 |
| Fe2 | 13.5 | 29.4 | 39.0 | 75.4 | 0.17 | 0.16 |
| Fe3 | 14.5 | 31.7 | 39.7 | 79.8 | 0.19 | 0.15 |

## 6. conclusion

Dense BNBT-*x*Li and BNBT-*x*Fe ($x$ = 0.01-0.03) ceramics were obtained via conventional solid-state reaction mixed-oxide route. XRD refinement revealed a coexistence of rhombohedral (*R3c*) and tetragonal (*P4bm*) phases with almost unchanged *R3c*/*P4bm* phase ratio (∼80/20) across the entire A-site Li and B-site Fe doping level studied. The results were further confirmed by XANEs analysis. With increasing Li or Fe doping content, the average grain size tended to increase while the resistivity ($\rho$) and activation energy of conduction ($E_a$) exhibited a decreasing trend, indicating that the samples became more conductive. However, different ferroelectric and piezoelectric properties were observed between A-site Li and B-site Fe doping. For A-site Li doping, 2 mol% doping level can transform the materials from an ergodic relaxor (ER) to ferroelectric as seen from a square-type *P-E* loops with substantial increase in $E_c$ (30.7 kV/cm), $P_r$ (33.9 $\mu C/cm^2$) and the presence of $S_{neg}$ (0.11%) in *S-E* curves. Meanwhile, for B-site Fe doping, slight constricted *P-E* with a moderate increase in $E_c$ (∼13–15 kV/cm) and a significant increase in $P_r$ (28–31 $\mu C/cm^2$) was observed throughout the whole doping level studied. The discrepancies could be linked to the ferroelectric-to-relaxor transition temperature ($T_{F-R}$) which exhibited a pronounced increase for Li doping but only showed moderate rise for Fe doping (97$^{O}$C, for Li3, and 41$^{O}$C. for Fe3). Thus, this study highlights the

differences in the *P-E* loop and *S-E* curves of Li and Fe doping, which will be beneficial for tailoring the BNT-based materials' properties for different applications.

## 7. References


[1] B. Jaffe, Piezoelectric ceramics, Elsevier, 2012.

[2] A.J. Moulson, J.M. Herbert, Electroceramics: materials, properties, applications, John Wiley & Sons, 2003.

[3] T.R. Shrout, R. Eitel, S. Zhang, C. Randall, E. Alberta, P. Rehrig, Recent developments in transition temperature ($T_c$) perovskite crystals, in: IEEE, 2003: pp. 774–777.

[4] S. Zhang, J.B. Lim, H.J. Lee, T.R. Shrout, Characterization of hard piezoelectric lead-free ceramics, IEEE Transactions on Ultrasonics, Ferroelectrics, and Frequency Control. 56 (2009).

[5] P. Lambeck, G. Jonker, The nature of domain stabilization in ferroelectric perovskites, Journal of Physics and Chemistry of Solids. 47 (1986) 453–461.

[6] L. Zhang, X. Ren, In situ observation of reversible domain switching in aged Mn-doped $BaTiO_3$ single crystals, Physical Review B. 71 (2005) 174108.

[7] R. Directive, Directive 2002/95/EC of the European Parliament and of the Council of 27 January 2003 on the restriction of the use of certain hazardous substances in electrical and electronic equipment, Official Journal of the European Union. 13 (2003) L37.

[8] T. Takenaka, K. Maruyama, K. Sakata, $(Bi_{1/2}Na_{1/2})TiO_3$-$BaTiO_3$ system for lead-free piezoelectric ceramics, Japanese Journal of Applied Physics. 30 (1991) 2236.

[9] C. Ma, X. Tan, Phase diagram of unpoled lead-free–ceramics, Solid State Communications. 150 (2010) 1497–1500.

[10] E. Aksel, E. Erdem, P. Jakes, J.L. Jones, R.-A. Eichel, Defect structure and materials "hardening" in $Fe_2O_3$-doped $[Bi_{0.5}Na_{0.5}]TiO_3$ ferroelectrics, Applied Physics Letters. 97 (2010) 012903.

[11] H. Zhang, J. Zhou, W. Chen, X. Yang, J. Shen, C. Wu, Stabilization of Ferroelectric Order in $Bi_{1/2}(Na_{0.8}K_{0.2})_{1/2}TiO_3$ Lead-Free Ceramics with Fe Doping, Journal of Electronic Materials. 46 (2017) 6167–6174.

[12] E. Sapper, R. Dittmer, D. Damjanovic, E. Erdem, D.J. Keeble, W. Jo, T. Granzow, J. Rödel, Aging in the relaxor and ferroelectric state of Fe-doped (1-x)($Bi_{1/2}Na_{1/2}$)$TiO_3$-x$BaTiO_3$ piezoelectric ceramics, Journal of Applied Physics. 116 (2014) 104102.

[13] W. Jo, E. Erdem, R.-A. Eichel, J. Glaum, T. Granzow, D. Damjanovic, J. Rödel, Effect of Nb-donor and Fe-acceptor dopants in ($Bi_{1/2}Na_{1/2}$)$TiO_3$–$BaTiO_3$–($K_{0.5}Na_{0.5}$)$NbO_3$ lead-free piezoceramics, Journal of Applied Physics. 108 (2010) 014110.

[14] M. Zhu, L. Liu, Y. Hou, H. Wang, H. Yan, Microstructure and electrical properties of MnO-doped ($Na_{0.5}Bi_{0.5}$)$_{0.92}Ba_{0.08}TiO_3$ lead-free piezoceramics, Journal of the American Ceramic Society. 90 (2007) 120–124.

[15] Y. Hiruma, H. Nagata, T. Takenaka, Thermal depoling process and piezoelectric properties of bismuth sodium titanate ceramics, Journal of Applied Physics. 105 (2009) 084112.

[16] M. Li, M.J. Pietrowski, R.A. De Souza, H. Zhang, I.M. Reaney, S.N. Cook, J.A. Kilner, D.C. Sinclair, A family of oxide ion conductors based on the ferroelectric perovskite $Na_{0.5}Bi_{0.5}TiO_3$, Nature Materials. 13 (2014) 31–35.

[17] X. Liu, Y. Zhao, J. Shi, H. Du, X. Xu, H. Lu, J. Che, X. Li, Improvement of dielectric and ferroelectric properties in bismuth sodium titanate based relaxors through Bi non-stoichiometry, Journal of Alloys and Compounds. 799 (2019) 231–238.

[18] Y. Sung, J. Kim, J. Cho, T. Song, M. Kim, T. Park, Effects of Bi nonstoichiometry in ($Bi_{0.5+x}Na$)$TiO_3$ ceramics, Applied Physics Letters. 98 (2011) 012902.

[19] D.P. Shih, A. Aguadero, S.J. Skinner, Improvement of ionic conductivity in A-site lithium doped sodium bismuth titanate, Solid State Ionics. 317 (2018) 32–38.

[20] S. Prasertpalichat, D.P. Cann, Hardening in non-stoichiometric (1− x)$Bi_{0.5}Na_{0.5}TiO_3$–x$BaTiO_3$ lead-free piezoelectric ceramics, Journal of Materials Science. 51 (2016) 476–486.

[21] G. Yesner, A. Safari, Improved resistivity in bismuth deficient morphotropic phase boundary 0.88BNT-0.08BKT-0.04BT ceramics, in: IEEE, 2017: pp. 110–112.

[22] M. Takahashi, Space charge effect in lead zirconate titanate ceramics caused by the addition of impurities, Japanese Journal of Applied Physics. 9 (1970) 1236.

[23] D.C. Lupascu, Y.A. Genenko, N. Balke, Aging in ferroelectrics, Journal of the American Ceramic Society. 89 (2006) 224–229.

[24] W. Warren, D. Dimos, B. Tuttle, R. Nasby, G. Pike, Electronic domain pinning in Pb (Zr, Ti) O3 thin films and its role in fatigue, Applied Physics Letters. 65 (1994) 1018–1020.

[25] W.L. Warren, D. Dimos, B.A. Tuttle, D.M. Smyth, Electronic and ionic trapping at domain walls in $BaTiO_3$, Journal of the American Ceramic Society. 77 (1994) 2753–2757.

[26] Y.A. Genenko, J. Glaum, M.J. Hoffmann, K. Albe, Mechanisms of aging and fatigue in ferroelectrics, Materials Science and Engineering: B. 192 (2015) 52–82.

[27] X. Ren, Large electric-field-induced strain in ferroelectric crystals by point-defect-mediated reversible domain switching, Nature Materials. 3 (2004) 91.

[28] D. Damjanovic, Hysteresis in piezoelectric and ferroelectric materials, The Science of Hysteresis. 3 (2006) 337–465.

[29] R. Zuo, S. Su, Y. Wu, J. Fu, M. Wang, L. Li, Influence of A-site nonstoichiometry on sintering, microstructure and electrical properties of $(Bi_{0.5}Na_{0.5})TiO_3$ ceramics, Materials Chemistry and Physics. 110 (2008) 311–315.

[30] Y. Sung, J. Kim, J. Cho, T. Song, M. Kim, H. Chong, T. Park, D. Do, S. Kim, Effects of Na nonstoichiometry in $(Bi_{0.5}Na_{0.5+x})TiO_3$ ceramics, Applied Physics Letters. 96 (2010) 022901.

[31] M. Li, H. Zhang, S.N. Cook, L. Li, J.A. Kilner, I.M. Reaney, D.C. Sinclair, Dramatic influence of A-site nonstoichiometry on the electrical conductivity and conduction mechanisms in the perovskite oxide $Na_{0.5}Bi_{0.5}TiO_3$, Chemistry of Materials. 27 (2015) 629–634.

[32] B. Ravel, M. Newville, ATHENA, ARTEMIS, HEPHAESTUS: data analysis for X-ray absorption spectroscopy using IFEFFIT, Journal of Synchrotron Radiation. 12 (2005) 537–541.

[33] H. Simons, J. Daniels, W. Jo, R. Dittmer, A. Studer, M. Avdeev, J. Rödel, M. Hoffman, Electric-field-induced strain mechanisms in lead-free $94\%(Bi_{1/2}Na_{1/2})TiO_3$–$6\%BaTiO_3$, Applied Physics Letters. 98 (2011) 082901.

[34] J.E. Daniels, W. Jo, J. Rödel, J.L. Jones, Electric-field-induced phase transformation at a lead-free morphotropic phase boundary: Case study in a $93\%(Bi_{0.5}Na_{0.5})TiO_3$–$7\%$ $BaTiO_3$ piezoelectric ceramic, Applied Physics Letters. 95 (2009) 032904.

[35] S.-T. Zhang, A.B. Kounga, E. Aulbach, H. Ehrenberg, J. Rödel, Giant strain in lead-free piezoceramics $Bi_{0.5}Na_{0.5}TiO_3$–$BaTiO_3$–$K_{0.5}Na_{0.5}NbO_3$ system, Applied Physics Letters. 91 (2007) 112906.

[36] H. Hayashi, H. Inaba, M. Matsuyama, N. Lan, M. Dokiya, H. Tagawa, Structural consideration on the ionic conductivity of perovskite-type oxides, Solid State Ionics. 122 (1999) 1–15.

[37] R.D. Shannon, Revised effective ionic radii and systematic studies of interatomic distances in halides and chalcogenides, Acta Crystallographica Section A: Crystal Physics, Diffraction, Theoretical and General Crystallography. 32 (1976) 751–767.

[38] C. Wang, T. Xia, X. Lou, Effects of Fe2O3 doping on the electrical properties of $Na_{0.47}Bi_{0.47}Ba_{0.06}TiO_3$ lead-free ceramics, Ceramics International. 44 (2018) 22053–22058.

[39] G. Viola, R. McKinnon, V. Koval, A. Adomkevicius, S. Dunn, H. Yan, Lithium-induced phase transitions in lead-free $Bi_{0.5}Na_{0.5}TiO_3$ based ceramics, The Journal of Physical Chemistry C. 118 (2014) 8564–8570.

[40] Q. Xu, H. Liu, L. Zhang, J. Xie, H. Hao, M. Cao, Z. Yao, M.T. Lanagan, Structure and electrical properties of lead-free $Bi_{0.5}Na_{0.5}TiO_3$-based ceramics for energy-storage applications, RSC Advances. 6 (2016) 59280–59291.

[41] S. Prasertpalichat, T. Siritanon, N. Nuntawong, D.P. Cann, Structural characterization of A-site nonstoichiometric $(1-x)\ Bi_{0.5}Na_{0.5}TiO_3–xBaTiO_3$ ceramics, Journal of Materials Science. 54 (2019) 1162–1170.

[42] S. Limpijumnong, S. Rujirawat, A. Boonchun, M. Smith, B. Cherdhirunkorn, Identification of Mn site in Pb (Zr, Ti)$O_3$ by synchrotron x-ray absorption near-edge structure: Theory and experiment, Applied Physics Letters. 90 (2007) 103113.

[43] J. Jutimoosik, S. Hunpratub, S. Maensiri, S. Rujirawat, R. Yimnirun, On preferred Mn site in multiferroic $BiFeO_3$: A view by synchrotron x-ray absorption near edge structure spectroscopy, Journal of Applied Physics. 116 (2014) 104105.

[44] A. Ankudinov, B. Ravel, J. Rehr, S. Conradson, Real-space multiple-scattering calculation and interpretation of x-ray-absorption near-edge structure, Physical Review B. 58 (1998) 7565.

[45] E. Taghaddos, M. Hejazi, A. Safari, Electromechanical properties of acceptor‐doped lead‐free piezoelectric ceramics, Journal of the American Ceramic Society. 97 (2014) 1756–1762.

[46] T.H. Dinh, M.R. Bafandeh, J.-K. Kang, C.-H. Hong, W. Jo, J.-S. Lee, Comparison of structural, ferroelectric, and strain properties between A-site donor and acceptor doped Bi1/2 $(Na_{0.82}K_{0.18})_{1/2}TiO_3$ ceramics, Ceramics International. 41 (2015) S458–S463.

[47] S. Wongsaenmai, R. Yimnirun, P. Laoratanakul, Effects of Dopants on Phase Formation and Microstructure of Bismuth Sodium Titanate-Potassium Sodium Niobate Ceramics, Ferroelectrics. 458 (2014) 214–220.

[48] P. Peng, H. Nie, Z. Liu, W. Ren, F. Cao, G. Wang, X. Dong, Enhanced ferroelectric properties and thermal stability of Mn-doped 0.96 $(Bi_{0.5}Na_{0.5})TiO_3$-0.04$BiAlO_3$ ceramics, Journal of the American Ceramic Society. 100 (2017) 1030–1036.

[49] W. Jo, R. Dittmer, M. Acosta, J. Zang, C. Groh, E. Sapper, K. Wang, J. Rödel, Giant electric-field-induced strains in lead-free ceramics for actuator applications–status and perspective, Journal of Electroceramics. 29 (2012) 71–93.

[50] W. Jo, S. Schaab, E. Sapper, L.A. Schmitt, H.-J. Kleebe, A.J. Bell, J. Rödel, On the phase identity and its thermal evolution of lead free $(Bi_{1/2}Na_{1/2)}TiO_3$-6 mol%$BaTiO_3$, Journal of Applied Physics. 110 (2011) 074106.

[51] E. Sapper, S. Schaab, W. Jo, T. Granzow, J. Rödel, Influence of electric fields on the depolarization temperature of Mn-doped (1-x)$Bi_{1/2}Na_{1/2}TiO_3$-x$BaTiO_3$, Journal of Applied Physics. 111 (2012) 014105.

[52] J. Rödel, W. Jo, K.T. Seifert, E. Anton, T. Granzow, D. Damjanovic, Perspective on the Development of Lead-free Piezoceramics, Journal of the American Ceramic Society. 92 (2009) 1153–1177.

[53] G. Dong, H. Fan, J. Shi, M. Li, Composition-and Temperature-Dependent Large Strain in (1− x)(0.8$Bi_{0.5}Na_{0.5}TiO_3$–0.2Bi0.5$K_{0.5}TiO_3$)–x$NaNbO_3$ Ceramics, Journal of the American Ceramic Society. 98 (2015) 1150–1155.

[54] Y. Hiruma, K. Yoshii, H. Nagata, T. Takenaka, Phase transition temperature and electrical properties of $(Bi_1/_2Na_1/_2)TiO_3$–$(Bi_1/_2A_1/_2)TiO_3$ (A= Li and K) lead-free ferroelectric ceramics, Journal of Applied Physics. 103 (2008) 084121.

[55] J. Li, F. Wang, C.M. Leung, S.W. Or, Y. Tang, X. Chen, T. Wang, X. Qin, W. Shi, Large strain response in acceptor-and donor-doped $Bi_{0.5}Na_{0.5}TiO_3$-based lead-free ceramics, Journal of Materials Science. 46 (2011) 5702–5708.

[56] Y. Qin, S. Zhang, Y. Wu, C. Lu, J. Zhang, Impacts of acceptor doping on the piezoelectric properties and domain structure in NBT-based lead-free ceramics, Journal of the European Ceramic Society. 37 (2017) 3493–3500.

[57] C. Lee, H. Han, T.A. Duong, T.H. Dinh, C.W. Ahn, J. Lee, Stabilization of the relaxor phase by adding CuO in lead-free $(Bi_{1/2}Na_{1/2})TiO_3$—$SrTiO_3$—$BiFeO_3$ ceramics, Ceramics International. 43 (2017) 11071–11077.

[58] B.K. Barick, R.N.P. Choudhary, D.K. Pradhan, Dielectric and impedance spectroscopy of zirconium modified (Na0. 5Bi0. 5) TiO3 ceramics, Ceramics International. 39 (2013) 5695–5704.

[59] Q. Xu, M.T. Lanagan, X. Huang, J. Xie, L. Zhang, H. Hao, H. Liu, Dielectric behavior and impedance spectroscopy in lead-free BNT–BT–NBN perovskite ceramics for energy storage, Ceramics International. 42 (2016) 9728–9736.

[60] J. Zang, M. Li, D.C. Sinclair, W. Jo, J. Rödel, Impedance spectroscopy of $(Bi_{1/2}Na_{1/2})TiO_3$–$BaTiO_3$ ceramics modified with $(K_{0.5}Na_{0.5})NbO_3$, Journal of the American Ceramic Society. 97 (2014) 1523–1529.

[61] Y. Huang, D. Shi, L. Liu, G. Li, S. Zheng, L. Fang, High-temperature impedance spectroscopy of $BaFe_{0.5}Nb_{0.5}O_3$ ceramics doped with $Bi_{0.5}Na_{0.5}TiO_3$, Applied Physics A. 114 (2014) 891–896.

[62] D. Sinclair, A. West, Effect of atmosphere on the PTCR properties of $BaTiO_3$ ceramics, Journal of Materials Science. 29 (1994) 6061–6068.

[63] T. Baiatu, R. Waser, K. Härdtl, dc electrical degradation of Perovskite-type Titanates: III, a model of the mechanism, Journal of the American Ceramic Society. 73 (1990) 1663–1673.

[64] R. Waser, T. Baiatu, K. Härdtl, dc Electrical Degradation of Perovskite-Type Titanates: I, Ceramics, Journal of the American Ceramic Society. 73 (1990) 1645–1653.

[65] R. Waser, T. Baiatu, K. Härdtl, dc Electrical Degradation of Perovskite-Type Titanates: II, Single Crystals, Journal of the American Ceramic Society. 73 (1990) 1654–1662.

[66] M. Bousquet, J.-R. Duclère, E. Orhan, A. Boulle, C. Bachelet, C. Champeaux, Optical properties of an epitaxial $Na_{0.5}Bi_{0.5}TiO_3$ thin film grown by laser ablation: Experimental approach and density functional theory calculations, Journal of Applied Physics. 107 (2010) 104107.

[67] M. Cernea, A.C. Galca, M.C. Cioangher, C. Dragoi, G. Ioncea, Piezoelectric BNT-BT 0.11 thin films processed by sol–gel technique, Journal of Materials Science. 46 (2011) 5621–5627.

[68] Y.-M. Li, W. Chen, J. Zhou, Q. Xu, X.-Y. Gu, R.-H. Liao, Impedance spectroscopy and dielectric properties of $Na_{0.5}Bi_{0.5}TiO_3$–$NaNbO_3$ ceramics, Physica B: Condensed Matter. 365 (2005) 76–81.

[69] J. East, D. Sinclair, Characterization of $(Bi_{1/2}Na_{1/2})TiO_3$ using electric modulus spectroscopy, Journal of Materials Science Letters. 16 (1997) 422–425.

[70] J. Zang, M. Li, D.C. Sinclair, T. Frömling, W. Jo, J. Rödel, Impedance Spectroscopy of $(Bi_{1/2}Na_{1/2})TiO_3$–$BaTiO_3$ Based High-Temperature Dielectrics, Journal of the American Ceramic Society. 97 (2014) 2825–2831.

[71] Q. Xu, M.T. Lanagan, W. Luo, L. Zhang, J. Xie, H. Hao, M. Cao, Z. Yao, H. Liu, Electrical properties and relaxation behavior of $Bi_{0.5}Na_{0.5}TiO_3$-$BaTiO_3$ ceramics modified with $NaNbO_3$, Journal of the European Ceramic Society. 36 (2016) 2469–2477.

[72] A. Ullah, C. Won Ahn, A. Ullah, I. Won Kim, Large strain under a low electric field in lead-free bismuth-based piezoelectrics, Applied Physics Letters. 103 (2013) 022906.

[73] K. Wang, A. Hussain, W. Jo, J. Rödel, Temperature-Dependent Properties of $(Bi_{1/2}Na_{1/2})TiO_3$–$(Bi_{1/2}K_{1/2})TiO_3$–$SrTiO_3$ Lead-Free Piezoceramics, Journal of the American Ceramic Society. 95 (2012) 2241–2247.

[74] W. Jo, T. Granzow, E. Aulbach, J. Rödel, D. Damjanovic, Origin of the large strain response in $(K_{0.5}Na_{0.5})NbO_3$-modified $(Bi_{0.5}Na_{0.5})TiO_3$–$BaTiO_3$ lead-free piezoceramics, Journal of Applied Physics. 105 (2009) 094102.

[75] H. Lidjici, B. Lagoun, M. Berrahal, M. Rguitti, M.A. Hentatti, H. Khemakhem, XRD, Raman and electrical studies on the $(1-x)(Na_{0.5}Bi_{0.5})TiO_3-xBaTiO_3$ lead free ceramics, Journal of Alloys and Compounds. 618 (2015) 643–648.

[76] D. Yin, Z. Zhao, Y. Dai, Z. Zhao, X. Zhang, S. Wang, Electrical properties and relaxor phase evolution of Li-modified BNT-BKT-BT lead-free ceramics, Journal of the American Ceramic Society. 99 (2016) 2354–2360.

[77] Y. Guo, H. Fan, J. Shi, Origin of the large strain response in tenary $SrTi_{0.8}Zr_{0.2}O_3$ modified $Bi_{0.5}Na_{0.5}TiO_3$–$Bi_{0.5}K_{0.5}TiO_3$ lead-free piezoceramics, Journal of Materials Science. 50 (2015) 403–411.

[78] L. Jin, F. Li, S. Zhang, Decoding the fingerprint of ferroelectric loops: comprehension of the material properties and structures, Journal of the American Ceramic Society. 97 (2014) 1–27.

[79] K. Yoshii, Y. Hiruma, H. Nagata, T. Takenaka, Electrical properties and depolarization temperature of $(Bi_{1/2}Na_{1/2})TiO_3$–$(Bi_{1/2}K_{1/2})TiO_3$ lead-free piezoelectric ceramics, Japanese Journal of Applied Physics. 45 (2006) 4493.

[80] L. Jin, Broadband dielectric response in hard and soft PZT: Understanding softening and hardening mechanisms, Ceramics Laboratory. (2011).

## 8. Suggestions for future research

Though the experimental results (XRD, XAS, SEM, electrical conductivity ferroelectric and piezoelectric) clearly demonstrated that A-site Li doping resulted in a more pronounced hardening characteristics in terms of an increase in $E_c$ as compared to that of B-site Fe doping where the constricted *P-E* loops with relatively low $E_c$ were observed throughout the entire doping level studied, two more things are still needed for a more clarification. The first one is the aging effect which can also cause constricted/pinched *P-E* hysteresis loops. Thus, the deaging procedures, e.g. by applying electric field cycles or by applying thermal, are required to confirm that the observed constricted *P-E* loops in B-site Fe doping is truly a result of the less stabilized ferroelectric order. Second, as the $T_{F\text{-}R}$ is ascribed to be the reason for the discrepancies between A-site and B-site acceptor doping in this study, using other techniques to confirm the obtained $T_{F\text{-}R}$ is also beneficial to the reliability of the results. Finally, it's also of interest to expand the results to other BNT-based systems and see whether the same trend was obtained.

**Output จากโครงการวิจัยที่ได้รับทุนจาก สกว.**

1. ผลงานตีพิมพ์ในวารสารวิชาการนานาชาติ

Comparison of structural, ferroelectric, and piezoelectric properties between A-site and B-site acceptor doped $0.93Bi_{0.5}Na_{0.5}TiO_3$-$0.07BaTiO_3$ lead-free piezoceramics ***manuscript* *แนบในภาคผนวก*

2. การนำผลงานวิจัยไปใช้ประโยชน์

- เชิงพาณิชย์

ไม่มี

- เชิงนโยบาย

ไม่มี

- เชิงสาธารณะ

ไม่มี

- เชิงวิชาการ

สร้างบัณฑิตใหม่ระดับปริญญาเอก คือ นายอนุรักษ์ แวหะยี

สร้างองค์ความรู้ที่เกี่ยวข้อง

3. อื่นๆ (เช่น ผลงานตีพิมพ์ในวารสารวิชาการในประเทศ การเสนอผลงานในที่ประชุม)

นำเสนอผลงานในงานประชุม The 2nd MRS Thailand Meeting 2019, 10th – 12rd July 2019, Pattaya, Thailand (Oral presentation)

# ภาคผนวก

# Comparison of structural, ferroelectric, and piezoelectric properties between A-site and B-site acceptor doped $0.93Bi_{0.5}Na_{0.5}TiO_3$-$0.07BaTiO_3$ lead-free piezoceramics

**Sasiporn Prasertpalichat[1,2,*], Somkiat Kangketkarn[1], Theeranun Siritanon[3], Jaru Jutimoosik[1,2], Pinit Kidkhunthod[4] and Theerachai Bongkarn[1,2]**

[1]*Department of Physics, Faculty of Science, Naresuan University, Phitsanulok, Thailand 65000*

[2]*Research Center for Academic Excellent in Applied Physics, Faculty of Science, Naresuan University, Phitsanulok, Thailand 65000*

[3]*School of Chemistry, Institute of Science, Suranaree University of Technology, Nakhonratchasima, Thailand 30000*

[4]*Synchrotron Light Research Institute (Public Organization), 111 University Avenue, Muang District, Nakhon Ratchasima, Thailand 30000*

## Abstract

The inconsistent and still unclear doping effects in BNT-BT lead-free ceramic as compared to that of PZT is one of the reasons that have limited its usage in practical applications. In this study, A-site Li- and B-site Fe-doped $0.93(Bi_{0.5}Na_{0.5})TiO_3$-$0.07BaTiO_3$ (abbreviated as BNBT) ceramics based on compositions $(Bi_{0.465}Na_{0.465}Ba_{0.07})_{1-x}Li_xTiO_3$ and $(Bi_{0.465}Na_{0.465}Ba_{0.07})Fe_xTi_{1-x}O_3$ ($x$ = 0.01–0.03), respectively, were prepared via conventional solid state mixed-oxide route. The effects of Li and Fe dopant on the structural, microstructure, dielectric, electrical, ferroelectric and piezoelectric properties were systematically investigated. It was found that all samples possessed a coexistence of rhombohedral (*R3c*) and tetragonal (*P4bm*) phases with the phase ratio (*R3c*/*P4bm* ~ 80/20) that are relatively constant and insensitive to an increasing of both Li and Fe doping level. In addition, upon increasing doping level, both Li- and Fe-doped samples also exhibited similar changes: an increase in average grain size, a decrease in resistivity ($\rho$) and a reduction of activation energy for conduction ($E_a$), which are typical characteristics for typical acceptor doping. However, it was found that A-site Li doping can induce the material from ergodic relaxor to ferroelectric order at $x$ =

0.02 as seen from significant increase in $E_c$ (from 11.3, for BNBT, to 30.7 kV/cm) and $P_r$ (from 11.5 to 33.9 μC/cm$^2$) along with the emergence of negative strain. On the contrary, for B-site Fe doping, slight constricted *P*-*E* with a moderate increase in $E_c$ (from 11.3 to 15.1 kV/cm) and $P_r$ (from 11.5 to 28.6 μC/cm$^2$) was observed at $x$ = 0.01 and persisted with only a slight change up to $x$=0.03. The discrepancies will be discussed based on the relaxor nature of BNT-based material, defect dipoles and lattice distortion.

**Keywords:** Lead-free piezoceramics, BNT-BT, hardening characteristics, A-site and B-site acceptor doping

## Introduction

Lead zirconate titanate, $Pb(Zr_xTi_{1-x})O_3$ (PZT), and its derivatives have dominated the piezoelectric market for more than half a century due to their excellent electromechanical properties at the "morphotropic phase boundary" (MPB) [1] [2] and high curie temperature ($T_c$ > 300°C), which enables a broader operating temperature [3]. Moreover, tailoring PZT's properties for specific applications are well established and can be directly done by chemical modification through dopant. For examples, 'hardening' characteristics, which is required for high-power applications such as transformer and ultrasonic motor, can be achieved in PZT simply by acceptor doping on either A- or B-sublattice site of the perovskite structure (e.g. $Fe^{3+}$/$Mn^{3+}$replacing $Ti^{4+}$/$Zr^{4+}$ or $K^+$ replacing $Pb^{2+}$). This causes a formation of negatively-charged defects (e.g. $Fe'_{Ti}$) along with compensating oxygen vacancies ($V_O^{\cdot\cdot}$). And it is widely accepted that these mobile charged defects either in the form of single ion (e.g. $V_O^{\cdot\cdot}$) or defect dipoles (e.g. $Fe'_{Ti}-V_O^{\cdot\cdot}$) could stabilize domain configurations and lead to a reduction of polarization contributions to the electrical response. Accordingly, the materials exhibit 'hard-type' characteristics which include a lowered electrical resistivity (i.e. higher conductivity), a

decrease in the piezoelectric coefficient, dielectric permittivity ($\varepsilon_r$) and dielectric loss (tan $\delta$), along with an increase in $Q_m$ and coercive field ($E_c$) as well as more pronounced aging effects [4] [5] [6]. However, lead oxide (PbO), which is the main component in PZT (~ 60-70 wt%), is highly toxic to both environment and human health, resulting in a restriction of its use in many countries around the globe [7]. Therefore, a search for lead-free piezoelectric ceramics with comparable properties to that of PZT is crucial.

Among the available lead-free materials, the solid solution between rhombohedral $Bi_{0.5}Na_{0.5}TiO_3$ (BNT) and tetragonal $BaTiO_3$ (BT), (1–$x$)BNT–$x$BT, has received much attention due to its superior ferroelectric and piezoelectric properties at the MPB around $x$ = 0.055-0.07, similar to what observed in PZT [8] [9]. Acceptor doping have also been investigated extensively in BNT-based systems by adopting typical A- and B-site acceptor dopants used in PZT. However, B-site acceptor doped BNT-based ceramics only displayed a slight or moderate hardening characteristics. For examples, independent studies of $Fe_2O_3$-doped BNT [10] and BNKT exhibited only a small increase in coercive field ($E_c$) [11] even though the defect dipoles responsible for hardening characteristics were clearly detected,. Likewise, Sapper *et al.* [12] reported a small or absence of aging effects in 1 at% Fe doped (1-$x$)BNT-$x$BT ($x$ = 0.01). The less pronounced hardening and aging effects were attributed to the relaxor nature of BNT-based materials, which makes stabilized domain volume smaller than that of the ferroelectric PZT. Similarly, hard-type characteristics like an increase in $E_c$ or internal bias field were very difficult to discern in Fe-doped 92BNT-6BT-2KNN [13] due to the constricted *P-E* hysteresis loop arising from the ergodic relaxor nature of the base composition. Meanwhile, though an increase in $Q_m$ was observed in a study of Mn-doped 92BNT-BT [14], a conclusion that it was a hardening characteristic from microscopic origin cannot be made as the microstructure and density also changed.

Compared to their B-site counterpart, the amount of reports on hardening characteristics due to A-site modifications are relatively small. Most of previous works mainly focused on the effects of A-site nonstoichiometry on the electrical conductivities and leakage currents since both Bi and Na are volatile elements and tend to escape during high temperature sintering [15] [16] [17] [18]. Lately, after oxygen vacancies have been revealed to be the dominant conduction species in Bi-deficient BNT [16], attention has also been paid toward the development of BNT as oxide ion conductor through A-site acceptor doping [19]. Though the number of studies based on A-site acceptor-doped BNT-based systems are very limited, satisfactory hardening characteristics due to A-site modifications (through adjusting Bi/Na ratio) were recently shown in a comprehensive study of (1-$x$)BNT–$x$BT at the compositions near the MPB ($x$ = 5.5, 6 and 7 mol%) [20]. All "hardening" characteristics including an increase in $E_c$, $Q_m$, as well as a decrease in $P_r$, $d_{33}$, $\varepsilon_r$, and tan $\delta$ were obtained in all Na-excess samples. Moreover, an increase in $E_c$ and a decrease in $P_r$ were further confirmed by remanent hysteresis measurements. Also, Yesner *et al.* [21] observed a drastic increase in $Q_m$ in Bi-deficient BNT-BKT-BT ceramics.

Given that hardening characteristics due to A-site stoichiometry modification exhibited promising results as compared to its B-site counterpart, it is very interesting to investigate whether the same or more pronounced hard-type characteristics could be obtained by other A-site acceptor dopants. To the best of our knowledge, there has been no report that systematically compare the effect of A-site and B-site acceptor dopants in (1–$x$)BNT–$x$BT at the MPB compositions. Therefore, in this study, the 0.93BNT-0.07BT, which was the MPB composition exhibiting the highest degree of hardening in previous study [20], will be chosen as a starting composition. The roles of Li as A-site and Fe B-site acceptor-doped 0.93BNT-0.07BT will be compared and investigated through

systematic studies of crystal structure, dielectric, electrical conductivity, piezoelectric and ferroelectric properties. Due to the reported inconsistencies of doping effects between lead-free and PZT materials as well as the fact that comprehension of doping outcome is one of the key requirements for employing material in practical use, this study is expected to provide more understanding on the doping effect, particularly acceptor doping, in the MPB composition of BNT-BT which is widely used as base composition in various studies.

**Method and procedure**

Ceramic samples based on the compositions $(Bi_{0.465}Na_{0.465}Ba_{0.07})_{1-x}Li_xTiO_3$ (abbreviated as Li100*x*), for A-site Li doping, and $(Bi_{0.465}Na_{0.465}Ba_{0.07})Fe_xTi_{1-x}O_3$ (abbreviated as Fe100*x*), for B-site Fe doping, where $x$ = 0-0.03, were prepared via conventional solid state mixed oxide route. Reagent-grade powders of $Bi_2O_3$ (99.9%, Sigma Aldrich), $Na_2CO_3$ (99.95%, Alfa Aesar), $TiO_2$ (99%, Sigma Aldrich), $BaCO_3$ (99.9%, Alfa Aesar), $Li_2CO_3$ (99%, Merck) and $Fe_2O_3$ (99%, Sigma Aldrich), were used as starting chemicals. The starting materials were weighted according to the required chemical formula and then ball-milled in ethanol with yttrium-stabilized zirconia as a media for 24 h before subsequently dried in the oven for 24 h. After that, the milled powders were calcined at 800°C and followed by re-milling and drying step to ensure that the achieved powders were in sub-micron sized range. The obtained powders were then mixed with 3 wt% polyvinyl butyral (PVB) and pressed into disc pellets with 15 mm in diameter. The pellets were sintered at temperature between 1150 to 1175°C in a covered crucible for 2 h with a polymer burned out step at 400°C for 3 h. It should be noted that all green pellets were embedded in sacrificial powders of the same composition in order to minimize the loss of the volatile Bi and Na components during sintering. Phase purity

and crystal structure were identified by X-ray diffraction (XRD, Bruker D8 Advance) on crushed sintered ceramics using Cu $K_\alpha$ radiation. Two sets of scans were performed, one with an addition of NaCl as internal standard in the 2θ range of 10º-80º with a 0.02º step-size and 1 s/step scan speed. The other scan was without standard in the range 10º-120º with a 0.02º step-size and 2 s/step scan speed. The obtained XRD data were further analyzed by using the Le Bail and Rietveld refinement technique via the TOPAS software. Then the synchrotron x-ray absorption near edge structure (XANES) spectroscopy were conducted on BNBT-*x*Fe samples at ambient temperature at XAS beam line (BL5.2 SUT-NANOTECT-SLRI) of Synchrotron Light Research Institute (SLRI), Thailand, with provided electron energy of 1.2 GeV and beam current of 140-80 mA. The Ti and Fe *K*-edge XANES spectra were measured in the fluorescent mode and the signals were collected by using a four-element Si drift detector. A double crystal monochromator Ge(220) was used to scan the photon energy. For Ti and Fe K-edge XANES measurements, the scanning step was set at 0.2 eV in the photon energy range of 4500-5400 eV and 7100-7200 eV, respectively. The normalized XANES data were processed and analyzed after background subtraction in the pre-edge and post-edge region using the ATHENA software. The linear combination analysis (LCA) method in the ATHENA program as implement in IFEFFIT package was used for the data fitting [22].

Prior to electrical measurements, samples were ground and polished to ~0.7-0.8 mm thick and then silver paste (Heraeus C1000) was applied on both sides and fired at 700°C for 0.5 h. The temperature and frequency dependence of dielectric properties were measured by Agilent 4263B LCR Meter on poled samples. It's worth noting that all samples were poled by applying a dc electric field at 50 kV/cm for 0.5 h at room temperature. The impedance spectroscopy was conducted over a wide temperature (~460-540°C) and frequency range (20 Hz-10MHz) using Keysight impedance gain/phase

analyzer (model 4194A). The electric field induced polarization (*P*-*E*) and strain (*S*-*E*) measurements were measured by using a Precision Premier II, Radiant technology. The low field piezoelectric coefficient ($d_{33}$) was measured using a YE2730A d33 meter.

**Results and discussion**

Figure 1(a) displays room temperature X-ray diffraction (XRD) patterns of BNBT–*x*Li and BNBT–*x*Fe (*x* = 0, 0.01, 0.02 and 0.03) crushed sintered pellets. It is noteworthy that NaCl was used as an internal standard to obtain a better determination of lattice parameter changes due to Li and Fe doping. Thus, apart from the peaks corresponding to NaCl (marked with asterisk (*) in Fig. 1(a)), it can be seen that all samples exhibited a single-phase perovskite structure with no trace of any secondary phases, suggesting that $Li^+$ and $Fe^{3+}$ ions diffused into lattice site and form a complete solid solution with BNBT. For pure BNBT (i.e. 0.93BNT-0.07BT), the rhombohedral characteristic (111) peak at $2\theta \sim 40°$ (Fig 1(b)) and tetragonal characteristic (200) reflection at $2\theta \sim 46°$ (Fig 1(c)) displayed a single broad peak with no visible shoulder or peak splitting, indicating that the prepared BNBT possessed pseudocubic structure. The result is consistent with previous studies in which the average structure of (1-*x*)BNT-*x*BT at the MPB compositions (*x*=0.055-0.07) were reported to be near cubic [23] or pseudocubic with a minor tetragonal and rhombohedral distortion [24] [25]. In case of Li-doped BNBT ceramics, a single broad (111) and (200) peaks persisted up to *x*=0.02 (Li2). However, when *x* reached 0.03 (Li3), the (111) peak became broader and a small but noticeable bump on the higher angle was started to be observed; meanwhile, the (200) peak also broadened, implying that the degree of tetragonal and rhombohedral distortion increased. In addition, it was found that the peaks shifted toward higher $2\theta$ with increasing Li doping. This indicates that the lattice site is reduced, which can be attributed to a smaller

ionic radii of $Li^+$ ion (~ 1.20 Å) [19] [26] as compared to that of $Bi^{3+}$ (1.38 Å), $Na^+$ (1.39 Å) and $Ba^{2+}$ (1.61 Å) [27] on the A-site. On the other hand, for BNBT-*x*Fe ceramics (*x*=0.01-0.03), neither shoulder nor peak splitting of (111) and (200) peaks were observed across the entire range of Fe doping level studied, suggesting that pseudocubic structure persisted in all Fe-doped BNBT ceramics and that Fe doping had little to no effect on the structural changes. Besides, a relatively small downward peak shift, which indicates an expansion of unit cell volume, was detected upon increasing Fe doping level and it can be ascribed to a larger ionic radius of $Fe^{3+}$ (0.645 Å) that substitutes for $Ti^{4+}$ (0.605 Å) [27]. The results are well consistent with previous reports on Fe-doped BNKT [11] and 0.94BNT-0.06BT ceramics [28] in which a slight peak shift were also reported. A less pronounced peak shift in Fe-doped BNBT ceramics may arise from a smaller difference between ionic radii of $Fe^{3+}$dopant and $Ti^{4+}$host ion on B-site in comparison to those on the A-site ($Li^+$ Vs $Bi^{3+}$, $Na^+$ and $Ba^{2+}$).

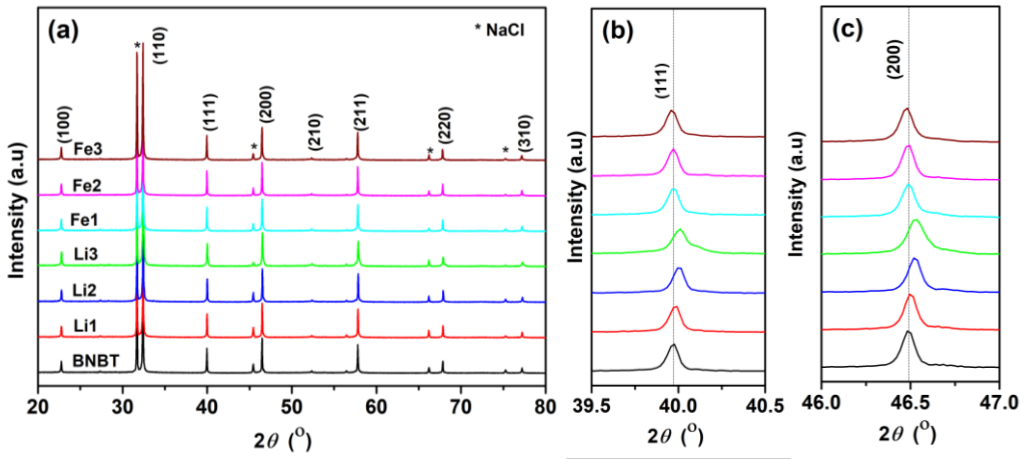


**Fig. 1.** Room temperature XRD patterns of BNBT-*x*Li and BNBT-*x*Fe ceramics (*x* = 0, 0.01, 0.02 and 0.03) in the 2$\theta$ range of (a) 20-80° (b) 39.5-40.6° and (c) 46.0-47.0°

Since the base composition (0.93BNT-0.07BT) in this study is at the MPB where two phases coexist, Rietveld refinement technique was performed on all samples' XRD data to provide more insight on the effect of Li and Fe doping on structural change

especially the phase fraction, which have been shown to have a significant effect on the electrical properties. For the present study, the use of two-phase model consisting of rhombohedral (space group *R3c*) and tetragonal (space group *P4bm*) phases provided the optimum fit, consistent well with previous reports of similar compositions [29] [30]. In addition, it's worth noting that two sets of refinement were performed in this study. First, the accurate cell parameters of both phases were obtained from a Le Bail refinement using XRD patterns collected with internal standard addition (i.e. NaCl). Then, the obtained values were fixed in Rietveld refinement so that the number of correlated parameters was minimized. The structural information obtained from [31] was used as a starting model. Background data was refined by using Chebyshev function with six polynomial coefficients whereas the atomic occupancies were assumed to be equal to the chemical formula of each composition and were not refined. The calculated profile from Rietveld refinement along with corresponding experimental XRD data of BNBT-*x*Li and BNBT-*x*Fe ceramics are demonstrated in Fig.2. Related refinement data including phase fraction, lattice parameters and fitting quality values are listed in Table I. The reliability factors (see Table I) and the good fit between calculated and observed data (see Fig. 2) indicate that the samples are well described by the refined models. For BNBT (i.e. undoped 0.93BNT-0.7BT) the refined phase fraction of *R3c* and *P4bm* were 84.11% and 15.89%, respectively, which correspond well with previous results obtained from the refinement of both laboratory (93% *R3c*+7% *P4bm*) [29] and high-resolution XRD data (77.7% *R3c*+22.3% *P4bm*) [31]. With increasing either Li or Fe doping level (*x*) from 0.01 to 0.03, it was found that the *R3c* phase fraction changed in the range of ~79%–85% and that of *P4bm* varied between ~15 to ~21%, respectively. This relatively small change of both *R3c* and *P4bm* phase fraction (i.e. less than ±5% variation) as compared with the base composition BNBT suggests that both A-site (Li) and B-site (Fe) acceptor doping

had little or no influences on the constituent phases. Previous studies from Xu *et al*. [30] observed a substantial change of phase fraction from 49.5% *R3c*+50.5% *P4bm*, for $x = 0$, to 24.8% *R3c*+75.1% *P4bm*, for $x = 0.10$, in (1-*x*)(BNT-BT)-*x*$NaTiO_3$ ceramics. Similar phenomenon was also observed in Li-doped BNT-BT-*x*$CaTiO_3$ [29], in which a variation from 93% *R3c*+7% *P4bm* ($x = 0$) to 43% *R3c*+57% *P4bm* ($x = 0.15$) was reported. Thus, a fairly small change in phase fraction in this study may be ascribed partly to a lesser amount of doping ($x \leq 0.03$) compared to that of previous reports ($x \sim 0.10$ or 0.15). Nevertheless, it was observed that the changes in unit cell volume, obtained from the refinement, agreed well with the observed XRD peak shift in Fig. 1 where both *R3c* and *P4bm* unit cell volume gradually decreased with increasing Li content while they continuously increased upon increasing Fe dopant.

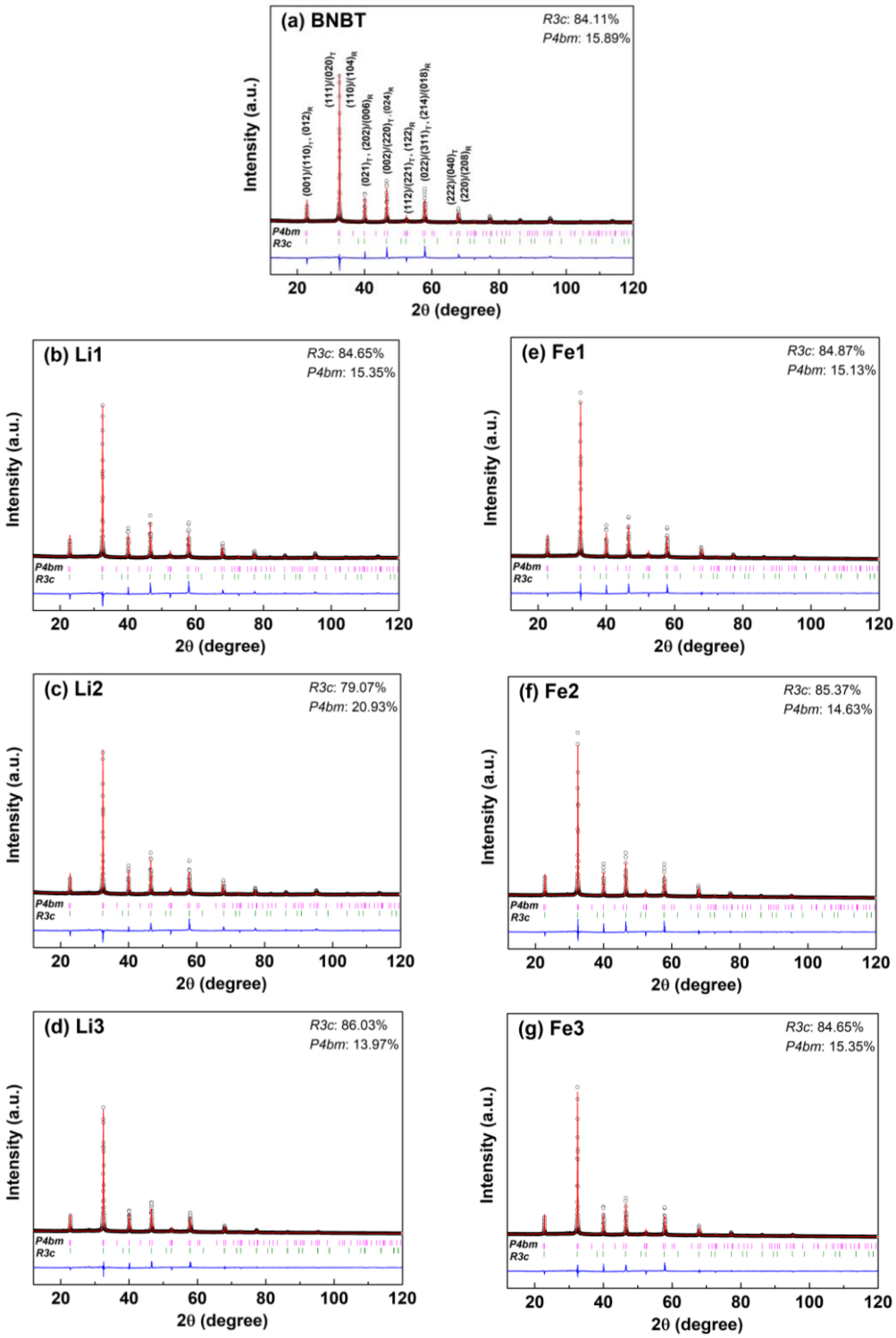


**Fig. 2.** Room temperature XRD patterns of BNBT-*x*Li and BNBT-*x*Fe ceramics, $x = 0.01$-$0.03$. The black circles represent experimental data and the red lines correspond to the calculated profile from Rietveld refinement. The blue lines are differences between the experimental and the refined diffraction patterns. The allowed Bragg reflections for *P4bm* and *R3c* space groups are indicated by pink and green ticks, respectively.

**Table I** Phase fraction, calculated lattice parameters and fitting quality values of BNBT-*x*Li and BNBT-*x*Fe samples obtained from the Rietveld refinement of room-temperature XRD data.

| | Phase fraction (%) | | *R3c* | | | *P4bm* | | | $\%R_{wp}$ | $\%R_p$ |
|---|---|---|---|---|---|---|---|---|---|---|
| | *R3c* | *P4bm* | a (Å) | c (Å) | vol (Å$^3$) | a (Å) | c (Å) | vol (Å$^3$) | | |
| BNBT | 84.1 | 15.9 | 5.5219(2) | 13.526(1) | 357.2 | 5.4904(4) | 3.9498(4) | 119.1 | 11.27 | 8.24 |
| Li1 | 84.7 | 15.3 | 5.5206(2) | 13.523(1) | 356.9 | 5.4877(4) | 3.9511(4) | 119.0 | 11.47 | 8.37 |
| Li2 | 79.1 | 20.9 | 5.5187(2) | 13.517(1) | 356.5 | 5.4929(4) | 3.9430(4) | 119.0 | 10.89 | 8.02 |
| Li3 | 86.0 | 14.0 | 5.5196(2) | 13.510(1) | 356.4 | 5.4953(3) | 3.9376(3) | 118.9 | 11.88 | 8.39 |
| Fe1 | 84.9 | 15.1 | 5.5225(2) | 13.526(1) | 357.3 | 5.4918(3) | 3.9523(4) | 119.2 | 12.06 | 8.31 |
| Fe2 | 85.4 | 14.6 | 5.5226(2) | 13.527(1) | 357.3 | 5.4907(4) | 3.9541(4) | 119.2 | 12.59 | 8.78 |
| Fe3 | 81.0 | 19.0 | 5.5241(2) | 13.530(1) | 357.6 | 5.4950(4) | 3.9494(4) | 119.3 | 11.94 | 8.26 |

The synchrotron x-ray absorption near edge structure (XANES) spectroscopy is an element specific technique that can probes the absorption edge of the desired element to gain structural information about its valence state and local environment. This technique can thus be used to identify the lattice site of an atomic species, e. g. a dopant, in a known matrix [32] [33]. The measured Ti and Fe *K*-edge XANES spectra measured for BNBT and BNBT-xFe ceramics are compared with standard $TiO_2$ ($Ti^{4+}$) and $Fe_2O_3$ ($Fe^{3+}$) powders, as shown in Fig. 3(a) and 3(b), respectively. Under most circumstances, XANES also allows for the determination of cation valences. The higher the oxidation number, the further the position of absorption edge is shifted toward higher energies as compared to the neutral metallic state. As indicated by XANES spectra in Fig. 3, the position of absorption edge at Ti *K*-edge of all samples resembles that of the $TiO_2$ standard, showing that Ti species in all samples is $Ti^{4+}$, as expected. For Fe K-edge, one can easily see that the edge position of all BNBT-*x*Fe ceramics is higher than that of the $Fe^{3+}$ at approximately 7126 eV. Thus, this result indicates that the majority Fe ions in our samples possessed the mixed valence state of $Fe^{3+}$ and $Fe^{4+}$. Moreover, all the spectral feature of Fe K-edge also look similar to those of Ti K-edge of BNBT-*x*Fe ceramics, suggesting that the local structure surrounding Fe atoms in BNBT-*x*Fe ceramics is similar

to that of Ti atoms, which means Fe substituting for Ti in BNBT-*x*Fe ceramics. This result introduced oxygen vacancies leading to a distortion of the local symmetry.

To gain information about the local atomic structure and the size occupancy of Fe dopant in BNBT structure, calculation of XANES spectra was performed using the ab initio FEFF8.2 code with the self-consistent and full multiple-scattering options [34]. The spherical cluster size of electron wave function was increased until the spectra converged. The theoretical Ti and Fe K-edge XANES spectra, which correspond to BNBT-*x*Fe ceramics, were calculated in terms of a cluster derived from the average structure determined from our XRD result. Clusters with a size up to eight shells, containing at least 110 atoms, around the absorber (Ti and Fe atoms) were used to calculatethe XANES spectra based on BNBT *P4bm* and *R3c* crystallographic phases. The calculated XANES spectra of Ti and Fe substituting on the Ti site in BNBT *P4bm* and *R3c* structures are shown in Fig. 3(c) and (d), respectively. It is clear that the calculated XANES spectra are in very good agreement with the measured spectra of BNBT-*x*Fe ceramics, this implies that the local structure around Ti atom in BNBT-*x*Fe ceramics have a mixed phase between *P4bm* and *R3c* in a ratio of 20:80. This result is consistent with the phase fraction from our XRD analysis. Furthermore, calculation of Fe K-edge XANES spectra reveals that Fe dopant prefer to substitute on the Ti site of BNBT *R3c* structure, suggesting that the occupancy behavior of Fe dopant depend on doping level and preparation methods.

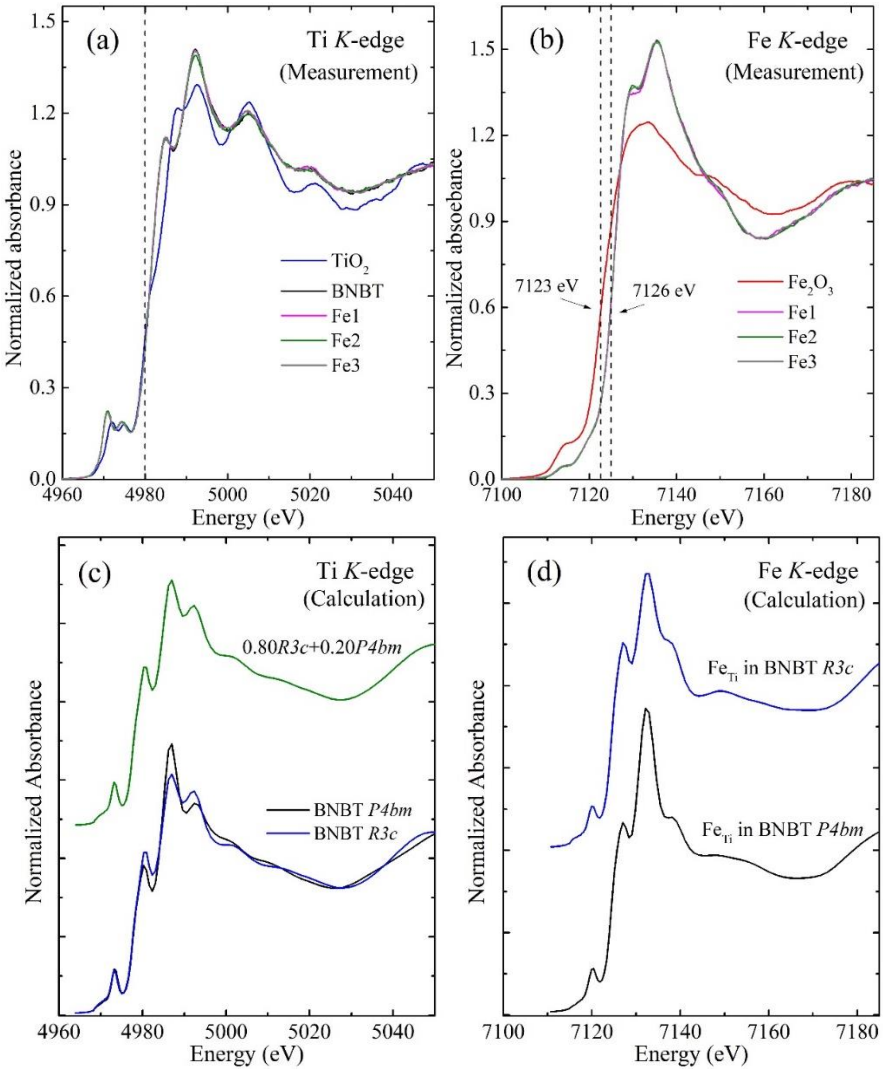


**Fig 3**. Measured (a) Ti *K*-edge, (b) Fe *K*-edge XANES spectra of BNBT-*x*Fe ceramics with comparison to $TiO_2$ and $Fe_2O_3$ standards and calculated (c) Ti *K*-edge, (d) Fe *K*-edge XANES spectra of BNBT *P4bm* and *R3c* structures.

Fig. 4(a)–(g) illustrates SEM micrographs of BNBT-*x*Li and BNBT-*x*Fe (*x*=0-0.03) ceramics thermal etched at 1000°C for 20 mins. All samples exhibited dense microstructure with a mixture of small and large irregular-sized grains. With increasing doping level (*x*), the average grain size calculated by using linear intercept method gradually increased from 0.68±0.11 μm (*x* = 0) to 0.99±0.13 μm (Li1), 1.23 ± 0.19 μm (Li2), and 1.25 ± 0.13 μm (Li3), for Li doping, and to 0.99 ± 0.16 μm (Fe1), 1.16 ± 0.15 μm (Fe2) and 2.10±0.29 μm (Fe3), for Fe doping. In this study, acceptor doping on A-

site with Li or on B-site with Fe can cause negatively charged defects along with the compensating oxygen vacancies according to the following defect reactions:

$$Li_2O \xrightarrow{2(Bi_{0.465}Na_{0.465}Ba_{0.07})TiO_3} 2Li'_{(Bi_{0.465}Na_{0.465}Ba_{0.07})} + V_O^{\cdot\cdot} + O_O^X \quad (1)$$

$$Fe_2O_3 \xrightarrow{2(Bi_{0.465}Na_{0.465}Ba_{0.07})TiO_3} 2Fe'_{Ti} + V_O^{\cdot\cdot} + 3O_O^X \quad (2)$$

It's generally known that oxygen vacancy can help facilitate the mass transportation during sintering process and result in a promotion of grain growth [35]. Thus, a continuous increase in grain size with increasing Li and Fe doping level could be attributed to an increase in oxygen vacancy concentrations generated upon increasing doping content. Similar results were also observed in Li-doped BNKT [36] and BNT-KNN [37] as well as Mn-doped 0.94BNT-0.06$BiAlO_3$ [38].

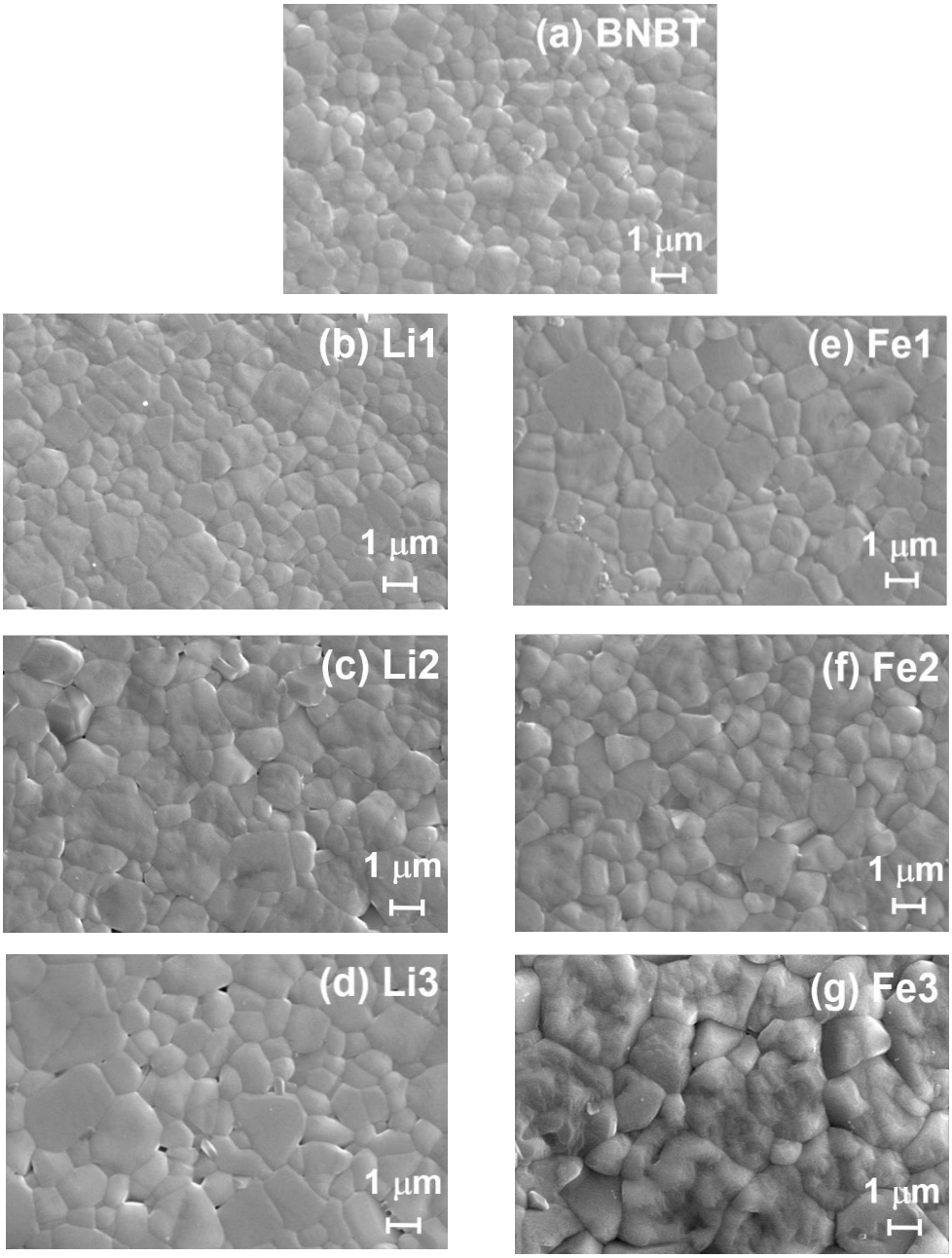


**Fig. 4.** SEM micrographs of BNBT-*x*Li and BNBT-*x*Fe ceramics ($x$ = 0, 0.01, 0.02 and 0.03)

Temperature dependence of relative permittivity ($\varepsilon_r$) and loss tangent ($\tan\delta$) of poled BNBT-*x*Li and BNBT-*x*Fe ceramics measured from room temperature (RT) up to 450°C at frequency of 1 Hz–100 kHz were illustrated in Fig. 5(a)–(g). For both BNBT-*x*Li and BNBT-*x*Fe ceramics, two dielectric anomalies were observed throughout the entire temperature and frequency range studied. The first one at the temperature of $T_m$

~300°C is characterized by maximum dielectric permittivity ($\varepsilon_{r,\ m}$) with frequency independent while another one at a lower temperature of $T_{F\text{-}R}$ (i.e. ferroelectric-to-relaxor transition temperature) is categorized by frequency-independent discontinuity peak in both $\varepsilon_r$–T and tan$\delta$–T curves (indicated by arrow in Fig. 5(a)–g)). The origin of $T_m$ has been recently accepted to arise from two successive processes that occur upon increasing measuring temperature: (1) a transition from rhombohedral (*R3c*) to tetragonal (*P4bm*) polar nanoregions (PNRs) and (2) a relaxation of *P4bm* PNRs emerged from *R3c* [39] [40]. Meanwhile, the origin of $T_{F\text{-}R}$ is ascribed to a breakdown of electric-field-induced ferroelectric order from the non-ergodic relaxor (NER) state (i.e. a state where materials irreversibly transform into ordered FE domain under applied electric field and sustain even E-field is removed) into ergodic relaxor (ER) upon heating the materials [39] [41]. The temperature and frequency dependence of dielectric properties in this study corresponded well to the proposed framework.

To better compare the effects of A-site (Li) and B-site (Fe) acceptor doping on dielectric properties, extracted parameters from $\varepsilon_r$–T curves (at 1 kHz) including $T_{F\text{–}R}$, $T_m$, $\varepsilon_{r,\ m}$, room temperature $\varepsilon_r$ ($\varepsilon_{r,\ RT}$) along with their corresponding tan$\delta$ are listed in Table II. From Table II, it can be seen that $T_{F\text{-}R}$ significantly increased from 26°C (BNBT) to 37°C, 67°C and 97°C for Li1, Li2 and Li3, respectively, while it moderately increased to 36°C (Fe1) and 45°C (Fe2) before slightly dropped to 41°C (Fe3). The $T_{F\text{–}R}$ is known to be correlated with the stability of ferroelectric order (i.e. the higher the $T_{F\text{-}R}$ is, the stronger domain configuration the material possesses) [42]. And it is widely accepted that the oxygen vacancies can stabilize the ferroelectric domain in perovskite oxide materials [43]. Thus, an upward shift of $T_{F\text{–}R}$ with increasing either Li or Fe acceptor doping level in this study is most likely be a result of an increase in oxygen vacancy concentration which is generated according to the abovementioned defect reactions (equation (1) and

(2)). Similar results have also been reported in other acceptor-doped BNT-based ceramics including $(Bi_{0.47}Na_{0.47}Ba_{0.06})Ti_{1-x}Fe_xO_{3-\delta}$ ($x$ = 0–0.03) [28] and $Bi_{1/2}(Na_{0.8}K_{0.2})_{1/2}(Ti_{1-x}Fe_x)O_{3-x/2}$ ($x$ = 0–0.03) [11], $0.96(Bi_{0.5}Na_{0.5})(Ti_{1-x}Mn_x)O_3$–$0.04BiAlO_3$ ($x$ = 0–0.01 mol%) [38] and $(1-x)(Bi_{1/2}Na_{1/2})TiO_3$-$x(Bi_{1/2}Li_{1/2})TiO_3$ ($x$ = 0–0.24) [44]. In contrast to the change in $T_{F-R}$, it was found that $T_m$ increased from 306°C (BNBT) to 326°C (Li3) for Li doping but decreased to 288°C (Fe3) for Fe doping. Due to the complication behind the origin of $T_m$, the reason for its shifting is still inconclusive. Both upward [38] [45] [46] and downward [47] shift of $T_m$ have been reported in previous studies of acceptor doped BNT-based ceramics. However, regardless of the type of acceptor dopant used, a sharp rise in tan$\delta$ at fairly high temperature (>400°C) was noticed in both Li- and Fe-doped BNBT ceramics with high doping content (e.g. Li2, Fe2, Li3, Fe3). This could be attributed to oxygen vacancies that can be thermally activated at high temperature [28], thus leading to an increase in tan$\delta$ at elevated temperature, as was also shown previously in other acceptor-doped BNT–based ceramics e.g. Mn-doped 0.94BNT–0.04BA [38], Mn-doped BNBK [46] and Fe-doped BNBT [28].

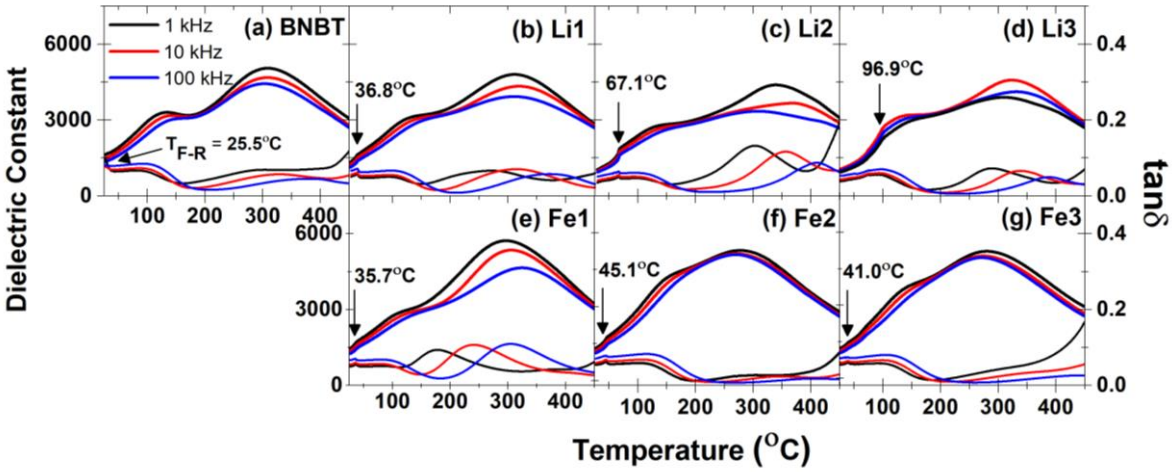


**Fig. 5.** Temperature dependence of relative permittivity ($\varepsilon_r$) and dielectric loss (tan $\delta$) for poled BNBT-$x$Li and BNBT-$x$Fe ceramics, $x$ = 0.01, 0.02 and 0.03 measured at 1, 10 and 100 kHz**.**

**Table II** Related dielectric properties parameters of unpoled and poled BNBT–*x*Li and BNBT– *x*Fe ceramics

| Compositions | $T_{F\text{-}R}$ (°C) | $T_m$ (°C) | $\varepsilon_{r,RT}$ | $\tan\delta_{RT}$ | $\varepsilon_{r,m}$ | $\tan\delta_m$ |
|---|---|---|---|---|---|---|
| BNBT | 26 | 306 | 1666 | 0.09 | 5045 | 0.06 |
| Li1 | 37 | 311 | 1391 | 0.05 | 4780 | 0.06 |
| Li2 | 67 | 337 | 1032 | 0.03 | 4380 | 0.09 |
| Li3 | 97 | 326 | 1087 | 0.04 | 4574 | 0.06 |
| Fe1 | 36 | 291 | 1529 | 0.05 | 5714 | 0.04 |
| Fe2 | 45 | 287 | 1364 | 0.05 | 5265 | 0.02 |
| Fe3 | 41 | 288 | 1282 | 0.05 | 5204 | 0.04 |

To investigate the conduction mechanism and further explain the observed sharp rise in tan$\delta$ at high temperature observed in previous section, impedance spectroscopy technique was conducted on all samples. Figure 6(a)–(f) shows the complex plane ($Z^*$) plots of BNBT-*x*Li and BNBT-*x*Fe ceramics measured in the temperature range of 460–540°C at 20 Hz–10 MHz. For BNBT, the $Z^*$ plot showed a single semicircle corresponding to the bulk response. With increasing either Li or Fe doping content, a depressed single semicircle with an asymmetric arc at low frequency was clearly observed, indicating an increase in contribution from grain boundary. More details on the effects of Li and Fe will be discussed in the following paragraph. Nonetheless, in all samples, it can be seen clearly that the resistance values progressively decreased with the rise in temperature, conforming to the negative temperature coefficient of resistance (NTCR) effect commonly observed in various semiconductors [48] e.g. BNT-BT-*x*NN [49] and BNT-BT-*x*Cz [50]. This behavior can be attributed to the thermal activation of weakly trapped charge carriers [51]. The impedance data were also replotted in the form of $Z''(f)$ spectroscopic plots as demonstrated in Fig. 7(a)–(g). All samples exhibited a shift of $Z''$ peak toward higher frequencies along with a reduction of $Z''$ values with increasing temperature. This indicates a reduction of samples' resistance with an increase in temperature, consistent well with the behavior observed in $Z^*$ plots.

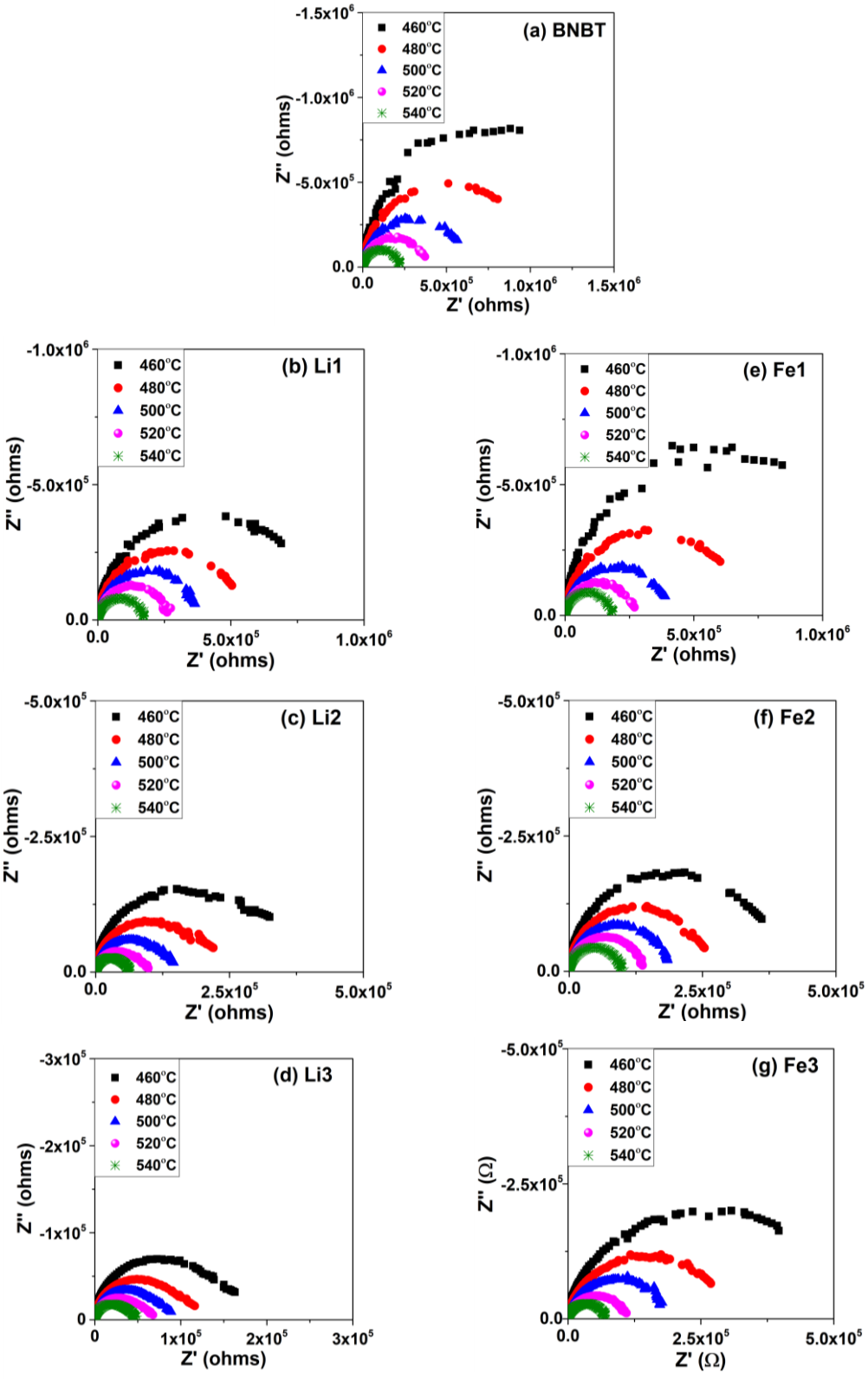


**Fig. 6.** Impedance complex plane plots (Z*) of BNBT–*x*Li and BNBT–*x*Fe ceramics, *x* = 0.01, 0.02 and 0.03, ceramics measured in the temperature range of 460°C-540°C.

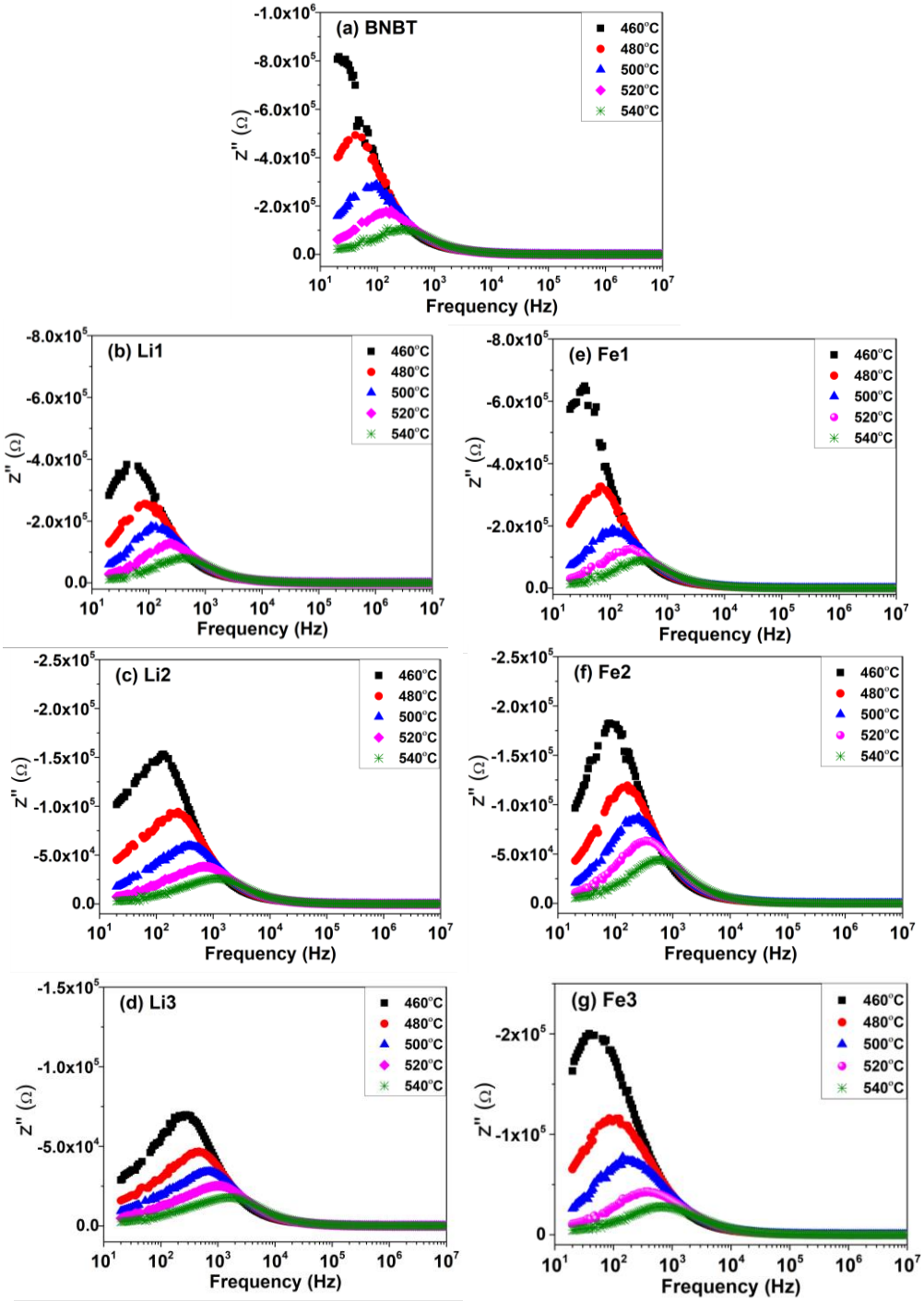


**Fig. 7.** The Z′′(f) spectroscopic plots of BNBT–*x*Li and BNBT–*x*Fe ceramics, $x = 0.01$, 0.02 and 0.03, ceramics measured at different temperatures and frequencies ($T$=460°C–540°C, $f$ = 20 Hz–10 MHz).

For a better comparison on the effect of Li and Fe doping, the complex plane (Z*) and corresponding normalized Z′′(f) spectroscopic plots ($Z''/Z''_{max}$) at 540°C of BNBT–*x*Li and BNBT–*x*Fe ceramics were compared as shown in Fig. 8(a)–(d). In addition, the

resistivities (ρ), calculated from low frequency arc intersection on *x*-axis (Z′) and sample's dimension, are also listed in Table III. From Fig. 8 (a), (b) and Table III, it is clearly observed that increasing either Li or Fe doping content resulted in a continuous decrease of resistivity from 3.21 (BNBT) to 2.18, 0.98 and 0.72 MΩ.cm (for Li1, Li2 and Li3) and to 2.56, 1.56 and 1.02 MΩ.cm (for Fe1, Fe2 and Fe3), respectively. Moreover, it was found that the semicircular arc at low frequency became more apparent at high doping level for both Li- and Fe-doped BNBT compositions e.g. Li3, Fe3. This observation was evidently supported by the normalized Z′′(f) plots (Fig. 8(c)–(d)) where a single Debye peak for BNBT clearly evolved into a broad peak with noticeable asymmetry at low frequency region with increasing Li or Fe doping content. The broadness of Debye peak was further confirmed by extracting the full width at half maximum (FWHM) (marked by arrow in Fig 8(c) and (d)). For BNBT, the FWHM of 1.20 decades was obtained, which is close to the ideal theoretical values of 1.14 decades [52]. With increasing doping level (*x*), the FWHM increased to 1.22, 1.41 and 1.58 decades for Li1 Li2 and Li3, respectively; meanwhile, it also increased to 1.16, 1.27 and 1.48 for Fe1, Fe2 and Fe3. The observed behaviors in both Z* and normalized Z′′(*f*) plots evidently suggest that the grain boundary contribution became more prominent upon increasing either Li or Fe doping content. Similar result was also reported in KNN modified 0.94BNT-0.06BT ceramics [50].

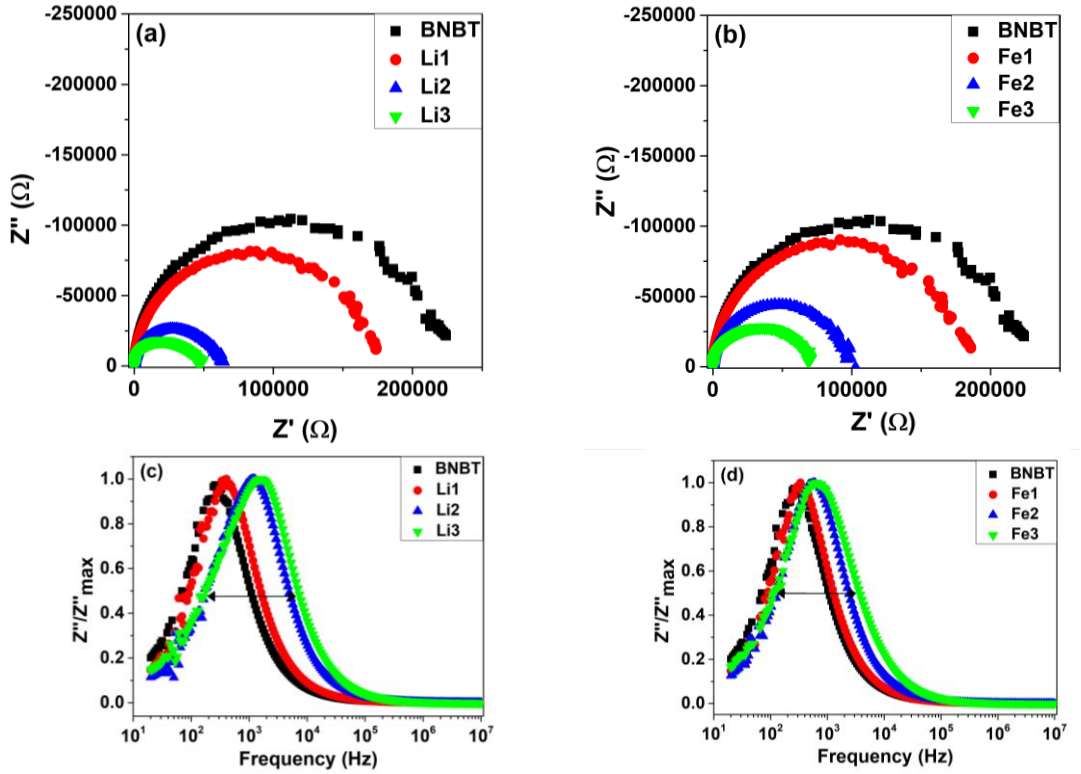


**Fig. 8.** The complex plane (Z*) plots at 540°C of (a) BNBT–*x*Li and (b) BNBT–*x*Fe ceramics along with the corresponding normalized Z′′(f) spectroscopic plots at 540°C of (c) BNBT–*x*Li and (d) BNBT–*x*Fe ceramics.

To analyze the activation energy of conduction ($E_a$), the plots of 1000/T versus lnσ for BNBT-*x*Li and BNBT–*x*Fe ceramics are demonstrated in Fig. 9(a) and (b), respectively. All plots obeyed the Arrhenius law, which is expressed as:

$$\sigma = \sigma_0 . exp\left[-\frac{E_a}{k_B T}\right] \quad (3)$$

where $\sigma_0$ is constant, $E_a$ is the activation energy of conduction, $k_B$ is Boltzmann constant and $T$ is temperature in Kelvin. By calculating the slope of the fitted graphs, the $E_a$ magnitudes for each composition were obtained as listed in Table III. For $ABO_3$ perovskite materials, $E_a$ magnitudes varies depending on the type of conducting species. For example, doubly ionized oxygen vacancies ($V_O^{\cdot\cdot}$) can be thermally activated at high temperature with associated $E_a$ of 1.005–1.093 eV [53] [54] [55] while $E_a$ for intrinsic band-type electronic conduction for BNT-BT based materials were reported to be

approximately half of the band gap ($E_g/2$ ~1.6–1.7 eV) [56] [57]. In the present study, the pure BNBT ceramic possessed $E_a$ of 1.33 eV, agreeing well with that of previous studies on BNT-based systems which reported $E_a$ in the range of 1.3–1.7 eV [58] [59]. With increasing doping level, despite some fluctuation, $E_a$ exhibited a decreasing trend to 0.86 eV (Li3) and 1.29 eV (Fe3). Though $E_a$ in the samples with high level of $x$ content (e.g. Li2, Fe3) fell in the range of oxygen ionic conduction, the electrode response at low frequency was not observed. Therefore, the oxygen ionic conduction is not likely the case and we instead propose the electronic conduction to be the dominating mechanism for both undoped (i.e. BNBT) and doped (i.e. Li and Fe) BNBT samples, which is consistent with the studies of BNT-BT-CZ [60] and BNT-BT-KNN [50] and BNT-BT-NN [61]. In this study, the addition of Li or Fe most likely causes a reduction of energy barrier required for electronic conduction [50]. Consequently, the resistivity decreased with increasing doping level.

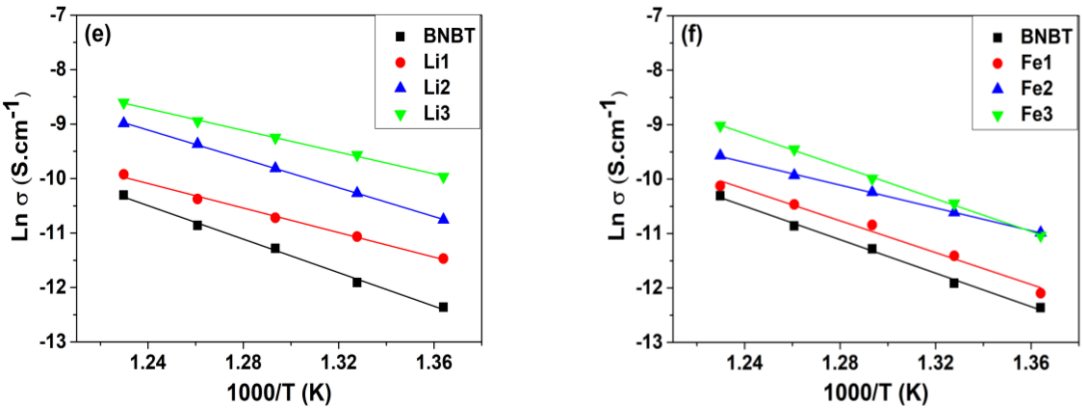


**Fig.** 9. The Arrhenius plots of (a) BNBT–$x$Li and (b) BNBT–$x$Fe ceramics. The symbols represent the experimental data and the straight line is the least-square fit.

**Table III** The resistivity at 540°C and activation energy of conduction of BNBT–*x*Li and BNBT–*x*Fe ceramics

| Compositions | $\rho_{540°C}$ (Ω.cm) | $E_a$ (eV) |
|---|---|---|
| BNBT | $3.21 \times 10^6$ | 1.33 |
| Li1 | $2.18 \times 10^6$ | 0.97 |
| Li2 | $0.98 \times 10^6$ | 1.14 |
| Li3 | $0.72 \times 10^6$ | 0.86 |
| Fe1 | $2.56 \times 10^6$ | 1.26 |
| Fe2 | $1.56 \times 10^6$ | 0.90 |
| Fe3 | $1.02 \times 10^6$ | 1.29 |

Fig. 10(a)–(f) and Fig. 11(a)–(f) exhibits room temperature polarization hysteresis (*P*-*E*) loops and bipolar strain curves (*S*-*E*) of BNBT-*x*Li and BNBT-*x*Fe ceramics (*x*=0, 0.01, 0.02 and 0.03) under an applied electric field of 50 kV/cm at 1 Hz. Related ferroelectric and piezoelectric parameters including $E_c$, $P_r$, $P_s$, $P_r/P_s$ ratio, negative strain ($S_{neg}$) and positive strain ($S_{pos}$) are listed in Table IV. For pure BNBT, a relaxor-like slim *P*-*E* loop with relatively small $P_r$ (11.5 μC/cm$^2$) and $E_c$ (11.3 kV/cm) together with a sprout shaped *S*-*E* curve with no noticeable $S_{neg}$ (Fig. x(a)) were observed, indicating that the obtained BNBT is in ergodic relaxor state having a "weak" polar phase at zero electric field which can reversibly transform into ferroelectric state under an applied field [62] [63] [64]. However, it's observed that the $P_r$ and $E_c$ of BNBT in this study were lower than the reported values in previous studies of the same composition [65] [20], which may be attributed to the differences in the purity of the starting materials and/or the preparing conditions especially those that affect Bi and Na volatility [17] [20]. Interestingly, it was found that A-site (Li) and B-site (Fe) doped BNBT ceramics clearly exhibited different ferroelectric and piezoelectric properties upon increasing doping level (*x*).

For Li doping, at $x = 0.01$ (Li1), both slim *P*-*E* loop and sprout-shaped *S*-*E* curve with similar $E_c$, $P_r$, $P_s$ and $S_{neg}$ values to that of BNBT were observed, suggesting that Li1

is still an ER. With increasing $x$ to 0.02 (Li2), an abrupt change to a square-like $P$-$E$ loop with a substantial increase in $E_c$ (from 10.4 to 30.7 kV/cm) and $P_r$ (from 11.8 to 33.9 μC/cm$^2$), which is a common characteristic for ferroelectric, was observed and sustained up to $x$ = 0.03 (Li3). Corresponding well to the $P$-$E$ loops, the $S$-$E$ curves exhibited a sudden change from a sprout to a butterfly shape with obvious $S_{neg}$ at $x$ = 0.02 (Li2), which persisted up to $x$ = 0.03 (Li3). These drastic changes from a slim- to a rectangular-shaped $P$-$E$ loop along with a transition from a sprout- to a butterfly-shaped $S$-$E$ curves indicate that 2 mol% Li doping can induced the BNBT from ergodic relaxor (ER) to ferroelectric (or more precisely a nonergodic relaxor (NER) state). The results agreed well with the $T_{F\text{-}R}$ values, which were around RT for BNBT (26°C) and Li1 (37°C) but were significantly higher than RT for Li2 (67°C) and Li3 (97°C).

On the contrary, a slight constricted $P$-$E$ loops with the $E_c$ that slightly varied in the range of 13.5–15.1 kV/cm was observed in all Fe-doped BNBT samples as seen from Fig. 10(e)-(f). Furthermore, both $P$-$E$ and $S$-$E$ data demonstrated that 1 mol% Fe (Fe1) can induce the ferroelectric order as evidently seen from a substantial increase in $P_r$ (from 11.5 to 28.6 μC/cm$^2$), a moderate increase in $P_s$ (from 34.5 to 38.5 μC/cm$^2$) and the emergence of butterfly-shaped bipolar strain with obvious $S_{neg}$ (0.16%). With increasing of $x$ to 0.02 (Fe2) and 0.03 (Fe3), a gradual increase in $P_r$ (to 29.4 and 31.7 μC/cm$^2$), $P_s$ (to 39 and 39.7 μC/cm$^2$) and $S_{neg}$ (to 0.17% and 0.19%) were clearly detected, thus suggesting a continuous increase in ferroelectricity upon increasing Fe doping content. These observations were further supported by the $P_r/P_s$ ratio which showed a large jump from 33.3% (BNBT) to 74.3 (Fe1) and then kept increasing to 75.4% (Fe2) and 79.8% (Fe3), indicating that a fraction of electric field-induced polarization, which remains after removing electric field, is larger in the sample with higher Fe content. In addition, alongside with the slight constricted P-E loop, it's worth noting that all Fe1, Fe2 and Fe3

samples possessed the deformed butterfly-shaped *S-E* curves, which can be observed as a broad feature around the negative strain minimum. Similar phenomena (i.e. slight constricted *P-E* loops and deformed butterfly-shape *S-E* curves) have also been encountered in other modified BNT-based materials when the measuring temperatures is close to the ferroelectric-to-relaxor transition temperature ($T_{F\text{-}R}$). In other words, it is often observed at the temperature slightly below $T_{F\text{-}R}$ or when the disrupted ferroelectric order is almost completely changed to the ergodic relaxor state (ER). Examples of those systems include $85BN_{0.5(1\text{-}x)}Li_{0.5x}$T-11BKT-4BT ($x$ = 0–0.15) [66] in which a gradual disruption of ferroelectric order was observed with increasing $x$. In their study, a slim *P-E* loop together with sprout-shaped *S-E* curve were observed in the sample ($x$ = 0.15), which had $T_{F\text{-}R}$ lower than RT, while the exact same *P-E*/*S-E* behaviors to this study were detected at the measuring temperature of 40° in $x$ = 0.10 composition, which possessed the $T_{F\text{-}R}$ of 70°C. Similarly, for (1-$x$)BNKT-$x$$SrTi_{0.8}Zr_{0.2}O_3$ ($x$ = 0–1.0%) ceramics [67], the same phenomena as this study (i.e. a concurrent constricted *P-E* loop with high $P_r$ and the deformed butterfly *S-E* curve) were also observed at 10-20°C lower than the $T_{F\text{-}R}$ e.g. at 60°C ($T_{F\text{-}R}$ = 71°C), for $x$ = 0 and at 90°C ($T_{F\text{-}R}$ = 109°C), for $x$ = 0.2%. Thus, based on these studies, we proposed the $T_{F\text{-}R}$, which located slightly above the RT in all Fe1 (36°C) Fe2 (45°C) and Fe3 (41°C) samples, to be responsible for the observed constricted *P-E* loops in Fe-doped BNBT ceramics.

For the compositions around the MPB where two phases coexist, the *P-E* loop characteristics (e.g. $E_c$, $P_r$) are also greatly influenced by the phase fraction or the dominating phase [68] [69] [30]. For example, the higher the *P4bm* phase is, the smaller the $E_c$ and $P_r$ is observed for BNBT-based ceramics having *R3c* and *P4bm* coexistent phases [30] [68] while the opposite trend (i.e. a higher $E_c$ and $P_r$) was detected for PZT-based systems [70]. In this study, the data from XRD and Rietveld refinement clearly

showed that both BNBT-*x*Li and BNBT-*x*Fe ceramics possessed similar amount of *R3c* (~79%–85%) and *P4bm* (~15–21%) phase upon increasing doping content, which was even further confirmed by XANEs analysis for the case of BNBT-*x*Fe ceramics to be consistent (80% *R3c* 20% *P4bm*). Besides, the microstructure (i.e. grain size), which can also affect the *P*-*E* loop features [68], was also revealed by the SEM to display the same trend upon increasing either Li or Fe doping level. Accordingly, the attributing of inconsistencies of high-field ferroelectric and piezoelectric properties between BNBT-*x*Li and BNBT-*x*Fe ceramics to the $T_{F\text{-}R}$ seems to be reasonable as other influencing factors (e.g. crystal structure and microstructure) were verified to be mostly the same change upon increasing either Li or Fe doping content.

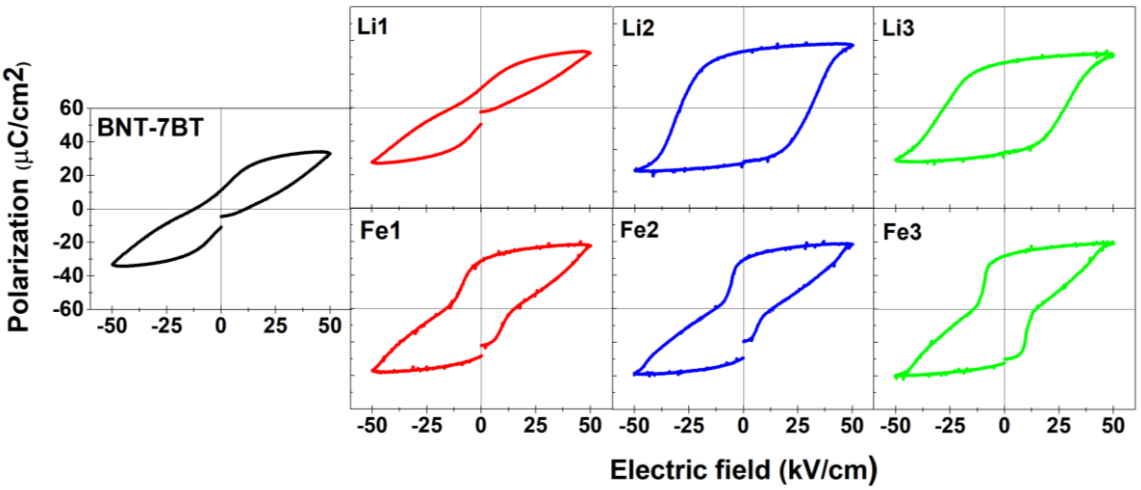


**Fig. 10.** Room temperature polarization hysteresis (*P*-*E*) loops of BNBT-*x*Li and BNBT-*x*Fe ceramics (x = 0, 0.01, 0.02 and 0.03) measured at 1 Hz.

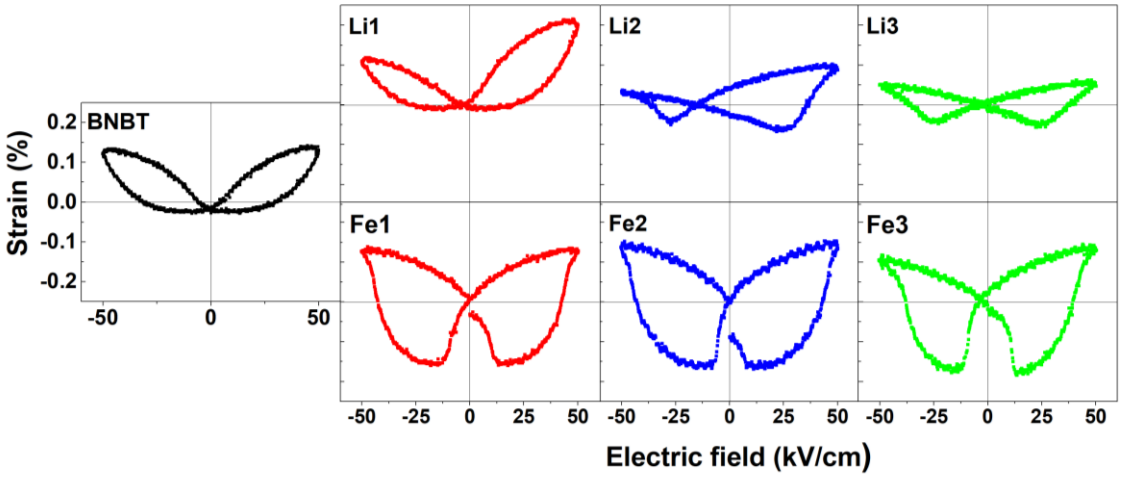


**Fig. 11.** Room temperature bipolar strain curves of BNBT-*x*Li and BNBT-*x*Fe ceramics ($x$ = 0, 0.01, 0.02 and 0.03) measured at 1 Hz.

**Table IV** Room temperature ferroelectric and strain properties of BNBT-*x*Li and BNBT-*x*Fe ceramics ($x$ = 0, 0.01, 0.02 and 0.03)

| Compositions | $E_c$ (kV/cm) | $P_r$ (μC/cm$^2$) | $P_s$ (μC/cm$^2$) | $P_r/P_s$ (%) | $S_{neg}$ (%) (+$E$ direction) | $S_{pos}$ (%) (+$E$ direction) |
|---|---|---|---|---|---|---|
| BNBT | 11.3 | 11.5 | 34.5 | 33.3 | - | 0.16 |
| Li1 | 10.4 | 11.8 | 33.4 | 35.3 | - | 0.22 |
| Li2 | 30.7 | 33.9 | 38.3 | 88.5 | 0.073 | 0.11 |
| Li3 | 27.7 | 26.7 | 32.2 | 82.9 | 0.065 | 0.066 |
| Fe1 | 15.1 | 28.6 | 38.5 | 74.3 | 0.16 | 0.14 |
| Fe2 | 13.5 | 29.4 | 39.0 | 75.4 | 0.17 | 0.16 |
| Fe3 | 14.5 | 31.7 | 39.7 | 79.8 | 0.19 | 0.15 |

## Conclusions

Dense BNBT-*x*Li and BNBT-*x*Fe ($x$ = 0.01-0.03) ceramics were obtained via conventional solid-state reaction mixed-oxide route. XRD refinement revealed a coexistence of rhombohedral (*R3c*) and tetragonal (*P4bm*) phases with almost unchanged *R3c*/*P4bm* phase ratio (~80/20) across the entire A-site Li and B-site Fe doping level studied. The results were further confirmed by XANEs analysis. With increasing Li or Fe doping content, the average grain size tended to increase while the resistivity ($\rho$) and

activation energy of conduction ($E_a$) exhibited a decreasing trend, indicating that the samples became more conductive. However, different ferroelectric and piezoelectric properties were observed between A-site Li and B-site Fe doping. For A-site Li doping, 2 mol% doping level can transform the materials from an ergodic relaxor (ER) to ferroelectric as seen from a square-type *P-E* loops with substantial increase in $E_c$ (30.7 kV/cm), $P_r$ (33.9 μC/cm$^2$) and the presence of $S_{neg}$ (0.11%) in *S-E* curves. Meanwhile, for B-site Fe doping, slight constricted *P-E* with a moderate increase in $E_c$ (~13–15 kV/cm) and $P_r$ (28–31 μC/cm$^2$) was observed throughout the whole doping level studied. The discrepancies could be linked to the ferroelectric-to-relaxor transition temperature ($T_{F-R}$) which exhibited a pronounced increase for Li doping but only showed moderate rise for Fe doping (97$^o$C, for Li3, and 41$^o$C. for Fe3). Thus, this study highlights the differences in the *P-E* loop and *S-E* curves of Li and Fe doping, which will be beneficial for tailoring the BNT-based materials' properties for different applications.

**Acknowledgement**

This work was financially supported by Thailand Research Fund and Synchrotron Light Research Institute.

## References


[1] B. Jaffe, Piezoelectric ceramics, Elsevier, 2012.

[2] A.J. Moulson, J.M. Herbert, Electroceramics: materials, properties, applications, John Wiley & Sons, 2003.

[3] T.R. Shrout, R. Eitel, S. Zhang, C. Randall, E. Alberta, P. Rehrig, Recent developments in transition temperature (T/sub c/) perovskite crystals, in: IEEE, 2003: pp. 774–777.

[4] S. Zhang, J.B. Lim, H.J. Lee, T.R. Shrout, Characterization of hard piezoelectric lead-free ceramics, IEEE Transactions on Ultrasonics, Ferroelectrics, and Frequency Control. 56 (2009).

[5] P. Lambeck, G. Jonker, The nature of domain stabilization in ferroelectric perovskites, Journal of Physics and Chemistry of Solids. 47 (1986) 453–461.

[6] L. Zhang, X. Ren, In situ observation of reversible domain switching in aged Mn-doped BaTiO 3 single crystals, Physical Review B. 71 (2005) 174108.

[7] R. Directive, Directive 2002/95/EC of the European Parliament and of the Council of 27 January 2003 on the restriction of the use of certain hazardous substances in electrical and electronic equipment, Official Journal of the European Union. 13 (2003) L37.

[8] T. Takenaka, K. Maruyama, K. Sakata, $(Bi_{1/2}Na_{1/2})TiO_3$-$BaTiO_3$ system for lead-free piezoelectric ceramics, Japanese Journal of Applied Physics. 30 (1991) 2236.

[9] C. Ma, X. Tan, Phase diagram of unpoled lead-free–ceramics, Solid State Communications. 150 (2010) 1497–1500.

[10] E. Aksel, E. Erdem, P. Jakes, J.L. Jones, R.-A. Eichel, Defect structure and materials "hardening" in $Fe_2O_3$-doped $[Bi_{0.5}Na_{0.5}]TiO_3$ ferroelectrics, Applied Physics Letters. 97 (2010) 012903.

[11] H. Zhang, J. Zhou, W. Chen, X. Yang, J. Shen, C. Wu, Stabilization of Ferroelectric Order in $Bi_{1/2}(Na_{0.8}K_{0.2})_{1/2}TiO_3$ Lead-Free Ceramics with Fe Doping, Journal of Electronic Materials. 46 (2017) 6167–6174.

[12] E. Sapper, R. Dittmer, D. Damjanovic, E. Erdem, D.J. Keeble, W. Jo, T. Granzow, J. Rödel, Aging in the relaxor and ferroelectric state of Fe-doped (1-x)$(Bi_{1/2}Na_{1/2})TiO_3$-x$BaTiO_3$ piezoelectric ceramics, Journal of Applied Physics. 116 (2014) 104102.

[13] W. Jo, E. Erdem, R.-A. Eichel, J. Glaum, T. Granzow, D. Damjanovic, J. Rödel, Effect of Nb-donor and Fe-acceptor dopants in $(Bi_{1/2}Na_{1/2})TiO_3$–$BaTiO_3$–$(K_{0.5}Na_{0.5})NbO_3$ lead-free piezoceramics, Journal of Applied Physics. 108 (2010) 014110.

[14] M. Zhu, L. Liu, Y. Hou, H. Wang, H. Yan, Microstructure and electrical properties of MnO-doped $(Na_{0.5}Bi_{0.5})_{0.92}Ba_{0.08}TiO_3$ lead-free piezoceramics, Journal of the American Ceramic Society. 90 (2007) 120–124.

[15] Y. Hiruma, H. Nagata, T. Takenaka, Thermal depoling process and piezoelectric properties of bismuth sodium titanate ceramics, Journal of Applied Physics. 105 (2009) 084112.

[16] M. Li, M.J. Pietrowski, R.A. De Souza, H. Zhang, I.M. Reaney, S.N. Cook, J.A. Kilner, D.C. Sinclair, A family of oxide ion conductors based on the ferroelectric perovskite $Na_{0.5}Bi_{0.5}TiO_3$, Nature Materials. 13 (2014) 31–35.

[17] X. Liu, Y. Zhao, J. Shi, H. Du, X. Xu, H. Lu, J. Che, X. Li, Improvement of dielectric and ferroelectric properties in bismuth sodium titanate based relaxors

through Bi non-stoichiometry, Journal of Alloys and Compounds. 799 (2019) 231–238.
[18] Y. Sung, J. Kim, J. Cho, T. Song, M. Kim, T. Park, Effects of Bi nonstoichiometry in $(Bi_{0.5+x}Na)TiO_3$ ceramics, Applied Physics Letters. 98 (2011) 012902.
[19] D.P. Shih, A. Aguadero, S.J. Skinner, Improvement of ionic conductivity in A-site lithium doped sodium bismuth titanate, Solid State Ionics. 317 (2018) 32–38.
[20] S. Prasertpalichat, D.P. Cann, Hardening in non-stoichiometric $(1-x)Bi_{0.5}Na_{0.5}TiO_3–xBaTiO_3$ lead-free piezoelectric ceramics, Journal of Materials Science. 51 (2016) 476–486.
[21] G. Yesner, A. Safari, Improved resistivity in bismuth deficient morphotropic phase boundary 0.88BNT-0.08 BKT-0.04BT ceramics, in: IEEE, 2017: pp. 110–112.
[22] B. Ravel, M. Newville, ATHENA, ARTEMIS, HEPHAESTUS: data analysis for X-ray absorption spectroscopy using IFEFFIT, Journal of Synchrotron Radiation. 12 (2005) 537–541.
[23] H. Simons, J. Daniels, W. Jo, R. Dittmer, A. Studer, M. Avdeev, J. Rödel, M. Hoffman, Electric-field-induced strain mechanisms in lead-free $94\%(Bi_{1/2}Na_{1/2})TiO_3–6\%BaTiO_3$, Applied Physics Letters. 98 (2011) 082901.
[24] J.E. Daniels, W. Jo, J. Rödel, J.L. Jones, Electric-field-induced phase transformation at a lead-free morphotropic phase boundary: Case study in a $93\%(Bi_{0.5}Na_{0.5})TiO_3–7\%\ BaTiO_3$ piezoelectric ceramic, Applied Physics Letters. 95 (2009) 032904.
[25] S.-T. Zhang, A.B. Kounga, E. Aulbach, H. Ehrenberg, J. Rödel, Giant strain in lead-free piezoceramics $Bi_{0.5}Na_{0.5}TiO_3–BaTiO_3–K_{0.5}Na_{0.5}NbO_3$ system, Applied Physics Letters. 91 (2007) 112906.
[26] H. Hayashi, H. Inaba, M. Matsuyama, N. Lan, M. Dokiya, H. Tagawa, Structural consideration on the ionic conductivity of perovskite-type oxides, Solid State Ionics. 122 (1999) 1–15.
[27] R.D. Shannon, Revised effective ionic radii and systematic studies of interatomic distances in halides and chalcogenides, Acta Crystallographica Section A: Crystal Physics, Diffraction, Theoretical and General Crystallography. 32 (1976) 751–767.
[28] C. Wang, T. Xia, X. Lou, Effects of Fe2O3 doping on the electrical properties of $Na_{0.47}Bi_{0.47}Ba_{0.06}TiO_3$ lead-free ceramics, Ceramics International. 44 (2018) 22053–22058.
[29] G. Viola, R. McKinnon, V. Koval, A. Adomkevicius, S. Dunn, H. Yan, Lithium-induced phase transitions in lead-free $Bi_{0.5}Na_{0.5}TiO_3$ based ceramics, The Journal of Physical Chemistry C. 118 (2014) 8564–8570.
[30] Q. Xu, H. Liu, L. Zhang, J. Xie, H. Hao, M. Cao, Z. Yao, M.T. Lanagan, Structure and electrical properties of lead-free $Bi_{0.5}Na_{0.5}TiO_3$-based ceramics for energy-storage applications, RSC Advances. 6 (2016) 59280–59291.
[31] S. Prasertpalichat, T. Siritanon, N. Nuntawong, D.P. Cann, Structural characterization of A-site nonstoichiometric $(1-x)Bi_{0.5}Na_{0.5}TiO_3–xBaTiO_3$ ceramics, Journal of Materials Science. 54 (2019) 1162–1170.
[32] S. Limpijumnong, S. Rujirawat, A. Boonchun, M. Smith, B. Cherdhirunkorn, Identification of Mn site in $Pb(Zr,Ti)O_3$ by synchrotron x-ray absorption near-edge structure: Theory and experiment, Applied Physics Letters. 90 (2007) 103113.
[33] J. Jutimoosik, S. Hunpratub, S. Maensiri, S. Rujirawat, R. Yimnirun, On preferred Mn site in multiferroic $BiFeO_3$: A view by synchrotron x-ray absorption near edge structure spectroscopy, Journal of Applied Physics. 116 (2014) 104105.

[34] A. Ankudinov, B. Ravel, J. Rehr, S. Conradson, Real-space multiple-scattering calculation and interpretation of x-ray-absorption near-edge structure, Physical Review B. 58 (1998) 7565.
[35] E. Taghaddos, M. Hejazi, A. Safari, Electromechanical properties of acceptor-doped lead-free piezoelectric ceramics, Journal of the American Ceramic Society. 97 (2014) 1756–1762.
[36] T.H. Dinh, M.R. Bafandeh, J.-K. Kang, C.-H. Hong, W. Jo, J.-S. Lee, Comparison of structural, ferroelectric, and strain properties between A-site donor and acceptor doped $Bi_{1/2}(Na_{0.82}K_{0.18})_{1/2}TiO_3$ ceramics, Ceramics International. 41 (2015) S458–S463.
[37] S. Wongsaenmai, R. Yimnirun, P. Laoratanakul, Effects of Dopants on Phase Formation and Microstructure of Bismuth Sodium Titanate-Potassium Sodium Niobate Ceramics, Ferroelectrics. 458 (2014) 214–220.
[38] P. Peng, H. Nie, Z. Liu, W. Ren, F. Cao, G. Wang, X. Dong, Enhanced ferroelectric properties and thermal stability of Mn-doped $0.96(Bi_{0.5}Na_{0.5})TiO_3$-$0.04BiAlO_3$ ceramics, Journal of the American Ceramic Society. 100 (2017) 1030–1036.
[39] W. Jo, R. Dittmer, M. Acosta, J. Zang, C. Groh, E. Sapper, K. Wang, J. Rödel, Giant electric-field-induced strains in lead-free ceramics for actuator applications–status and perspective, Journal of Electroceramics. 29 (2012) 71–93.
[40] W. Jo, S. Schaab, E. Sapper, L.A. Schmitt, H.-J. Kleebe, A.J. Bell, J. Rödel, On the phase identity and its thermal evolution of lead free $(Bi_{1/2}Na_{1/2})TiO_3$-6 mol%$BaTiO_3$, Journal of Applied Physics. 110 (2011) 074106.
[41] E. Sapper, S. Schaab, W. Jo, T. Granzow, J. Rödel, Influence of electric fields on the depolarization temperature of Mn-doped (1-x) $Bi_{1/2}Na_{1/2}TiO_3$-x$BaTiO_3$, Journal of Applied Physics. 111 (2012) 014105.
[42] J. Rödel, W. Jo, K.T. Seifert, E. Anton, T. Granzow, D. Damjanovic, Perspective on the Development of Lead-free Piezoceramics, Journal of the American Ceramic Society. 92 (2009) 1153–1177.
[43] G. Dong, H. Fan, J. Shi, M. Li, Composition-and Temperature-Dependent Large Strain in $(1- x)(0.8Bi_{0.5}Na_{0.5}TiO_3–0.2Bi_{0.5}K_{0.5}TiO_3)–xNaNbO_3$ Ceramics, Journal of the American Ceramic Society. 98 (2015) 1150–1155.
[44] Y. Hiruma, K. Yoshii, H. Nagata, T. Takenaka, Phase transition temperature and electrical properties of $(Bi_{1/2}Na_{1/2})TiO_3$–$(Bi_{1/2}A_{1/2})TiO_3$ (A= Li and K) lead-free ferroelectric ceramics, Journal of Applied Physics. 103 (2008) 084121.
[45] J. Li, F. Wang, C.M. Leung, S.W. Or, Y. Tang, X. Chen, T. Wang, X. Qin, W. Shi, Large strain response in acceptor-and donor-doped $Bi_{0.5}Na_{0.5}TiO_3$-based lead-free ceramics, Journal of Materials Science. 46 (2011) 5702–5708.
[46] Y. Qin, S. Zhang, Y. Wu, C. Lu, J. Zhang, Impacts of acceptor doping on the piezoelectric properties and domain structure in NBT-based lead-free ceramics, Journal of the European Ceramic Society. 37 (2017) 3493–3500.
[47] C. Lee, H. Han, T.A. Duong, T.H. Dinh, C.W. Ahn, J. Lee, Stabilization of the relaxor phase by adding CuO in lead-free $(Bi_{1/2}Na_{1/2})TiO_3$–$SrTiO_3$–$BiFeO_3$ ceramics, Ceramics International. 43 (2017) 11071–11077.
[48] B.K. Barick, R.N.P. Choudhary, D.K. Pradhan, Dielectric and impedance spectroscopy of zirconium modified $(Na_{0.5}Bi_{0.5})TiO_3$ ceramics, Ceramics International. 39 (2013) 5695–5704.
[49] Q. Xu, M.T. Lanagan, X. Huang, J. Xie, L. Zhang, H. Hao, H. Liu, Dielectric behavior and impedance spectroscopy in lead-free BNT–BT–NBN perovskite ceramics for energy storage, Ceramics International. 42 (2016) 9728–9736.

[50] J. Zang, M. Li, D.C. Sinclair, W. Jo, J. Rödel, Impedance spectroscopy of (Bi1/2Na1/2) TiO3–BaTiO3 ceramics modified with $(K_{0.5}Na_{0.5})NbO_3$, Journal of the American Ceramic Society. 97 (2014) 1523–1529.
[51] Y. Huang, D. Shi, L. Liu, G. Li, S. Zheng, L. Fang, High-temperature impedance spectroscopy of $BaFe_{0.5}Nb_{0.5}O_3$ ceramics doped with $Bi_{0.5}Na_{0.5}TiO_3$, Applied Physics A. 114 (2014) 891–896.
[52] D. Sinclair, A. West, Effect of atmosphere on the PTCR properties of $BaTiO_3$ ceramics, Journal of Materials Science. 29 (1994) 6061–6068.
[53] T. Baiatu, R. Waser, K. Härdtl, dc electrical degradation of Perovskite-type Titanates: III, a model of the mechanism, Journal of the American Ceramic Society. 73 (1990) 1663–1673.
[54] R. Waser, T. Baiatu, K. Härdtl, dc Electrical Degradation of Perovskite-Type Titanates: I, Ceramics, Journal of the American Ceramic Society. 73 (1990) 1645–1653.
[55] R. Waser, T. Baiatu, K. Härdtl, dc Electrical Degradation of Perovskite-Type Titanates: II, Single Crystals, Journal of the American Ceramic Society. 73 (1990) 1654–1662.
[56] M. Bousquet, J.-R. Duclère, E. Orhan, A. Boulle, C. Bachelet, C. Champeaux, Optical properties of an epitaxial $Na_{0.5}Bi_{0.5}TiO_3$ thin film grown by laser ablation: Experimental approach and density functional theory calculations, Journal of Applied Physics. 107 (2010) 104107.
[57] M. Cernea, A.C. Galca, M.C. Cioangher, C. Dragoi, G. Ioncea, Piezoelectric BNT-BT 0.11 thin films processed by sol–gel technique, Journal of Materials Science. 46 (2011) 5621–5627.
[58] Y.-M. Li, W. Chen, J. Zhou, Q. Xu, X.-Y. Gu, R.-H. Liao, Impedance spectroscopy and dielectric properties of $Na_{0.5}Bi_{0.5}TiO_3$–$NaNbO_3$ ceramics, Physica B: Condensed Matter. 365 (2005) 76–81.
[59] J. East, D. Sinclair, Characterization of $(Bi_{1/2}Na_{1/2})TiO_3$ using electric modulus spectroscopy, Journal of Materials Science Letters. 16 (1997) 422–425.
[60] J. Zang, M. Li, D.C. Sinclair, T. Frömling, W. Jo, J. Rödel, Impedance Spectroscopy of $(Bi_{1/2}Na_{1/2})TiO_3$–$BaTiO_3$ Based High-Temperature Dielectrics, Journal of the American Ceramic Society. 97 (2014) 2825–2831.
[61] Q. Xu, M.T. Lanagan, W. Luo, L. Zhang, J. Xie, H. Hao, M. Cao, Z. Yao, H. Liu, Electrical properties and relaxation behavior of $Bi_{0.5}Na_{0.5}TiO_3$-$BaTiO_3$ ceramics modified with $NaNbO_3$, Journal of the European Ceramic Society. 36 (2016) 2469–2477.
[62] A. Ullah, C. Won Ahn, A. Ullah, I. Won Kim, Large strain under a low electric field in lead-free bismuth-based piezoelectrics, Applied Physics Letters. 103 (2013) 022906.
[63] K. Wang, A. Hussain, W. Jo, J. Rödel, Temperature-Dependent Properties of $(Bi_{1/2}Na_{1/2})TiO_3$–$(Bi_{1/2}K_{1/2})TiO_3$–$SrTiO_3$ Lead-Free Piezoceramics, Journal of the American Ceramic Society. 95 (2012) 2241–2247.
[64] W. Jo, T. Granzow, E. Aulbach, J. Rödel, D. Damjanovic, Origin of the large strain response in $(K_{0.5}Na_{0.5})NbO_3$-modified $(Bi_{0.5}Na_{0.5})TiO_3$–$BaTiO_3$ lead-free piezoceramics, Journal of Applied Physics. 105 (2009) 094102.
[65] H. Lidjici, B. Lagoun, M. Berrahal, M. Rguitti, M.A. Hentatti, H. Khemakhem, XRD, Raman and electrical studies on the $(1- x)(Na_{0.5}Bi_{0.5})TiO_3- xBaTiO_3$ lead free ceramics, Journal of Alloys and Compounds. 618 (2015) 643–648.

[66] D. Yin, Z. Zhao, Y. Dai, Z. Zhao, X. Zhang, S. Wang, Electrical properties and relaxor phase evolution of Li-modified BNT-BKT-BT lead-free ceramics, Journal of the American Ceramic Society. 99 (2016) 2354–2360.
[67] Y. Guo, H. Fan, J. Shi, Origin of the large strain response in tenary $SrTi_{0.8}Zr_{0.2}O_3$ modified $Bi_{0.5}Na_{0.5}TiO_3$–$Bi_{0.5}K_{0.5}TiO_3$ lead-free piezoceramics, Journal of Materials Science. 50 (2015) 403–411.
[68] L. Jin, F. Li, S. Zhang, Decoding the fingerprint of ferroelectric loops: comprehension of the material properties and structures, Journal of the American Ceramic Society. 97 (2014) 1–27.
[69] K. Yoshii, Y. Hiruma, H. Nagata, T. Takenaka, Electrical properties and depolarization temperature of $(Bi_{1/2}Na_{1/2})TiO_3$–$(Bi_{1/2}K_{1/2})TiO_3$ lead-free piezoelectric ceramics, Japanese Journal of Applied Physics. 45 (2006) 4493.
[70] L. Jin, Broadband dielectric response in hard and soft PZT: Understanding softening and hardening mechanisms, Ceramics Laboratory. (2011).